



**HAL**  
open science

# La formation et le transport des particules dans le plasma froid

Jiashu Lin

► **To cite this version:**

Jiashu Lin. La formation et le transport des particules dans le plasma froid. Autre. Université d'Orléans; Kyoto Institute of Technology, 2020. Français. NNT : 2020ORLE3029 . tel-03124143

**HAL Id: tel-03124143**

**<https://theses.hal.science/tel-03124143>**

Submitted on 28 Jan 2021

**HAL** is a multi-disciplinary open access archive for the deposit and dissemination of scientific research documents, whether they are published or not. The documents may come from teaching and research institutions in France or abroad, or from public or private research centers.

L'archive ouverte pluridisciplinaire **HAL**, est destinée au dépôt et à la diffusion de documents scientifiques de niveau recherche, publiés ou non, émanant des établissements d'enseignement et de recherche français ou étrangers, des laboratoires publics ou privés.

ÉCOLE DOCTORALE ENERGIE, MATERIAUX, SCIENCE DE LA TERRE ET DE L'UNIVERS

THÈSE EN COTUTELLE INTERNATIONALE présentée par :

**Jiashu LIN**

soutenue le : Janvier 2020

pour obtenir le grade de :

**Docteur de Université d'Orléans  
et de Kyoto institute of technology**

Discipline/ Spécialité : Physique des plasmas

**Formation and transport of particles in  
low temperature plasmas**

THÈSE dirigée par :

[Pr. BOUFENDI Laïfa]

[Pr. TAKAHASHI Kazuo]

Professeur, Université d'Orléans

Professeur, Kyoto institute of technology

JURY :

[Pr. ISSHIKI Toshiyuki]

[Pr. AWATSUJI Yasuhiro]

[Pr. MOTELICA Mikael]

[Pr. BOUFENDI Laïfa]

[Pr. TAKAHASHI Kazuo]

Professeur, Kyoto institute of technology

Professeur, Kyoto institute of technology

Professeur, Université d'Orléans

Professeur, Université d'Orléans

Professeur, Kyoto institute of technology

Président

Examineur

Examineur

Examineur

Examineur



Formation and transport of particles in low temperature  
plasmas

Jiashu Lin

Department of Electronics, Kyoto Institute of Technology, Japan

GREMI, Université d'Orléans, France

Email address: [jiashu.lin@etu.univ-orleans.fr](mailto:jiashu.lin@etu.univ-orleans.fr)

February 6, 2020



# Abstract

This thesis studies the dust particles in plasmas. It consists of two parts. The first part is the formation of dust particles. That is to study how the dust particles are generated from the reactive gas in the plasmas. The second part is the transport behaviour of dust particles. That is to study how the dust particles act in the plasmas.

In the part of the formation of dust particles, carbon dust particles are generated in the plasmas. It is known that the formation process of dust particles in plasmas can be determined by 3 steps: nucleation, agglomeration and surface grow. The nucleation step is focused. The results of experiments show that the nucleation process occurs faster in higher power, higher pressure and lower temperature. The dependency of the nucleation time on the temperature is explained by the vibration-transition energy relaxation mechanism, and that on the RF power and pressure is explained by the ratio of the charge and diffusion time of the small dust particles.

In the part of the transport behaviours of dust particles, industrially fabricated particles with determined size are injected into Ar plasmas. The particles in the plasmas are observed by laser scattering with a CCD camera. The diagnostics of plasma are performed by a double Langmuir probe. Pulse-time modulation to the Ar RF plasmas is studied to be a factor to influence and to control the transport of dust particles. Particles of mono-dispersed size are firstly studied in the plasmas. It is shown that the levitating positions and falling down processes can be controlled by RF power and pulse-time modulation. Secondly, two sizes particles are injected into the plasma at same time. The different transport behaviours, as like the segmentation of levitation and different timing of falling down basis on their size, are observed. Particles of mixture sizes can be separated one size particles from other sizes. The mechanisms of transport behaviours of the dust particles are investigated by the combination of the diagnostic of plasma parameters (electron temperature and ion density in principle) by the double Langmuir probe and calculation of the forces acting on the dust particles. Calculation methods adjusting to the specific experiment setup are established. The calculation results have a good agreement with that of the experiments.



# Résumé

Les plasma poudreux sont des plasmas qui contiennent des particules solides dont les tailles vont quelques nanomètres à quelques dizaines de micromètres. La présence de ces particules solides, dans les plasmas, a été découverte dans les procédés de l'industrie de microélectronique. Les particules dans le plasma étaient considérées comme la source principale de la contamination de ces procédés. Les premiers travaux de recherche étaient focalisés sur les méthodes et moyens de les éliminer et d'empêcher leur formation. Suite à l'identification des différentes phases de formation et la découverte de la structure cristalline des nanoparticules qui se forment dans la première phase des applications très prometteuses ont commencé à se développer dans différents domaines tels que le photovoltaïque, la nanoélectronique etc., Ceci a donné une nouvelle impulsion aux activités de recherches sur les propriétés du plasma poudreux ont attiré l'attention de plus en plus de chercheurs à travers le monde.

Les travaux de recherche, entrant dans le cadre de cette thèse, sur les plasmas poudreux, ont été focalisés essentiellement sur le contrôle de la formation des particules solides et leur transport dans le plasma. Par conséquent, cette thèse est composée par deux parties, la première concerne la formation des particules en phase gazeuse dans le plasma et la deuxième traitera du comportement et du transport du nuage dense de particules dans le plasma. Ces travaux ont été effectués au sein du laboratoire GRMI (Université d'Orléans, France) et du Département d'électronique du Kyoto Institute of Technology (Japon), respectivement, dans le cadre d'une co-tutelle.

Les travaux sur la formation des particules a été réalisée dans un plasma RF généré dans un mélange gazeux composé d'Argon (Ar, 98%) et d'Acétylène ( $C_2H_2$ , 2%). Le processus de formation des particules s'effectue en trois étapes: la nucléation (phase chimique), l'agglomération, et la croissance par dépôt radicalaire sur la surface des particules. Nous sommes intéressés à l'étape de nucléation. L'influence de la puissance, la pression et la température des gaz sur le temps de nucléation est étudiée. L'évolution temporelle de la tension d'auto polarisation de la décharge est utilisée comme un indice pour détecter la fin de l'étape de nucléation. Les résultats montrent que le temps de nucléation augmente avec l'augmentation de la température mais diminue avec celle de la puissance et de la pression. Cela dit, plus la température est basse, la puissance et la pression sont élevées, plus la phase de nucléation est rapide. La dépendance de la nucléation de la température est expliquée par le mécanisme de la relaxation de l'excitation translationnelle-vibrationnelle des molécules du gaz précurseur. En effet l'énergie d'excitation vibrationnelle joue le rôle d'énergie d'activation pour les réactions chimiques ayant lieu lors de cette phase. Par contre, celles sur la puissance et la pression, elles sont expliquées par la concurrence entre le temps de charge des nanoparticules et le temps de leur diffusion, ce qui conduit à leur perte. La caractérisation du plasma, au cours de la formation des nanoparticules montre que la

---

densité électrique augmente avec l'augmentation de la puissance RF. Ceci se traduit aussi la réduction du temps de charge des nanoparticules. De l'autre côté, l'augmentation de la pression réduit le parcours libre moyen, et par conséquent, aide à confiner les particules. Un calcul théorique de ce temps, basé sur ces mécanismes, est effectué et nous obtenons un bon accord avec celui déduit des expériences.

Dans la deuxième partie de ce travail de recherche sur le comportement et le transport du nuage de particules, nous avons utilisé des particules de tailles certifiées acquises auprès d'une entreprise spécialisée. Les particules sont injectées dans le plasma et observées par la diffusion de la lumière d'un faisceau laser. Une étude de l'influence de la modulation temporelle de la puissance RF sur le comportement collectif des particules est effectuée. Les études expérimentales sur l'effet de la modulation ont été effectuées parallèlement au diagnostic du plasma. Ainsi nous avons mis en évidence que la température électronique peut être contrôlée par la modulation. Les particules, de distribution en taille mono-dispersées, sont au départ localisées dans le plasma en jouant sur la modulation et la tension RF. Le piégeage et le dé-piégeage, les positions de lévitation dans le corps plasma et le dépôt sur la surface de l'électrode du bas sont examinées différentes conditions expérimentales. L'effet d'une distribution poly-dispersée des tailles des particules est étudiée en injectant un mélange de particules de deux tailles différentes. Un phénomène de ségrégation des particules basée sur leur taille est observé, et le dé-piégeage des particules du plasma s'opère à différentes conditions. Cela signifie que sous certaines conditions, les particules d'une certaine taille sont dé-piégées et celles de l'autre restent dans le plasma. Les particules mélangées en tailles peuvent être séparées les unes des autres. La structure du plasma, est calculée à partir des paramètres plasma mesurés par un système de double sondes de Langmuir. Les charges et les forces auxquelles sont soumises les particules dans le plasma sont examinées quantitativement. Les résultats numériques correspondent aux ceux donnés par les expériences.

Les différents résultats obtenus dans le cadre de cette thèse sur la formation, le comportement et le transport de nuages denses de particules dans le plasma ouvrent de réelles perspectives industrielles pour la fabrication et le traitement des particules par un plasma. Le plasma peut être un milieu de génération des particules, une <<passoire>> pour les classer selon leurs tailles, ou utilisé pour les transporter et les déposer en un lieu bien précis.

# Acknowledgment

This thesis is based on the Co-Supervisor between Orlans University and Kyoto Institute of Technology (KIT). I will thank deeply my supervisors Prof. Kazuo Takahashi, Prof. Laïfa Boufendi, and Dr. Marie Hénault, who continuously guided me during whole of the work. I will express my gratitude to Mr. Thomas Lecas for the technical aides in Orléans University. I am grateful to Prof. Yasuaki Hayashi and Mr. Satoru Oshima for encouragements during my study in KIT. I express my gratitude to Prof. Yasuhiro Awatsuji, Prof. Akio Sanpei, Prof. Sadao Masamune, who gave me doctoral lessons and precious advises. I would like to thank Dr. Sagi Orazbayev (Al-Farabi Kazakh National University), Mr. Almasbek Utegenov (Al-Farabi Kazakh National University), He Huang (Donhua University) for the cooperations in the experiments and wide discussions on the Dusty Plasmas. I want to express my gratitude to my team members of the research of dusty plasma in the laboratory in KIT: Ms. Kuri Hashimoto, Mr. Rui Togashi, Mr. Eigo Ito, Mr. Hiroto Tanaka, who performed the experiments with me. I would like to thank all member of the laboratory in KIT and in Orléans University who gave me a lot of life and language (Japanese and French) support during my study. I want to thank Dr. Michele Olios Pasco (Kyoto University) who helped me check the manuscript and gave me support both on English and French.



# Contents

<b>1</b>	<b>Introduction</b>	<b>13</b>
1.1	General . . . . .	13
1.2	Researches of dusty plasmas . . . . .	13
1.2.1	Formation of dust particles in plasmas . . . . .	14
1.2.2	Behaviours of dust particles in plasmas . . . . .	15
1.3	Applications . . . . .	16
1.4	Objective and outline of this thesis . . . . .	17
1.4.1	Chapter 2 Theoretical aspects . . . . .	17
1.4.2	Chapter 3 Experiment setups . . . . .	17
1.4.3	Chapter 4 Formation of dust particles . . . . .	17
1.4.4	Chapter 5 Pulse-time modulation to low pressure cold RF plasmas . . . . .	17
1.4.5	Chapter 6 Analysis methods . . . . .	18
1.4.6	Chapter 7 Transport behaviours of dust particles . . . . .	18
1.4.7	Chapter 8 Perspective . . . . .	19
1.4.8	Chapter 9 Conclusion . . . . .	19
1.5	French summery . . . . .	19
<b>2</b>	<b>Theoretical aspect</b>	<b>25</b>
2.1	Plasma parameters . . . . .	25
2.1.1	Electrons and ions densities, ionisation degree: $n_e, n_i, \alpha$ . . . . .	25
2.1.2	Electron and ion temperature: $T_e, T_i$ . . . . .	26
2.1.3	Plasma potential $V_p$ . . . . .	26
2.1.4	Debye length . . . . .	27
2.1.5	Continuity equation . . . . .	28
2.2	Collision . . . . .	28
2.2.1	Cross section of collision . . . . .	28
2.2.2	Mean free path and collision frequency . . . . .	28
2.2.3	Main collisions in low pressure cold plasma . . . . .	29
2.3	Ambipolar diffusion . . . . .	30
2.4	Plasma sheath . . . . .	31
2.4.1	Bohm sheath criterion . . . . .	32

2.4.2	Child-Langmuir law . . . . .	32
2.5	Solid body in plasma . . . . .	33
2.5.1	Sheath model . . . . .	33
2.5.2	Orbit-motion-limited model . . . . .	34
2.6	Charge of dust particle in plasma . . . . .	35
2.6.1	Charge time . . . . .	36
2.7	Forces act on dust particle in plasma . . . . .	37
2.7.1	Gravitational force . . . . .	37
2.7.2	Electrostatic force . . . . .	37
2.7.3	Ion drag force . . . . .	37
2.8	Diagnostic of plasma parameters . . . . .	39
2.8.1	Single probe method . . . . .	39
2.8.2	Double probe method . . . . .	40
2.8.3	Electron density measurement by microwave resonance cavity . . . . .	43
2.9	French summery . . . . .	45
<b>3</b>	<b>Experiment setup</b>	<b>49</b>
3.1	Particle formation experiments . . . . .	49
3.1.1	Plasma chamber . . . . .	49
3.1.2	Generator system . . . . .	49
3.1.3	Gas injection system . . . . .	49
3.1.4	Pumping system . . . . .	51
3.1.5	Temperature regulating system . . . . .	51
3.1.6	Diagnostics tools . . . . .	52
3.2	Particle behaviours experiments . . . . .	52
3.2.1	PK-3 plus chamber . . . . .	52
3.2.2	Particle dispenser . . . . .	54
3.2.3	Gas and electric connection . . . . .	56
3.2.4	Function generator and amplifier . . . . .	56
3.2.5	Optic system . . . . .	56
3.2.6	Double probe method . . . . .	60
3.3	French summery . . . . .	61
<b>4</b>	<b>Nucleation time of nano-particles in low pressure C<sub>2</sub>H<sub>2</sub>/Ar RF plasmas</b>	<b>65</b>
4.1	Introduction . . . . .	65
4.2	Experimental . . . . .	66
4.3	Results and Discussion . . . . .	66
4.4	Conclusion . . . . .	75
4.5	French summery . . . . .	77

<b>5</b>	<b>Pulse-time modulation</b>	<b>81</b>
5.1	Introduction . . . . .	81
5.2	Numerical simulation . . . . .	83
5.3	Experiment . . . . .	84
5.4	Results and discussion . . . . .	84
5.5	Conclusion . . . . .	87
5.6	French summery . . . . .	87
<b>6</b>	<b>Analysis methods</b>	<b>91</b>
6.1	Introduction . . . . .	91
6.2	Numerical solution of fluid model . . . . .	91
6.3	Boundary condition at sheath edge and sheath structure . . . . .	94
6.4	Particle charge in the bulk of plasma and in the sheath . . . . .	98
6.4.1	Particle charge in the bulk of plasma . . . . .	98
6.4.2	Particle charge in the sheath . . . . .	100
6.5	Conclusion . . . . .	100
6.6	French summery . . . . .	101
<b>7</b>	<b>Particle behaviours in RF plasmas</b>	<b>105</b>
7.1	Diagnostic of RF discharge . . . . .	106
7.1.1	Light emission . . . . .	108
7.1.2	Influence of presence of dusty particles to double langmuir probe measurements . . . . .	108
7.1.3	Spatial distribution of ion density and electron temperature . . . . .	111
7.2	Levitating position and trajectory of dust particles transported to electrodes in dusty plasmas . . . . .	113
7.2.1	Introduction . . . . .	113
7.2.2	Experiment . . . . .	113
7.2.3	Results . . . . .	113
7.2.4	Discussion . . . . .	119
7.2.5	Conclusion . . . . .	129
7.3	Segmentation of particles in their size . . . . .	129
7.3.1	Experimental . . . . .	130
7.3.2	Results . . . . .	130
7.3.3	Discussion . . . . .	132
7.3.4	Conclusion . . . . .	133
7.4	Classification of particles in their size . . . . .	134
7.4.1	Experimental . . . . .	139
7.4.2	Results and Discussion . . . . .	139
7.4.3	Conclusion . . . . .	148
7.5	Conclusion . . . . .	150
7.6	French summery . . . . .	151

---

<b>8</b>	<b>Perspective</b>	<b>155</b>
8.1	Introduction to LIBS . . . . .	155
8.1.1	Ablation of material by laser heating . . . . .	155
8.1.2	Generation of plasma based on the released material element particles . . . . .	156
8.1.3	Light emission by LIP . . . . .	157
8.2	Experiment . . . . .	157
8.2.1	Particles . . . . .	157
8.2.2	Laser . . . . .	158
8.2.3	Reactor . . . . .	159
8.2.4	Spectrometer . . . . .	159
8.2.5	Schematic . . . . .	160
8.3	Result . . . . .	160
8.4	Conclusion . . . . .	162
8.5	French summery . . . . .	162
<b>9</b>	<b>Conclusion</b>	<b>167</b>

# Chapter 1

## Introduction

### 1.1 General

Dusty plasmas are plasmas which contain inside their body nanometres ( $10^{-9}$  m) to millimetres ( $10^{-3}$  m) sized dust particles. They are also called as "complex plasmas". Dusty plasmas widely and universally exist both in nature and in laboratory.[1, 6, 1, 15] The nature of the dust particles can be nanosized clusters, nucleates, particulates, and complex aggregates, agglomerates.[5] Indeed, since the universal existence of dust materials in the atmosphere of earth and space, there are rather dusty plasmas in nature, for examples, as the lightning, aurora, ring of Saturn, *etc.*[1, 15] Especially, the discovery of dusts in the interstellar matter motivated many researchers in space science and astronomy to study dusty plasmas.[6]

In the industry and laboratory, the research of dusty plasma started from the field of the fabrication of microelectronic devices.[6] With the rapid decrease of the dimension of the integrated circuitry elements, contamination of small dust particles becomes a serious problem. The particle contamination can cause irremediable defect to the microelectronic devices.[7, 8] Many attempts were carried out to prevent the particle contamination to the devices. The developing and improving of the clean room is one of important measure to avoid the particle contamination from air. For some processes, in spite of the high level of the clean room class, the particle contamination occurs still. Researchers started to realise that the contamination occurs even in the process reactors. The discovery of dust particles in plasmas while the fabrication processes ignited the researches of the dusty plasmas firstly in order to eliminate the particle contamination.[6, 9, 10, 11, 12, 13]

### 1.2 Researches of dusty plasmas

Dust particles in the processing plasmas can be considered to have two general sources. In the first case, microsized particles can be produced by the sputtering of the target or reactor walls, and then trapped by the plasmas. In the other case, dust particles can be generated in the plasma by reacting gasses. The two cases lead the necessity to study both the transport behaviours and formation mechanism of dust particles in the plasmas. To know the transport behaviours allows the manipulation of the

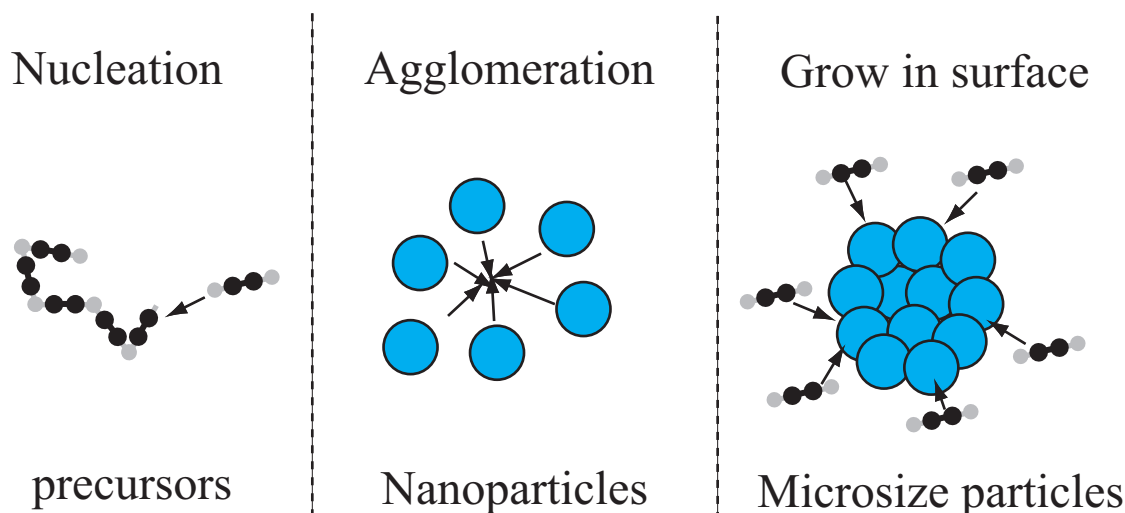


Figure 1.1: The 3-step process of the formation of dust particle in plasmas. Precursors nucleate to nanoparticles by chain reaction. Nanoparticles agglomerate to larger particles. Radicals deposit on the surface of the agglomerated particles.

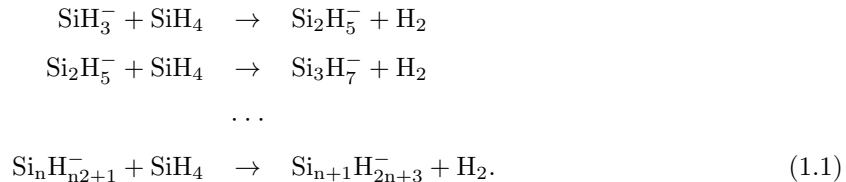
trajectory of the dust particles to avoid the contamination to the wafer substrate. The elucidation of the formation mechanism can prevent the generation of the dust particles.[6]

### 1.2.1 Formation of dust particles in plasmas

Studies of the formation of dust particles were initially performed in silene ( $\text{SiH}_4$ ) based plasma as the silene is one of the most frequently used gas in microelectronic manufacturing processes.[7] These earlier works made clear that the formation of dust particles in low-pressure plasmas is a 3-step process.[7, 10, 14, 15, 16, 17, 18] The first one corresponds to nucleation and growth of nanoparticles by chain reactions between ions and gas molecules, the second one is agglomeration of the nanoparticles to form larger particles, and finally, the particles grow by radical deposition on their surfaces. (Fig. 1.1)

Detection of the dust particles in situ of the processing plasmas were performed in earlier works by the laser light scattering.[10, 11]. In the studies, it is further found that during the formation process of dust particles, time evolution of electrical signals, as the discharge current and self bias voltage, and plasma parameters, as the electron density, show their features corresponding on the formation steps.[19, 20, 21] The dust particles in the plasma are negatively charged by free electrons. The appearance of the dust particles cause a decrease of electron density in the bulk of plasma. The decrease of electron density causes further a decrease of amplitude of self bias voltage in radio frequency (RF) plasmas.[20] Thus, the electron density and self bias voltage can be used for the detection of the dust particles. Furthermore, it is found an instability of the discharge current occurs at the end of the nucleation phase.[21] It allows to detect the phase transition timing and time duration of the nucleation process.[21]

Modeling of the formation of dust particle was dealt based on numerous experiments.[8, 15, 22, 23] The nucleation process in SiH<sub>4</sub>/Ar plasma can be expressed as



Identification of the nucleation phase allows detailed studies and applications.[15, 20, 21] Effect of gas temperature to the nucleation time in the SiH<sub>4</sub>/Ar plasma was studied in many experiments.[20, 15] The nucleation time increase with the increase of the gas temperature. This phenomenon is explained by further modeling work[15]: the nucleation process occurs by the chain reaction of reactive molecules thanks to the exceed vibrational energy. The vibrational energy is exceed by electron collisions and relaxed by collisions with atom or molecules. Knowledge of the nucleation process can be used both for the prevent and fabrication of nanoparticles.[20, 21]. One can avoid the conditions of the nucleation process to prevent the contamination, or interrupt the nucleation process at suitable moment by a modulation of discharge power to obtain specific sized particles.[20, 21]

In parallel of the studies of the SiH<sub>4</sub> based dusty plasmas, the formation of carbon based dust particles was also reported and studied in many experimental and numerical works.[24, 25] Hydrocarbon particles can be formed by acetylene (C<sub>2</sub>H<sub>2</sub>) or methane (CH<sub>4</sub>), and formation of fluorocarbon particles is observed in C<sub>4</sub>F<sub>8</sub> plasmas.[24, 25] Detailed mechanisms were given, and it is shown that they have the same tendency than the formation of the silicon based dust particles.

### 1.2.2 Behaviours of dust particles in plasmas

Meanwhile, behaviours of the dust particles in plasmas were widely studied, as like charging process[23, 10, 5], forces acting on the dust particles[7, 8, 9, 6, 32], single or collective motion[33, 34, 35, 36], effects of the presence of the dust particles on the plasma parameters, effect of the discharge conditions on the dusty plasma parameters[37] *etc.*

In the earlier works of the detection of dust particles by leaser scattering method, the dust particles were found at the boundaries of plasma sheath, and it is explained by the negative charge of the dust particles and the electric field in the plasmas.[10] An analytical method to calculate the charge of dust particle in the plasmas was established by taken into account an orbit-motion-limited (OML) model.[5] The forces acting on the dust particles have been also studied, and analytical formulas of these forces are founded.[6, 38] Detailed descriptions of these methods are presented in chapter 2.

Charges and forces on the dust particles are affected by the plasma parameters. The 1-dimensional fluid model is widely discussed and taken into the calculation in order to analyze the spatial distribution of the plasma parameters as well as the behaviours of the dust particles.[23, 7, 8, 9, 39] Experimental and analytical works in the 1-dimensional show that the dust particles levitate in different height position depending on the discharge conditions.[7, 8, 9] The 1-dimensional model is available for certain symmetrical discharge configuration, as like the parallel plat electrode under the consideration of the homogeneity in the direction parallel to the electrodes. That consideration is not always available

when the electrode is relative small comparers to the distance of inter electrode or to the dimension of the reactor chamber. The 2- or 3-dimensional discussions are required for certain cases. The multi-dimensional model should adapt each times to the specific geometry of the discharge configurations of the real experiment setups. The detailed discussion of the 2-dimensional fluid model adapted to the experiment setups used in this thesis are presented in the Chapter 6.

The discovery of coulomb crystal is another important factor to attract the interests of researchers.[40] Coulomb crystal is a crystalline structure formed by dust particles in the bulk of plasma when the inter-particle potential energy exceeds the kinetic energy.[6] The crystalline structure in macroscopic size, which can be observed by naked eyes, has grad interests for the studies of the phase transition and the crystalline structure itself.[41, 42, 43]

While the study of the coulomb crystal in the dusty plasmas, many unexpected phenomena were observed, as the void[44, 45], acoustic wave[33], vortex rotation[34, 35, 36], *etc.*

In certain conditions, a dust free region appears in the dusty plasmas while other parts are fully occupied by the dust particles. Usually, the void is obtained in the plasma centre.[44, 45] The appearance of the void is explained by the outward ion flux which repels the dust particles from the centre. That is caused by the inhomogeneity of the ionisation rate. Plasma parameters were measured through the void region to particle exiting region. According to the 1-dimensional fluid model analysis, a strongly ionisation area can be detected, and the void region corresponds the strongly ionisation area. Enhancement of ion density and electron temperature in the void was reported.[45] The existence and size of the void can be controlled by discharge conditions and the configuration of the discharge chamber.[12]

### 1.3 Applications

Some positive roles of the dust particle and their applications are also found in certain industries.[8, 24, 47, 48, 49, 50, 52, 51]

During the production of silicon thin films by plasma enhanced chemical vapor deposition (PECVD), it is found that when the discharge conditions are regulated close to that of the formation of nanoparticles, a new type of material, named polymorphous silicon, is obtained.[18, 8, 51] The polymorphous silicon shows an enhanced transport properties and stability as compere to amorphous silicon.[51, 52] The growth reaction of the polymorphous silicon and the cause of the evolution of its properties are further studied, and the particle formation processes in the plasmas are proved to be the key point.[52, 53] The formation of nano-particles in silane plasma is considered as a potential for obtaining the new silicon films.[52] These "new silicon films" and nanoparticles incorporating plasmas are widely used for applications in solar cells in industry.[8, 5] It is reported that performance of PIN (p-type semiconductor/insulator/n-type semiconductor) solar cells can be significantly improved through nanocrystalline (usually 1~2 nm) inclusions deposited with high rates in silane-based PECVD.[5] The possibility to improve transport properties, photo induced degradation, control the energy band gape, minimize the film thickness *etc.* make the polymorphous silicon films to be a new potential candidate for the production of hight efficiency solar cells.[8, 5]

## 1.4 Objective and outline of this thesis

This thesis has two part of studies: formation of the dust particles in reactive gas plasma and their transport behaviours in inert gas plasma. In the part of the dust particle formation, the work is focused on the effects of gas temperature, pressure and discharge power on nucleation time of nano-particles in low pressure  $C_2H_2/Ar$  RF plasmas. In the part of the transport behaviours, the final objective is the classification of dust particles in their sizes by dusty plasmas. A time-pulse modulation method is applied to a regulation factor of the discharge conditions. Control of the levitation positions and transport trajectory of dust particles is studied and the effect of their sizes is in question in order to separate and classify them. The studies of the formation of the dust particles and the classification of them in their sizes have the interests to the fabrication of the nano- or micro- particles by improving the mono-dispersity of the particle size. This thesis consist of 9 chapters.

### 1.4.1 Chapter 2 Theoretical aspects

Some basic theoretical notions concerning the main works of this thesis are introduced in this chapter.

### 1.4.2 Chapter 3 Experiment setups

Two experiment setups are presented in this chapter. One is that for the study of the formation process of carbon particles by  $C_2H_2/Ar$  plasma. That is a temperature controllable system. The method of particle detection by electrical signals is implanted. This experiment setup is used in the *GRMI* laboratory, France. The other is that for the study of the transport behaviours. A reactor chamber same then that in PK-3 plus system is used with some modifications. Ar gas only is used in this system, and laser scattering method of the particle detection is implanted. This experiment setup is used in *Kyoto Institute of technology*, Japan.

### 1.4.3 Chapter 4 Formation of dust particles

In this chapter, nucleation time for carbon dust particles is studied in low pressure Acetyene/Argon radio RF plasmas. Since self-bias voltage on a powered electrode is drastically affected by transition from the nucleation to the agglomeration phases, nucleation time is measured by observing the self-bias voltage time evolution. The nucleation time increases with the gas temperature, and decreases when the gas pressure and the RF power are increased. A kinetic model, involving balance between diffusion and charging times of the nanoparticles as well as the chain reactions, is used to explain the exponential dependence of the nucleation time on the gas temperature. The balance between the times was especially indispensable to get good agreement between the model and the experimental results.

### 1.4.4 Chapter 5 Pulse-time modulation to low pressure cold RF plasmas

The time-pulse modulation is a method to manipulate the discharge conditions. Some effects of the time-pulse modulation were reported in the studies of the plasma etching processes.[2, 3] In this thesis, the effects of time-pulse modulation is expected to be a factor to study and control the transport

behaviours of the dust particles. The investigation of the time-pulse modulation for the discharge configuration is dealt in this chapter. By applying the time-pulse modulation to the RF power, the electron temperature can be regulated. The optimal frequency of the time-pulse modulation is discussed.

### 1.4.5 Chapter 6 Analysis methods

Calculation methods used to analyze the results of the experiments of transport behaviours are presented in detail in this chapter. The numerical solution of the 2-dimensional fluid model is discussed by adapting the specific geometry of the experiment set up. The sheath structure is discussed by taking the boundary condition between the bulk of plasmas and sheath into the Child-Langmuir law. The elucidation of the sheath structure allows the calculation of the charge of the dust particles through the sheath.

### 1.4.6 Chapter 7 Transport behaviours of dust particles

Main experiments and results to investigate the transport behaviours of dust particles are presented in this chapter. It contains a part of diagnostics of plasmas and 3 experiments of the observation of the transport behaviours of the dust particles. Dust particles are observed by the laser light scattering method. Time-pulse modulation and RF voltage are the main playable factors. Diagnostics of plasmas were performed firstly in order to make clear the effect on the plasma parameters of the regulation of the discharge conditions.

In the first experiment, dust particles of mono-dispersed size were injected in the plasmas. Levitating positions and dropping trajectory were studied by the regulating both the RF voltage and duty cycle of the time-pulse modulation. The charge of the dust particles and forces acting on them were calculated based on the combination of 2-dimensional fluid model and child-langmuir law.

In the second experiment, dust particles with two sizes were observed in a dusty plasma and they were divided into segments by changing RF voltage. Meanwhile a calculation and an analysis of forces acting on the dust particles were dealt based on measurement of plasma parameters. Segmentation of the dust particles depending on the voltage was discussed in this part. It made clear that spatial distribution of ion density with steep gradient induced ion flux by diffusion strong enough to make horizontal segments of the dust particles separated in their size. This means separating the dust particles horizontally can be controlled by changing the condition for generating the plasmas.

In the third experiment, the dust particles with two sizes were injected in the plasmas. The plasmas were generated by applying a pulse-time modulated RF voltage. The pulse-time modulation made it possible to change electron temperature in the plasmas. The electron temperature dominates charges of the dust particles and electric fields around the sheath where the dust particles are levitated. Equilibrium position of the dust particles can be determined by forces on them derived from the charges and the electric fields. In this research, it was clearly shown to change the position of the dust particles and drop them from the plasmas by the pulsed-time modulation. Furthermore, the modulated RF plasma worked as sieves of the dust particles. It was possible to drop larger dust particles from the plasma with leaving smaller ones in the plasmas.

### 1.4.7 Chapter 8 Perspective

A brief presentation the Leaser Introduced Breakdown Spectroscopy (LIBS) is done in this chapter. This work is not finished, but as a perspective of the next work. In the main part of this thesis, the formation and transport control of dust particle in the dusty plasma are studied. The LIBS method is to determine the chemical composition of the dust particle by suspending them in the dusty plasmas. The know-how of the control of the levitating positions of dust particles is useful in the LIBS work.

### 1.4.8 Chapter 9 Conclusion

The conclusion of this thesis is described in this chapter.

## 1.5 French summery

Plasmas poudreux sont des plasmas qui contiennent des particules solides dont les tailles peuvent être de quelques nanomètres à quelques dizaines de micromètres. La présence de ces particules dans les plasmas a été découverte dans les procédés utilisés dans l'industrie de la microélectronique. Les particules dans le plasma ont été reconnues comme la source principale de la contamination des réacteurs et par conséquent les recherches étaient effectuées au début des années 1990 visaient à les éliminer. Suite à la découverte d'applications intéressantes et les effets induits par le comportement collectif des nuages denses de particules piégées dans le plasma (structure cristalline), les recherches sur les propriétés du plasma poudreux même ont commencé à attirer l'attention de plus en plus de chercheurs.

Ainsi dans le cadre du programme de recherche sur les plasmas poudreux, les objectifs de cette thèse sont focalisés sur la compréhension des mécanismes de formation de ces particules solides et leur effets sur les propriétés du plasma, et d'en contrôler la formation et le mouvement dans le plasma et agissant sur les paramètres de celui-ci. Par conséquent, cette thèse est composée par deux parties principales, la recherche sur la formation des particules solides dans le plasma ainsi le comportement, et le transport dans le plasma. Ces travaux de recherche ont été effectués, dans le cadre d'une thèse en co-tutelle, au sein de laboratoire GRMI (Orléans, France) et de Kyoto Institute of technology (Japon), respectivement, dans le cadre de la collaboration entre ces deux institutions.



# Bibliography

- [1] C. K. Goertz, *Rev. Geophys.* **27** 271 (1989).
- [2] M. Hénault, Ph. D. thesis, University of Orleans, Orleans (2015).
- [3] M. Boudhib, Ph. D. thesis, University of Orleans, Orleans (2017).
- [4] P. K. Shukla, A. A. Mamun, *Introduction to Dusty Plasma Physics*, (IOP series of plasma Physics, 2002).
- [5] K. Ostrikov, *Rev. Mod. Phys.* **77**, 489, (2005).
- [6] K. Takahashi, Ph. D. thesis, Kyoto University, Kyoto (2000).
- [7] K. De Bleecker, Ph. D. thesis, Universiteit Antwerpen, Antwerpen (2006).
- [8] K. De Bleecker, A. Bogaerts, and Wim Goedheer, *Phys. Rev. E*, **70** 056407 (2004).
- [9] G. M. Jellum and D. B. Graves, *J. Appl. Phys.* **67**, 6490 (1990).
- [10] G. S. Selwyn, J. Singh, and R. S. Bennett, *J. Vac. Sci. Technol. A*, **7** 2758 (1989).
- [11] G. S. Selwyn, J. E. Heidenreich, and K. L. Haller, *Appl. Phys. Lett.* **57**, 1876 (1990).
- [12] S. J. Choi and M. J. Kushner, *J. Appl. Phys.* **74**, 853 (1993).
- [13] M. J. McCaughey and M. J. Kushner, *J. Appl. Phys.* **69**, 10 (1991).
- [14] A. Bouchoule, A. Plain, L. Boufendi, J. Ph. Blondeau and C. Laur, *J. Appl. Phys.* **70**,1991 (1991).
- [15] A. A. Fridman, L. Boufendi, T. Hbid, B. V. Potapkin, and A. Bouchoule, *J. Appl. Phys.* **79**, 1303 (1996).
- [16] L. Boufendi and A. Bouchoule, *Plasma Sources Sci. Technol.* **3**, 262 (1994).
- [17] L. Boufendi, A. Bouchoule and T. Hbid, *J. Vac. Sci. Technology* **A14**, 572 (1996).
- [18] L. Boufendi, M. Ch. Jouanny, E. Kovacevic, J. Berndt, and M. Mikikian, *J. Phys. D: Appl. Phys.* **44** 174035 (2011).
- [19] L. Boufendi, J. Gaudin, S. Huet, G. Viera, and M. Dudemaine, *Appl. Phys. Lett.* **79** 26 (2001).

- 
- [20] M. Cavarroc, M. Mikikian, and L. Boufendi, "*New insights on the earlier phase of nucleation and growth of nanoparticles in argon-silane*", 6th Intern. Conf. on Reactive Plasmas and 23rd Symp. on Plasma Processing, 2006, Matsushima-Sendai, Japan.
- [21] M. Cavarroc, M. Mikikian, G. Perrier, and L. Boufendi, *Appl. Phys. Lett.* **89** 013107 (2006).
- [22] K. De Bleecker, A. Bogaerts, and R. Gijbels. *Phys. Rev. E* **69** 056409 (2004).
- [23] K. De Bleecker, A. Bogaerts and W. Goedheer, *New J. Phys.* **8** 178 (2006).
- [24] K. De Bleecker, and A. Bogaerts, *Phys. Rev. E* **73** 026405 (2006).
- [25] K. Takahashi, and K. Tachibana, *J. Vac. Sci. Technol. A* **19** 2055 (2001).
- [26] A. V. Ivlev, M. Kretschmer, M. Zuzic, G. E. Morfill, H. Rothermel, H. M. Thomas, V. E. Fortov, V. I. Molotkov, A. P. Nefedov, A. M. Lipaev, O. F. Petrov, Yu. M. Baturin, A. I. Ivanov, and J. Goree, *Phys. Rev. Lett.* **90**, 05 (2003).
- [27] J. Goree, *Plasma Sources Sci. Technol.* **3**, 400, (1994).
- [28] A. Douglass, V. Land, K. Qiao, L. Matthews, and T. Hyde, *Phys. Plasmas* **19**, 013707 (2012).
- [29] V. Land, L. S. Matthews, and T. W. Hyde, *Phys. Rev. E* **81** 056402 (2010).
- [30] A. Douglass, V. Land, L. Matthews, and T. Hyde, *Phys. of Plasmas* **18**, 083706 (2011).
- [31] M. S. Barnes, J. H. Keller, J. C. Forster, J. A. O'Neill, and D. K. Coultas, *Phys. Rev. Lett.* **68**, 313 (1992).
- [32] L. Couëdel, M. Mikikian, L. Boufendi, and A.A Samarian, *Phys. Rev. E* **74** 026403 (2006).
- [33] L. Yang, M. Schwabe, S. Zhdanov, H. M. Thomas, A. M. Lipaev, V. I. Molotkov, V. E. Fortov, J. Zhang, and C. Du, *Europhysics Lett.* **117** 25001 (2017).
- [34] K. B. Chai, and P. M. Bellan, *Phys. Plasma*, **23**, 023701, (2016).
- [35] M. Schwabe, S. Zhdanov, C. R ath, D. B. Graves, H. M. Thomas, and G. E. Morfill, *Phys. Rev. Lett.* **112**, 115002 (2014).
- [36] M. Schwabe, and D. B. Graves, *Phys. Rev. E* **88**, 023101 (2013).
- [37] T. E. Sheridan, *J. Appl. Phys.* **106** 033303 (2009).
- [38] J. E. Daugherty, R. K. Porteous, and D. B. Graves, *J. Appl. Phys.* **73** 1617 (1993).
- [39] I. L. Semenov, *Phys. Rev. E*, **95** 043208 (2017).
- [40] Y. Hayashi, and K. Tachibana, *Jpn. J. Appl. Phys.* **33** L804 (1994).
- [41] H. Thomas, G. E. Morfill, J. Goree, B. Feuerbacher, and D. M ohlmann, *Phys. Rev. Lett.* **73** 652 (1994).

- [42] S. A. Maiorov, S. K. kodanova, M. K. Dosbolayev, T. S. Ramazanov, R. I. Golyatina, N. Kh. Bastykova, and A. U. Utegenov, *Phys. of Plamsas*, **22** 033705 (2015).
- [43] C. Dietz, and M. H. Thoma, *Phys. Rev. E* **94** 033207 (2016).
- [44] M. Mikikian, L. Couëdel, M. Cavarroc, Y. Tessier, and L. Boufendi, *New J. Phys.* **9**, 268 (2007).
- [45] V. Land, and W. J. Goedheer, *N. J. Phys.* **9** 246 (2007).
- [46] A. G. Khrapak, V. I. Molotkov, A. M. Lipaev, D. I. Zhukhovitskii, V. N. Naumkin, V. E. Fortov, O. F. Petrov, H. M. Thomas, S. A. Khrapak, P. Huber, A. Ivlev, and G. Morfill, *Contrib. Plasma Phys.* **56**, 253 (2016).
- [47] M. Lennox and S. Coulombe, *J. Nanopart. Res.* **14**, 1245 (2012).
- [48] R. L. Merlino, *Plasma Physics Applied* (Research Signpost, Kerala, India, 2006) p. 73.
- [49] D. A. Mendis and M. Rosenberg, *Annu. Rev. Astron. Astrophys.* **32**, 419 (1994).
- [50] K. Takahashi and K. Tachibana, *J. Appl. Phys.* **89**, 893 (2001).
- [51] M. Meaudre, R. Meaudre, R. Butté, and S. Vignoli, *J. Appl. Phys.* **86**, 946 (1999).
- [52] P. Roca i Cabarrocas, *J. Non-Cryst. Solids*, **266-269**, 31 (2000).
- [53] A. Fontcuberta i Morral, and P. Roca i Cabarrocas, *Thin Solid Films*, **383** 161 (2001).
- [54] H. Sugai, K. Nakamura, Y. Hikosaka, and M. Nakamura, *J. Vac. Sci. Technol.* **A13**, 887 (1995).
- [55] S. Samukawa, H. Ohtake and T. Mieno, *J. Vac. Sci. Technol.* **A14**, 3049 (1996).



# Chapter 2

## Theoretical aspect

### 2.1 Plasma parameters

Plasma is known as the fourth state of matter, which is evolved from the others state by getting more energy to break partially or fully the bonds between electrons and atoms/molecules. Plasmas contain basically free electrons, ions and neutral species such as radicals, atoms and molecules.[1, 15, 24, 25]

#### 2.1.1 Electrons and ions densities, ionisation degree: $n_e$ , $n_i$ , $\alpha$

The density of electrons and ions is depending on the density of ambient gas and ionisation degree  $\alpha$ , which is defined as

$$\alpha = \frac{n_i}{n_i + n_n}, \quad (2.1)$$

where  $n_i$  and  $n_n$  are the density of ions and neutral species respectively. According to the ionisation degree, plasmas can be categorised as

- Weakly ionised plasmas:  $\alpha \leq 10^{-6}$ .
- Intermediary ionised plasmas:  $10^{-6} \leq \alpha \leq 10^{-2}$ .
- Strongly ionised plasmas:  $\alpha \geq 10^{-2}$ .

The weakly ionised plasmas are concerned under focus in the work of this thesis.

Generally, plasmas are electrically neutral, which require that the average density of negative particle and positive particle should be equal in the bulk of the plasma.[1, 15, 24, 25]

$$n_e + \sum_k Z_k n_{k-} = \sum_j Z_j n_{j+}. \quad (2.2)$$

$Z$  is the charge number. Index  $k$  and  $j$  represent different sort of charged particles. The negatively charged particles can be the negative ions or charged dust particles. If there is not negative ions nor dust particles, and the positive ions are ionised only one time, the neutral condition can be simplified as  $n_e = n_i$ .

### 2.1.2 Electron and ion temperature: $T_e$ , $T_i$

Free electrons and ions in plasmas have kinetic energies. If their velocities can be considered to follow Maxwell-Boltzmann distribution, electron temperature  $T_e$  and ion temperature  $T_i$  can be defined. According the range and relation of  $T_e$  and  $T_i$ , plasmas can be categorised as

- Thermal plasmas:  $T_e \sim T_i$ .
- Non-thermal plasmas (cold plasmas):  $T_e \gg T_i$  with  $T_e \sim 10^4$  K (1 eV),  $T_i \sim 300$  -1000 K.

Non-thermal plasmas are mainly mentioned in this thesis. In cold plasmas, electrons and ions do not reach thermal equilibrium. Injected energy is mainly coupled to the electrons. The ions have almost same temperature as the neutrals about the ambient temperature.[1, 15, 24, 25]

Under the consideration of the Maxwell-Boltzmann distribution, average kinetic energy of electron and ion is given by

$$E_{\text{th}} = k_B T_{e,i}, \quad (2.3)$$

where  $k_B$  is the Boltzmann constant and  $T_{e,i}$  represent the electron or ion temperature. Average thermal velocity magnitude is given by

$$\bar{v} = \sqrt{\frac{8k_B T_{e,i}}{\pi m_{e,i}}}, \quad (2.4)$$

where  $m_{e,i}$  represent the electron or ion mass.

Electrons and ions are under the influence of electric potential in the plasmas. Faced on a potential barrier  $\Delta V$ , only the particles, which have the kinetic energy higher than the potential barrier,  $E_{\text{th}} > e\Delta V$ , where  $e$  is the elementary charge, can over come. Under the regime of the Maxwell-Boltzmann distribution, a relation between the potential barrier and the local density of electron or ion is given by

$$n'_e = n_{e,i} e^{-\frac{e\Delta V}{k_B T_e}}. \quad (2.5)$$

This is called Boltzmann relation.[1, 15, 24, 25]

In this thesis, ion and ambience temperature are given by Kelvin (K). Electron temperature is represented by Electron volte (eV) when it is appeared in experiment conditions or measurement results. In calculations, all temperatures are convert to Kelvin before substitute to the formula.

### 2.1.3 Plasma potential $V_p$

The average potential in the space of the plasma bulk between charged particles called plasma potential, usually noted as  $V_p$ . Electrons and ions generated in the bulk of plasma have tendency to diffuse toward outside. In cold plasmas, electron speed is much higher than the ion one, thus electrons have a tendency to diffuse more rapid than the ions. To compensate this inequality of the thermal speed, the plasma potential becomes positive.[1, 15, 24, 25]

### 2.1.4 Debye length

Debye length  $\lambda_{DL}$  is a typical value of the distance that a potential perturbation can give influence.[1, 15, 24, 25] When a negative potential  $\delta V$ , relative to that of the intrinsic plasma, appear in the plasma bulk, electrons around the perturbation point are repelled. This perturbation forme in local an area where the electro-neutrality is broken. This area is so called plasma sheath, and it plays the role to shield the potential perturbation. The debye length is the critical value for the shielding effect: within the debye length ( $r < \lambda_{DL}$ ), the local area is under the influence of the potential perturbation, out of the debye length ( $r > \lambda_{DL}$ ), the perturbation is shield. The Debye length  $\lambda_{DL}$  can be found by taken into account the Poisson's equation and Maxwell-Boltzmann distribution, with next conditions:

- Ions are not influenced by the perturbation potential.
- The potential energy  $|e\delta V|$  is much smaller than the thermal energy of electrons, thus  $|e\delta V| \ll k_B T_e$ .
- Electrons have Maxwell-Boltzmann distribution.

The potential in the 1-dimensional space is given by

$$\Delta V(r) = \frac{\partial^2 V(r)}{\partial r^2} = -\frac{\rho(r)}{\epsilon_0} = -e \frac{(n_i - n_e)}{\epsilon_0}. \quad (2.6)$$

While the ions are not influenced by the perturbation potential due to their heavy mass, the ion density  $n_i$  is constant, one can note as  $n_0$ . The electrons density under the local potential is  $n_e(x) = n_{e0} \exp[\frac{e\delta V}{k_B T_e}]$ , where  $n_{e0}$  is the electron density in the intrinsic plasma bulk which should be equal to that of ions:  $n_{e0} = n_i = n_0$ . Since the condition requires that  $|e\delta V| \ll k_B T_e$ , Second order Taylor approximation can be taken, and the expression of the local electron density becomes  $n_e(x) = n_0 [1 + \frac{e\delta V}{k_B T_e}]$ . The poisson equation eq. (2.6) can be rewritten as

$$\Delta V(r) = \frac{\partial^2 V(r)}{\partial r^2} = -e \frac{(n_0 - n_0 [1 + \frac{e\delta V}{k_B T_e}])}{\epsilon_0} = \frac{e^2 n_0}{\epsilon k_B T_e}. \quad (2.7)$$

The boundary conditions are

$$V(0) = \delta V, \quad (2.8)$$

$$V(\infty) = 0. \quad (2.9)$$

The second order partial differential equation eq. (2.7) can be resolved as

$$V(r) = \frac{e}{4\pi\epsilon_0 r} \exp\left(-\frac{r}{\sqrt{\frac{k_B T_e \epsilon_0}{e^2 n_e}}}\right), \quad (2.10)$$

from where, one can define

$$\sqrt{\frac{k_B T_e \epsilon_0}{e^2 n_e}} \equiv \lambda_{DL} \quad (2.11)$$

as the Debye length.[1, 15, 24, 25]

### 2.1.5 Continuity equation

Electrons and ions are created by ionisation in the bulk of plasma and lost by diffusion and recombination.[1, 15, 24, 25] Particle conservation requires the continuity equation:

$$G_{\text{ioni}} - L_{\text{Loss}} - \nabla(n_i \mathbf{v}_i) = \frac{\partial n_i}{\partial t}, \quad (2.12)$$

where  $G_{\text{ioni}}$  and  $L_{\text{Loss}}$  are volume generation and volume loss rate of ion-electron pair respectively. Generation of ion-electron is due to ionisation collision, which could be expressed by

$$G_{\text{ioni}} = \nu_i n_e, \quad (2.13)$$

where  $\nu_i$  is ionisation frequency. The loss of ions and electrons in volume is due to recombination which is often neglected in cold plasmas due to its low ionisation degree,[24] thus  $L_{\text{recombi}} = 0$ .  $n_i \mathbf{v}_i$  is the flux of ions that can be noted as  $\mathbf{\Gamma}_i = n_i \mathbf{v}_i$  When the plasma gets steady state, the term  $\frac{\partial n_i}{\partial t} = 0$ . The continuity equation becomes:

$$\nabla \mathbf{\Gamma}_i = \nu_i n_e. \quad (2.14)$$

## 2.2 Collision

Plasmas contain various species of elementary particles as electrons, ions, neutral atoms/molecules, radicals *etc.* as mentioned above. All species of elementary particles doing thermal movement collide to each others. While the collision, if the internal energy of the atom/molaicules is not changed, the collision is called elastic. Thermal energy transmission occurs between the elementary particles participating the elastic collision. In the other hand, if the internal energy of the atom/molaicular is changed by the collision, the collision is called inelastic collision. A transmission of energy between kinetic energy and internal energy of the atom/molaicules occurs while the inelastic collision.[24, 1] Although in reality collisions occur between two or multiple moving elementary particles, in analysis of two body collision, the model is often simplified to consider a projectile having a speed  $v_{\text{coll}}$  collides to a stationary target. The collision speed  $v_{\text{coll}}$  equals to the relative speed between the two elementary particles before the collision.

### 2.2.1 Cross section of collision

While a collision, there is an critical area around the target. If the projectile strike to the area, the collision occurs. If the projectile pass by out of the area, there is not collision. This area is the cross section of the collision. The crosse section is a function of kinetic energy of the projectile for the specific target and collision, noted as  $\sigma_{\text{coll}}(E_{\text{Proj}})$ .

### 2.2.2 Mean free path and collision frequency

Mean distance that a elementary particle can move without collision called mean free path, which is given by

$$\lambda_{\text{free}} = \frac{1}{n_{\text{target}} \sigma_{\text{coll}}}, \quad (2.15)$$

where  $n_{\text{target}}$  and  $\sigma_{\text{coll}}$  are the density of the target species and the maximum cross section of all collision, respectively. The mean free path is a critical value to determine whether an area is collisional or collisionless by comparing with the geometric dimension. If the velocity of the projectile is  $v_{\text{proj}}$ , then the mean time between two successive collision is [24]

$$\tau_{\text{coll}} = \frac{\lambda_{\text{free}}}{v_{\text{proj}}}. \quad (2.16)$$

The inverse is the collision frequency

$$\nu_{\text{coll}} = \frac{1}{\tau_{\text{coll}}} = n_{\text{target}}\sigma_{\text{coll}}v_{\text{proj}}. \quad (2.17)$$

The collision frequency is the number of collision occurring with in unite time.

### 2.2.3 Main collisions in low pressure cold plasma

Inelastic collision are mainly discussed

#### Atomic collisions

When the collision of electron/atom, if the free electron having an energy overcome the gap of the quantized energy level of the atom, the extranuclear of the atom can be excited to higher level or break the bond of the atom to be a free electron. Those collision are excitation and ionization, respectively.

- Excitation:  $A + e \rightarrow A^* + e$
- Ionization:  $A + e \rightarrow A^+ + 2e$

The spontaneous relaxation of the excited atoms is the main source of the light emission, and the ionization is the main source of the ions and free electrons.

#### Molecular collisions

Inelastic collisions of electron/molecule or molecule/molecule can interact to the molecular bound. The bound structure leads molecules have quantized energy levels of vibrational and rotational motion. An electron having kinetic energy overcomes the energy gap can excite the energy level of vibration/rotation. That is the vibration and rotation excitations. [24, 5] Note the molecule as AB, then the vibration and rotation excitations can be expressed as

$$e + AB(E_{\text{vib}} = 0) \rightarrow AB(E_{\text{vib}} > 0) + e, \quad (2.18)$$

and

$$e + AB(E_{\text{Rot}} = 0) \rightarrow AB(E_{\text{Rot}} > 0) + e, \quad (2.19)$$

where  $E_{\text{vib}}$  and  $E_{\text{Rot}}$  are energy level of vibration and rotation, respectively. The excited vibration and rotation motion can loss its energy by collision with other atoms/molecules. This is the vibration or rotation relaxation collision.

The molecular bound can be broken when the collision with an electron having enough energy, that is the dissociative collision.



When the electron is attached by the broken bound, the collision is the dissociative attachment.



## 2.3 Ambipolar diffusion

Fluid particles have tendency of free diffusion: to diffuse from high density area to low density area by the effect of thermodynamic. Note the fluid particle flux as  $\mathbf{\Gamma} = n\mathbf{u}$ , where  $n$  and  $u$  represent density and directed speed. Diffusion equation is

$$\mathbf{\Gamma} = -D\nabla n. \quad (2.22)$$

$D$  is diffusion coefficient, which is defined as  $D = k_B T / (m\nu_m)$ , where  $m$  and  $\nu$  are mass and collision frequency of the fluid particle respectively. Diffusion coefficient  $D$  has a relation with mobility  $\mu$  as

$$\mu = \frac{|q|}{k_B T} D, \quad (2.23)$$

where  $q$  is electric charge of the fluid particle. That is so-called Einstein relation.

In plasmas bulk electrons and ions initially have tendency to diffuse from ionisation area to walls. Higher temperature and smaller mass of electrons than that of ions lead the diffusion coefficient of electrons to be much higher than that of ions. Electrons initially diffuse more rapid than ions, that create electric field in the plasma bulk. Under the influence of the electric field, ions are accelerated, and electrons are slowed down, until the flows of electrons and ions to be equal, the diffusion reach a steady stat. The flows of electrons and ions in steady stat are

$$\mathbf{\Gamma}_e = -\mu_e n_e \mathbf{E} - D_e \nabla n_e \quad (2.24)$$

and

$$\mathbf{\Gamma}_i = \mu_i n_i \mathbf{E} - D_i \nabla n_i, \quad (2.25)$$

where  $\mathbf{E}$  is the electric field, index  $e$  and  $i$  represent parameters of electrons and ions respectively. The electric field can be resolved from the equation  $\mathbf{\Gamma}_e = \mathbf{\Gamma}_i$  as

$$\mathbf{E} = \frac{D_i - D_e}{\mu_i + \mu_e} \frac{\nabla n}{n}. \quad (2.26)$$

The ambipolar flow  $\mathbf{\Gamma} = \mathbf{\Gamma}_e = \mathbf{\Gamma}_i$  can be expressed as

$$\mathbf{\Gamma} = -\frac{\mu_i D_e + \mu_e D_i}{\mu_i + \mu_e} \nabla n. \quad (2.27)$$

If one note

$$D_a = \frac{\mu_i D_e + \mu_e D_i}{\mu_i + \mu_e}, \quad (2.28)$$

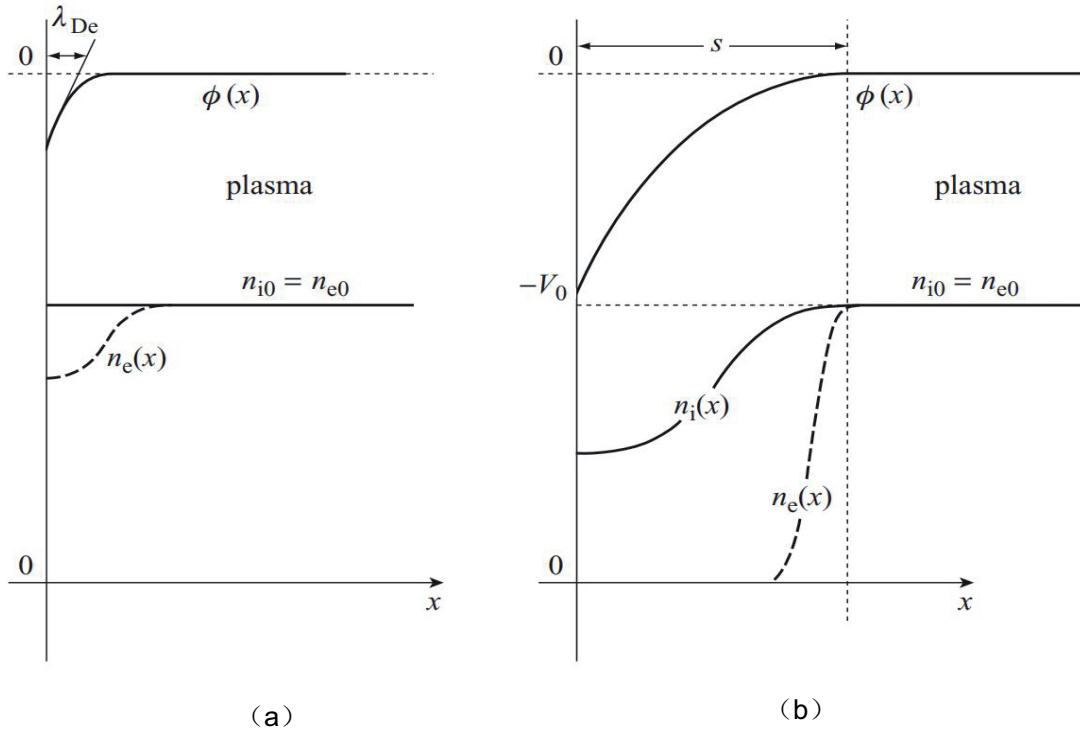


Figure 2.1: Schematic of the sheath structure for: (a) a small potential perturbation, in this case ion density is considered constant. (b) a larger potential drop, in this case electron depletion occurs and ion density decreases across the sheath.[1]

as the ambipolar coefficient, the expression of the ambipolar flow take a form of diffusion equation

$$\Gamma = -D_a \nabla n. \quad (2.29)$$

That called ambipolar diffusion.

Although the form of ambipolar diffusion equation is similar than that of free diffusion, one have to pay attention that free diffusion will not change the directed speed of diffusion particles, but under the ambipolar diffusion regime, ions are accelerated, *i.e.* ions get directed speed.

## 2.4 Plasma sheath

Plasmas in contact with solid body form a non-electro-neutral layer called plasma sheath. The formation of plasma sheath is caused by the inequality of the thermal speed between electrons and ions. In order to maintain the electro-neutrality in the bulk of plasma, electric field is created to confine electrons and cause a positive plasma potential. The plasma sheath plays a role of transition area from bulk of plasma to the walls and to shield the effect of the potential drop caused by the

solid body in plasmas or walls around plasmas. The potential drop through the sheath from plasma potential  $V_p$  to the mass potential if the walls are grounded, or to the floating potential  $V_f$  if the walls are isolated. Electric field is created due to the potential drop. The electric field in the sheath is often stronger than that in the bulk of plasmas due to the ambipolar diffusion. Electrons can only penetrate into a thin layer of the sheath, and in the most part of the sheath electrons can be neglected, thus the depletion of electron.[1, 15, 24, 25](Fig. 2.1)

### 2.4.1 Bohm sheath criterion

An estimation of ion directed speed in the edge of sheath can be dealt by the Bohm sheath criterion.[1, 15, 24, 25] That is the condition to form a positive ion sheath by considering ions are accelerated by the electric field in the sheath without collision. The Bohm sheath criterion requires that

$$v_i \geq v_B = \sqrt{\frac{k_B T_e}{m_i}}, \quad (2.30)$$

where  $v_B$  is called Bohm speed. The ions are accelerated in a so called pre-sheath to obtain the Bohm speed at the edge of the sheath. The pre-sheath is a region where have electro-neutrality  $n_i = n_e$ . Potential drop gradually in the pre-sheath, which results a electric field. Note that the electron/ion density and potential as  $n_i = n_e = n_0$  and  $V_0$  at the potion where ions have not directed speed, the electron/ion density and potential at the sheath edge as  $n_i|_s = n_e|_s = n_s$  and  $V_s$  where ions get Bohm speed  $v_B$ . The energy conservation equation could be written as

$$\frac{1}{2} m_i v_B^2 = -e(V_s - V_0). \quad (2.31)$$

The Boltzmann relation requires that

$$n_s = n_e|_s = n_0 \exp\left(\frac{-e(V_s - V_0)}{k_B T_e}\right) = n_0 \exp\left(\frac{1}{2}\right) = 0.61n_0. \quad (2.32)$$

### 2.4.2 Child-Langmuir law

The sheath structure could be determinate by Child-Langmuir law[1, 15, 24, 25] with assumptions of:

- Electron depletion in the sheath.
- Non zero ion flow remain constant in the sheath.

In the sheath, acted by the electric field, directed ion velocity is much higher than its thermal velocity, one dimensional structure could be taken. The electron depletion assure that there is not ionisation neither recombination in the sheath, so that the ion current should be constant, it is given by

$$J_i = en_i(x)v_i(x) = 0.6en_0v_B = constant, \quad (2.33)$$

where  $J_i$ ,  $n_i(x)$ ,  $v_i(x)$ ,  $n_0$  are ion current density, one dimensional ion density and ion velocity distribution function, and ion density in the bulk of plasma. The poisson equation in the sheath becomes

$$\frac{\partial^2 \phi(x)}{\partial x^2} = -\frac{en_i(x)}{\epsilon_0}, \quad (2.34)$$

where  $\phi(x)$  is the one dimensional distribution function of electric potential.

According to gas pressure, ion velocity should be discussed by two cases: low pressure and high pressure. In low pressure case, collision less regime should be taken into account, ions are accelerated by the electric field. Energy conservation equation could be established

$$\frac{1}{2}m_i v_i^2(x) + e\phi(x) = \frac{1}{2}m_i v_B^2. \quad (2.35)$$

In high pressure case, ohm law could be taken

$$v_i(x) = \mu_i E = \mu_i \frac{\partial \phi(x)}{\partial x}. \quad (2.36)$$

In low pressure collision less case, one can resolve the differential equation by combine eq. (2.33),(2.34) and (2.35). In high pressure case, the sheath structure can be found by resolving the differential equation by combine eq. (2.33),(2.34) and (2.36). The one dimensional potential function  $\phi(x)$  could be resolved. Then, the electric field and ion density could be found by:

$$E(x) = -\frac{\partial \phi(x)}{\partial x}, \quad (2.37)$$

and

$$n_i(x) = \frac{\epsilon_0}{e} \frac{\partial E(x)}{\partial x}. \quad (2.38)$$

## 2.5 Solid body in plasma

In plasma bulk, electrons and ions have significant thermal motion. A solid body penetrated in plasma bulk will be collided by electrons, ions, radicals and other neutral particles. The collision by electrons and ions lead a charge transmission from the plasma bulk to the solid body. The solid body receive charges but usually do not emit unless the case of secondary emission. In low temperature plasma, electron temperature is much higher than ion temperature, electrons have much higher speed of thermal motion. Electrons reach firstly to the surface of the solid body and give it negative potential. The negative potential repel new coming electrons. When the potential reach a value which lead the electron and ion flow to the surface to be equal, the system reach steady state. The potential called floating potential.

Under the consideration of Maxwell-Boltzmann distribution for ions and electrons, the flow of electrons forwarding the solid body can be expressed as

$$\Gamma_e = \frac{1}{4}n_e A \left[ \frac{8k_B T_e}{\pi m_e} \right]^{\frac{1}{2}} \exp\left[ \frac{e(V_f - V_p)}{k_B T_e} \right], \quad (2.39)$$

where  $A$ ,  $n_e$ ,  $V_f$ ,  $V_p$  are the surface area, electron density in the bulk of plasma, floating potential and plasma potential respectively. The expression  $\left[ \frac{8k_B T_e}{\pi m_e} \right]^{\frac{1}{2}}$  represent the thermal velocity of electron.

The expression of the ion flow depends on the dimension of the solid body.

### 2.5.1 Sheath model

For the big surface as like the pin of langmuir probe *e.g.*, the structure of the sheath around the surface is same as that around the walls and electrodes. The Bohm speed  $u_B = \sqrt{\frac{k_B T_e}{m_i}}$  should be taken for

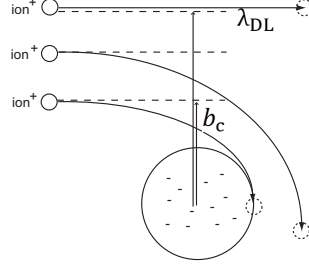


Figure 2.2: Schematic of orbit-limit model. Ion having speed  $v_i$  passe beside the particle can be attracted.

the ions forwarding to the surface, and the density of ions at the boundary of the sheath is  $n_s = 0.6n_i$ , where  $n_i$  is the ion density at the bulk of plasma. The ion flow is then

$$\Gamma_i = 0.6n_i A \sqrt{(k_B T_e / m_i)}. \quad (2.40)$$

### 2.5.2 Orbit-motion-limited model

For the small spherical surface as like dust particle *e.g.*, the orbit-motion-limited model(OML) should be taken. An positive ion passing by a negatively charged particle is attracted to the particle by the negative potential. As shown in Fig. 2.2, an ion having velocity  $v_i$  passes from the bulk of plasma where the potential is  $V_p$  to an cycle area of  $b_c$  in radius from the particle centre. The radius of the particle is  $r_p$ , and  $b_c > r_p$ . The ion motion is deviated by the negative charge and finally reach the particle surface which have a floating potential  $V_f$ , with modified velocity  $v'_i$ . The radius  $b_c$  can be determined by the energy and kinetic moment conservation:

$$E_{ki} + qV_p = E'_{ki} + qV_f, \quad (2.41)$$

and

$$v_i b_c = v'_i r_p, \quad (2.42)$$

where  $E_{ki}$  and  $E'_{ki}$  are kinetic energy of ion in the bulk of plasma and that when it reach the particle surface respectively. Then,  $b_c$  can be expressed as

$$b_c^2 = \frac{v_i'^2}{v_i^2} r_p^2 = \frac{E'_{ki}}{E_{ki}} r_p^2 = \left[1 - \frac{e(V_f - V_p)}{E_{ki}}\right] r_p^2. \quad (2.43)$$

In the case of a random thermal ion velocity, the kinetic energy and the thermal velocity are given by  $E_{ki} = k_B T_i$  and  $v_i = \left[\frac{8k_B T_i}{\pi m_i}\right]^{\frac{1}{2}}$  respectively. The ion flow reach the particle is

$$\begin{aligned} \Gamma_i &= 4\pi b_c^2 \frac{n_i}{4} v_i \\ &= \pi r_p^2 n_i \left[\frac{8k_B T_i}{\pi m_i}\right]^{\frac{1}{2}} \left[1 - \frac{e(V_f - V_p)}{k_B T_i}\right]. \end{aligned} \quad (2.44)$$

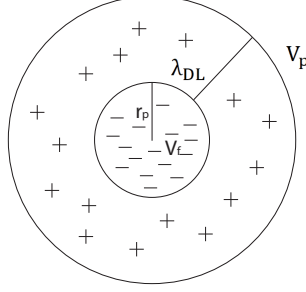


Figure 2.3: Schematic of negatively charged particle surrounded by positive ion sheath, which is characterised by the Debye length.

In the case that the directed ion velocity is dominant as at the boundary of the sheath, the kinetic energy is given by  $E_{ki} = \frac{1}{2}m_i v_i^2$ . For the unidirectional ion flow, the effective cross section is taken into account for the collection of ions, rather than the surface area. Then, the ion flow reach the particle is

$$\Gamma_i = \pi r_p^2 n_i v_i \left[ 1 - \frac{2e(V_f - V_p)}{m_i v_i^2} \right]. \quad (2.45)$$

## 2.6 Charge of dust particle in plasma

Dust particle as a solid body in plasmas gets negative charge caused by the inequality of the mobility between electrons and ions[1, 15, 24, 25, 13, 6]. When the charge  $Q$  lead the particle reach the floating potential, the flow of ions and electrons get equal, the particle gets a steady state. The charge  $Q$  can be calculated from the floating potential  $V_f$  by taking into account the sheath around the particle and the Debye length  $\lambda_{DL}$ . Figure 2.3 shows the schematic of the charged particle with a sheath whom typical length is the Debye length  $\lambda_{DL}$ . The difference of potential through the sheath is  $V_f - V_p$ . A equation can be established as

$$\int_{r_p}^{\lambda_{DL} + r_p} \frac{Q}{4\pi\epsilon_0 r^2} dr = V_f - V_p, \quad (2.46)$$

then the particle charge is

$$Q = (V_f - V_p) 4\pi\epsilon_0 r_p \left( 1 + \frac{r_p}{\lambda_{DL}} \right). \quad (2.47)$$

In the case that the particle dimension is much smaller then the Debye length ( $r_p \ll \lambda_{DL}$ ), for nanometric particles or for the particles levitating in the plasma sheath near the walls or electrodes *e.g.*, eq. (2.47) becomes the charge expression of spherical capacitor model

$$Q = (V_f - V_p) 4\pi\epsilon_0 r_p. \quad (2.48)$$

The potential difference  $V_f - V_p$  can be found from the equality of the electron and ion flow in the steady state,

$$\Gamma_e = \Gamma_i. \quad (2.49)$$

In the case that the random thermal motion of ions is dominant, eqs. (6.28) and (2.44) should be substituted into eq. (2.49), and it becomes

$$n_e \pi r_p^2 \left[ \frac{8k_B T_e}{\pi m_e} \right]^{\frac{1}{2}} \exp\left[ \frac{e(V_f - V_p)}{k_B T_e} \right] = n_i \pi r_p^2 \left[ \frac{8k_B T_i}{\pi m_i} \right]^{\frac{1}{2}} \left[ 1 - \frac{e(V_f - V_p)}{k_B T_i} \right]. \quad (2.50)$$

In the case that the unidirectional motion of ions is dominant, eqs. (6.28) and (2.45) should be substituted into eq. (2.49), and it becomes

$$n_e \pi r_p^2 \left[ \frac{8k_B T_e}{\pi m_e} \right]^{\frac{1}{2}} \exp\left[ \frac{e(V_f - V_p)}{k_B T_e} \right] = n_i \pi r_p^2 v_i \left[ 1 - \frac{2e(V_f - V_p)}{m_i v_i^2} \right]. \quad (2.51)$$

Charge neutralisation condition require that

$$-en_e + en_i + Qn_p = 0, \quad (2.52)$$

where  $n_p$  is the density of dust particles.

By combining eqs. (2.50) or (2.51) with eqs. (2.47) and (2.52), the charge of dust particles can be resolved.

### 2.6.1 Charge time

The particle charge number is determined when the particle reach floating potential. Before that the charge of particle get equilibrium, the charge variation rate is given by[8]

$$\frac{dQ}{dt} = J_e + J_i, \quad (2.53)$$

where  $J_e$  and  $J_i$  are current density of electrons and ions, which are given by  $J_e = -e\Gamma_e$  and  $J_i = e\Gamma_i$ . By taking eqs. (6.28), (2.44) and (2.47), the partial equation (2.53) becomes

$$4\pi\epsilon_0 r_p \left( 1 + \frac{r_p}{\lambda_{DL}} \right) \frac{d(V(t) - V_p)}{dt} = -en_e \pi r_p^2 v_{eth} \exp\left[ \frac{e(V(t) - V_p)}{k_B T_e} \right] + en_i \pi r_p^2 v_{ith} \left[ 1 - \frac{e(V(t) - V_p)}{k_B T_e} \right], \quad (2.54)$$

where  $v_{eth} = \left[ \frac{8k_B T_e}{\pi m_e} \right]^{\frac{1}{2}}$  and  $v_{ith} = \left[ \frac{8k_B T_i}{\pi m_i} \right]^{\frac{1}{2}}$  are thermal velocity of electrons and ions.  $V(t) - V_p$  can be noted as  $\phi(t)$ . During the charge process, the potential of the surface of the particle varies from  $V|_{t \rightarrow 0} = V_p$  to  $V|_{t \rightarrow \infty} = V_f$ . When  $V \rightarrow V_f$ , particle charge get stable and  $\frac{dQ}{dt} \rightarrow 0$ . In order to examine the time scale of charging process, the region  $V \rightarrow V_p$  should rather be taken account. In this region,  $\phi(t) \rightarrow 0$ , and the second order of Taylor approximation can be taken for  $\exp\left(\frac{e\phi(t)}{k_B T_e}\right) \sim 1 + \frac{e\phi(t)}{k_B T_e}$ . Take the charge neutralisation condition  $n_e = n_e = n_0$ . The partial equation (2.54) becomes

$$\begin{aligned} 4e\pi\epsilon_0 r_p \left( 1 + \frac{r_p}{\lambda_{DL}} \right) \frac{d(V(t) - V_p)}{dt} &= -en_e \pi r_p^2 v_{eth} \left[ 1 + \frac{e\phi(t)}{k_B T_e} \right] + en_i \pi r_p^2 v_{ith} \left[ 1 - \frac{e\phi(t)}{k_B T_e} \right] \\ \frac{d\phi(t)}{dt} &= -\frac{e^2 r_p n_0}{4\epsilon_0 \left( 1 + \frac{r_p}{\lambda_{DL}} \right) k_B} \left( \frac{v_{eth}}{T_e} + \frac{v_{ith}}{T_i} \right) \phi(t) + \frac{e r_p n_0}{4\epsilon_0 \left( 1 + \frac{r_p}{\lambda_{DL}} \right)} (v_{eth} - v_{ith}) \\ \frac{d\phi(t)}{dt} &= -\frac{1}{\tau_Q} \phi(t) + A. \end{aligned}$$

The boundary conditions are

$$Q|_{t \rightarrow 0} = 0, \quad (2.55)$$

$$Q|_{t \rightarrow \infty} = Q_{\text{eq}}, \quad (2.56)$$

$$\frac{dQ}{dt}|_{t \rightarrow \infty} = 0, \quad (2.57)$$

where  $Q_{\text{eq}}$  is the charge at steady state. The partial equation (2.55) can be resolved

$$Q(t) = Q_{\text{eq}}(1 - e^{-\frac{t}{\tau_Q}}). \quad (2.58)$$

The parameter  $\tau_Q$  can be defined as the typical time scale of the charging process of dusty particle, which is

$$\frac{1}{\tau_Q} = \frac{e^2 r_p n_0}{4\epsilon_0(1 + \frac{r_p}{\lambda_{DL}})k_B} \left( \frac{v_{\text{eth}}}{T_e} + \frac{v_{\text{ith}}}{T_i} \right). \quad (2.59)$$

In the case that the particle is enough small ( $r_p \ll \lambda_{DL}$ ) and electron temperature remain constant, the time scale can be expressed by[6, 8]

$$\tau_Q = \frac{K_{\text{plasma}}}{r_p n_0}, \quad (2.60)$$

Where  $K_{\text{plasma}}$  is a constant involving plasma parameters.

## 2.7 Forces act on dust particle in plasma

### 2.7.1 Gravitational force

In earthly laboratory, particles are permanently acted by the gravitational force. If the particle can be considered as a sphere, the gravitational force is given by[25, 13]

$$F_g = mg = \rho \frac{4}{3} \pi r_p^3 g, \quad (2.61)$$

where  $\rho$  is the mass density.

### 2.7.2 Electrostatic force

Charged particles in plasma are acted by electric force from the electric field.[25, 6]

$$F_E = QE \quad (2.62)$$

In the bulk of plasmas, the electric field is generated by ambipolar diffusion process as eq. (2.26). In the sheath of plasmas, the electric field is that of plasma sheath. If the sheath could be considered as positive ion sheath with electron depletion, the electric field could be found by the Child-Langmuir low. For a negatively charged particle, the electric force serves to confine particles.

### 2.7.3 Ion drag force

Ions in plasma are accelerated by the electric field and get directed speed  $v_i$ . Meanwhile, ions have a thermal speed

$$v_{\text{th}} = \sqrt{\frac{8k_B T_i}{m_i}}. \quad (2.63)$$

The mean speed of ions is then given by

$$v_s = \left( \frac{8k_B T_i}{m_i} + v_i^2 \right)^{\frac{1}{2}}. \quad (2.64)$$

The mean momentum of ions is

$$p_i = m_i v_s. \quad (2.65)$$

Particles in plasmas are receive directed ion flow, and momentum transfer occurs between the ion flow and particles. This momentum transfer is the cause of the ion drag force, which consists of two part: ion collection force and orbit force.

### Collection force

Collection force is caused by the momentum transfer when the ions collide to the particle.[25, 13, 6] The negatively charged particle can attract the positive ion passed near the particle. The effective crosse section of the collision is larger than the crosse section of the particle body. The radius of the effective cross section is given by eq. (7.5)

$$b_c = \left[ 1 - \frac{2e(V_f - V_p)}{m_i v_s^2} \right]^{\frac{1}{2}} r_p. \quad (2.66)$$

Consider a cylinder area with radius  $r = b_c$  and height  $h = v_i \delta t$ , where  $\delta t$  represent unit time scale. Ions in this area can collide to the particle during  $\delta t$ . The ions number in this area is

$$\begin{aligned} N_{\text{col}} &= n_i l \pi b_c^2 \\ &= n_i v_i \delta t \pi b_c^2 \\ &= \Gamma_i \pi b_c^2 \delta t. \end{aligned} \quad (2.67)$$

The total momentum transferred to the particle during  $\delta t$  is

$$p_{\text{total}} = m_i v_s \Gamma_i \pi b_c^2 \delta t. \quad (2.68)$$

Then the force by the collection of ion is[25, 13, 6]

$$F_{\text{col}} = \frac{p_{\text{total}}}{\delta t} = m_i v_s \Gamma_i \pi b_c^2. \quad (2.69)$$

### Orbit force

Ions, having directed speed  $v_i$ , passing beside particle will be attracted by its negative charge. Those ions passing outside de effective cross section will not collide to the particle but the trajectory will be modified. Momentum transfer occurs during this process. This momentum transfer causes the orbit force, which is given by[25, 13, 6]

$$F_{\text{orb}} = m_i v_s \Gamma_i 4\pi b_{\pi/2}^2 \frac{1}{2} \ln \left( \frac{\lambda_{\text{DL}}^2 + b_{\pi/2}^2}{b_c^2 + b_{\pi/2}^2} \right), \quad (2.70)$$

where  $b_{\pi/2}$  is the impact factor which is given by

$$b_{\pi/2} = \frac{eQ}{4\pi\epsilon m_i v_s^2}. \quad (2.71)$$

The total ion drag force is

$$F_{\text{id}} = F_{\text{col}} + F_{\text{orb}}. \quad (2.72)$$

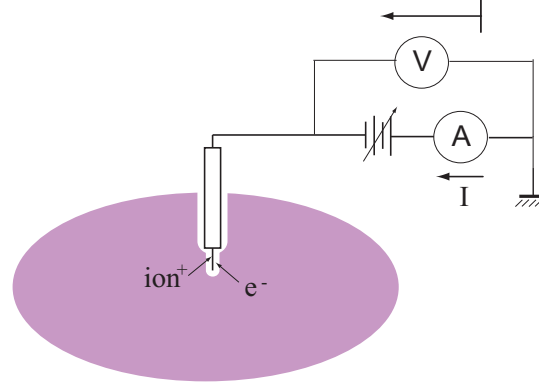


Figure 2.4: Schematic of the single langmuire probe.

## 2.8 Diagnostic of plasma parameters

### 2.8.1 Single probe method

The principle of the langmuir probe is to insert a polarised metallic body into the plasma, and estimate plasma parameters from the current-voltage curve. (Fig. 2.4) A single langmuir probe has a polarised pin referenced to the mass. The langmuir probe can measure the local parameters of plasmas, it could be used to determine spatial distribution of plasma parameters. Figure 2.4 represents the schematic. The probe pin as a solid body inserted into the bulk of plasma will attract ions and electrons then forme sheath around it self. If one takes into account the Bohm sheath criterion and define the current from mass to the plasma as positive direction, the current created by ion and electron flow toward the probe pin could be given by

$$I_i = -0.6eAn_iu_B, \quad (2.73)$$

and

$$I_e = eAn_e \left[ \frac{k_B T_e}{2\pi m_e} \right]^{\frac{1}{2}} \exp \left[ \frac{e(V - V_p)}{k_B T_e} \right], \quad (2.74)$$

where  $A$  and  $V$  are the surface of the probe pin and the polarisation potential that could be controlled by the measurement system. For the ideal model, the ion current is not influenced by the probe potential, while the electron current varies exponentially. One should note that eq. (2.74) is available only when  $V < V_p$ , at the region  $V > V_p$  electron current gets saturate.

The current that could be measured is the total current of ion and electron

$$\begin{aligned} I(V) &= I_i + I_e \\ &= I_i + eAn_e \left[ \frac{k_B T_e}{2\pi m_e} \right]^{\frac{1}{2}} \exp \left[ \frac{e(V - V_p)}{k_B T_e} \right]. \end{aligned} \quad (2.75)$$

#### Determination of $T_e$

One can see from eq. (2.75) that for the region  $V \ll V_p$  the electron current  $I_e \rightarrow 0$ , and  $I(V) \approx I_i$ . This is the saturate ion current region. The ion current  $I_i$  could be read. The electron current is then

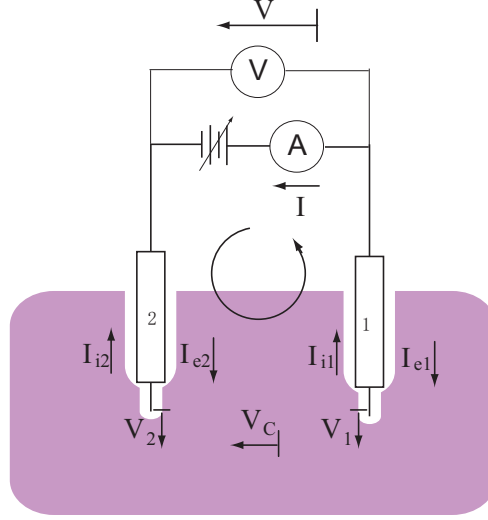


Figure 2.5: Schematic of the double langmuire probe.

given by

$$I_e(V) = I(V) - I_i. \quad (2.76)$$

Take logarithm for both side of eq. (2.74), and note that  $\gamma(V) \equiv \ln I(V) - I_i$ , one gets

$$\begin{aligned} \ln I_e &= \ln \left[ eAn_e \left( \frac{k_B T_e}{2\pi m_e} \right)^{\frac{1}{2}} \right] + \frac{e(V - V_p)}{k_B T_e}, \\ \gamma(V) &= \frac{e}{k_B T_e} V + \text{constant}. \end{aligned} \quad (2.77)$$

This is a linear function of  $V$ . By applying linear regression, the sloop  $\frac{e}{k_B T_e}$  could be found, then the electron temperature  $T_e$  could be obtained.

#### Determination of $n_i$

Substitute the obtained  $T_e$  to eq. (2.73), the ion density  $n_i$  could be found

$$n_i = - \frac{I_i}{0.6eA \sqrt{\frac{k_B T_e}{m_i}}}. \quad (2.78)$$

### 2.8.2 Double probe method

Double langmuir probe consists of two pins inserted in the bulk of plasma.[1, 15] The two floating pins are polarised reciprocally, and the current-voltage curve can be read by a measurement system. Advantage to use two pins instead of a single one is to reduce the perturbation from the measured system. Figure 2.5 represents the schematic of the double Langmuir probe. Figure 2.6 represents a typical current-voltage curve, which is symmetric to the zero point. One can define 3 region from this curve as marked in the figure, in the regions (I) and (III), ion current gets saturate, the ion current could be found from this region.[1, 15]

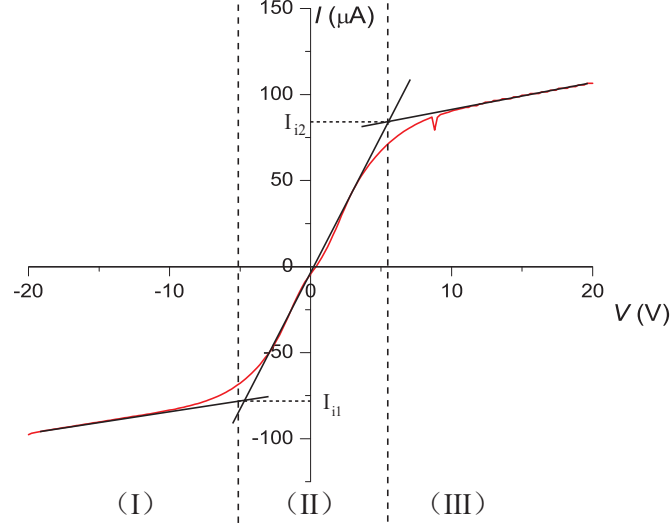


Figure 2.6: An example of current-voltage curve of the double langmuire probe. (I) and (III) are ion current saturation areas, where ion saturation current could be determined.

### Logarithmic plot method

The floating pins without polarisation in the bulk of plasmas act as a isolated solid body. Note one of the pins as pin 1 and the other as pin 2. the potential difference of the pin 1 to the local potential of the plasma could be noted as  $V_1$ , and that of the pin 2 to the local potential as  $V_2$ . One can take into account of the potential difference between the local points where inserted the pin 1 and pin 2 as  $V_C$ . The polarisation voltage that one can read from the measurement system is noted as  $V$ . Note the ion and electron current reach the pin 1 as  $I_{i1}, I_{e1}$ , and that of reach the pin 2 as  $I_{i2}, I_{e2}$ . Apply the Kirchoff's circuit low,[1, 15]

$$|I_{i1}| + |I_{i2}| = |I_{e1}| + |I_{e2}|, \quad (2.79)$$

and

$$V_1 + V_C = V_2 + V. \quad (2.80)$$

Equation 2.79 shows that the magnitude of electron currents is limited by ion current. This assure that electron currents will not saturate. Thus, eq. (2.79) could be expressed as

$$|I_{i1}| + |I_{i2}| = A_1 j_{01} \exp\left[-\frac{eV_1}{k_B T_e}\right] + A_2 j_{02} \exp\left[-\frac{eV_2}{k_B T_e}\right], \quad (2.81)$$

where  $A_1, A_2, j_{01}, j_{02}$  are the surface of pin 1 and pin 2, the saturate electron current at the local point of pin 1 and pin 2 respectively. Equation (2.80) could be written as

$$V_1 = V + V_2 - V_C. \quad (2.82)$$

Substitute eq. (2.82) to eq. (2.81),

$$|I_{i1}| + |I_{i2}| = A_1 j_{01} \exp\left[-\frac{eV}{k_B T_e}\right] \exp\left[-\frac{eV_2}{k_B T_e}\right] \exp\left[\frac{eV_C}{k_B T_e}\right] + |I_{e2}|, \quad (2.83)$$

$$= \frac{A_1 j_{01}}{A_2 j_{02}} |I_2| \exp\left[-\frac{eV}{k_B T_e}\right] \exp\left[\frac{eV_C}{k_B T_e}\right] + |I_{e2}|. \quad (2.84)$$

By taking logarithm, one obtains

$$\ln\left(\frac{|I_{i1}| + |I_{i2}|}{|I_{e2}|} - 1\right) = -\frac{e}{k_B T_e} V + \ln\left(\frac{A_1 j_{01}}{A_2 j_{02}}\right) \frac{eV_C}{k_B T_e} \quad (2.85)$$

Define that the current direction from pin 1 to pin 2 to be positive, the measurable current  $I$  is then expressed as

$$I = |I_{e2}| - |I_{i2}|. \quad (2.86)$$

So that  $|I_{e2}| = I + |I_{i2}|$ . One can note

$$\gamma'(V) \equiv \ln\left(\frac{|I_{i1}| + |I_{i2}|}{I + |I_{i2}|} - 1\right). \quad (2.87)$$

Then one gets a linear function of  $V$

$$\gamma'(V) = -\frac{e}{k_B T_e} V + \text{constant}. \quad (2.88)$$

By applying linear regression, the sloop  $-\frac{e}{k_B T_e}$  could be determined.

### Equivalent resistance method

Equivalent resistance method is one of quick calculation methods[15], which is diverged from the deduction of the eq. (2.84). If one thinks about the slop of the current-voltage curve at the point  $V = 0$  by taking the relation of eq. (2.86), one can obtain

$$\left.\frac{dI}{dV}\right|_{V=0} = \left.\frac{dI_{e2}}{dV}\right|_{V=0}. \quad (2.89)$$

The electron current  $I_{e2}$  can be deduced from eq. (2.84) as

$$I_{e2} = \frac{|I_{i1}| + |I_{i2}|}{\frac{A_1 j_{01}}{A_2 j_{02}} \exp\left(-\frac{eV_2}{k_B T_e}\right) + 1}. \quad (2.90)$$

Note

$$\sigma \equiv \frac{A_1 j_{01}}{A_2 j_{02}}. \quad (2.91)$$

$\sigma$  can be deduced from eq. (2.85) as

$$\sigma = \left(\frac{|I_{i1}| + |I_{i2}|}{|I_{e2}|} - 1\right)\bigg|_{V=0} = \frac{|I_{i1}| + |I_{i2}|}{|I_{i2}|} - 1. \quad (2.92)$$

Then

$$\left.\frac{dI}{dV}\right|_{V=0} = \frac{\sigma(|I_{i1}| + |I_{i2}|)}{(\sigma + 1)^2} \frac{e}{k_B T_e}. \quad (2.93)$$

Electron temperature can be deduced

$$T_e = \frac{e}{k_B} \frac{\sigma(|I_{i1}| + |I_{i2}|)}{(\sigma + 1)^2} \left. \frac{dV}{dI} \right|_{V=0}. \quad (2.94)$$

Here the factor  $\left. \frac{dV}{dI} \right|_{V=0}$  takes the form of resistance, it is denoted the equivalent resistance  $R_0 \equiv \left. \frac{dV}{dI} \right|_{V=0}$ . This method can easily estimate the electron temperature from 3 points of the current-voltage curve: negative and positive ion saturated current and slop of the current-voltage curve at  $V = 0$ . It prevents the laborious calculation of the logarithmic plot method.

### Intercept Method

Intercept method is another quick calculation method[15]. While the equivalent resistance method require the slop at the zero point, the intercept method permits us to choose by ourself two effective points for the calculation. This method can be used when some error occurs around the zero point.

Equation (2.84) can be rewritten as

$$V = -\frac{k_B T_e}{e} \ln \left[ \frac{1}{\sigma} \left( \frac{|I_{i1}| + |I_{i2}|}{I + |I_{i2}|} - 1 \right) \right]. \quad (2.95)$$

One can choose two points from the current-voltage curve, note as  $(V_1, I_1)$  and  $(V_2, I_2)$ . Note

$$F(I) = \frac{|I_{i1}| + |I_{i2}|}{I + |I_{i2}|}. \quad (2.96)$$

By substituting  $(V_1, I_1)$  and  $(V_2, I_2)$  to eq. (2.95), one obtain equations

$$\begin{cases} V_1 = -\frac{k_B T_e}{e} \ln \left[ \frac{1}{\sigma} (F(I_1) - 1) \right] \\ V_2 = -\frac{k_B T_e}{e} \ln \left[ \frac{1}{\sigma} (F(I_2) - 1) \right]. \end{cases} \quad (2.97)$$

Subtracting  $V_1$  by  $V_2$ , one obtain

$$V_1 - V_2 = -\frac{k_B T_e}{e} \ln \left[ \frac{(F(I_2) - 1)}{(F(I_1) - 1)} \right]. \quad (2.98)$$

Electron temperature can be deduced

$$T_e = \frac{V_1 - V_2}{\ln \left[ \frac{F(I_2) - 1}{F(I_1) - 1} \right]}. \quad (2.99)$$

The choice of the two effective points should not be too close.[15] Indeed, this is a special case when only two points are used for the logarithmic plot method.

### 2.8.3 Electron density measurement by microwave resonance cavity

Microwave resonance measurement method is one of principle methods to determine the electron density of plasmas. In this method, the microwave resonance effect is produced in the reactor chamber. The frequency of the resonance wave is related to the free electron density. By comparing the resonance frequency with and without plasma, the electron density can be deduced (Figure 2.7). Compared to the Langmuir probe, the microwave resonance method allows to determine plasma electron density without

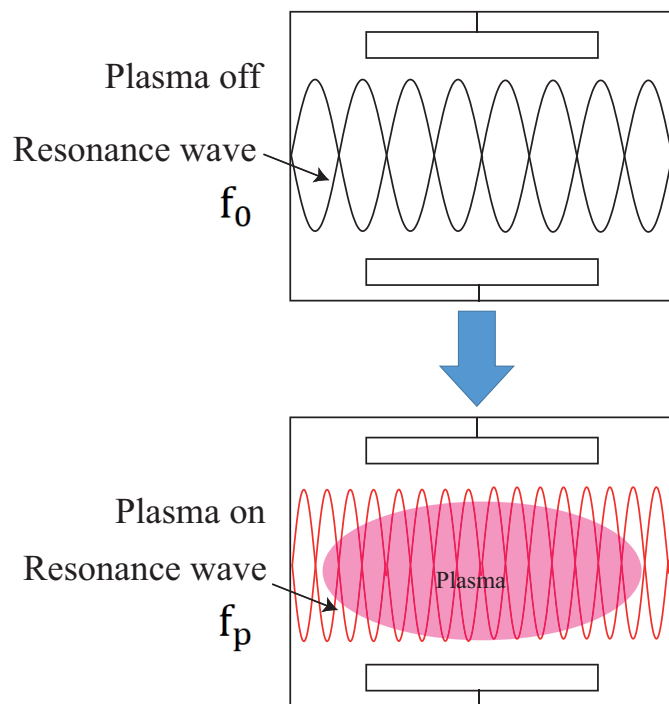


Figure 2.7: Schematic of the microwave resonance measurement method. Reactor chamber is treated as a resonant cavity, to detect the first harmony of resonance frequency with and without plasma.

disturbing the plasma. The disadvantages are that it requires that the plasma chamber should be a resonant metallic cavity for microwave and it can only measure the average value of the electron density of whole plasma.[6]

When the microwave propagates into a resonant cavity, the resonance effect can occur due to the geometry of the cavity and the permittivity for several incident wave frequency

$$f_{\text{mnp}} = \frac{C}{2\pi\sqrt{\mu\epsilon}}K(m, n, p), \quad (2.100)$$

where  $f_{\text{mnp}}$ ,  $C$ ,  $\mu$ ,  $\epsilon$  and  $K(m, n, p)$  are the resonance frequency, light speed, relative permeability, relative permittivity and geometrical function. In a specific cavity, the geometrical function  $K(m, n, p)$  is constant. In the bulk of plasma without magnetic field, the relative permeability  $\mu$  remains constant. The relative permittivity is influenced by the presence of the plasma and incident wave, which is given by

$$\epsilon = \epsilon_r \left(1 - \frac{n_e e^2}{2\pi f^2 m_e \epsilon_0}\right) \epsilon_e. \quad (2.101)$$

where  $f$  is the frequency of incident wave.

Resonance wave are measured with and without plasma by function generator and oscilloscope, note as  $f_p$  and  $f_0$ . They can be written, by taking eq. (2.100), as

$$f_p = \frac{C}{2\pi\sqrt{\mu\epsilon_r\epsilon_0}}K(m, n, p), \quad (2.102)$$

$$f_0 = \frac{C}{2\pi\sqrt{\mu\epsilon_0}}K(m, n, p). \quad (2.103)$$

By combining eqs. (2.102), (2.103) and (2.101), the electron density can be found as

$$n_e = \frac{2\pi(f_p^2 - f_0^2)\epsilon_0 m_e}{e^2}. \quad (2.104)$$

Thus, the mean electron density is determined.

## 2.9 French summery

Ce chapitre a été consacré à un état de l'art dans le domaine des plasmas poussiéreux. Ainsi les rappels présentés ont concerné les théories de bases qui ont été utilisées dans les études menées dans cette thèse. Ainsi les modèles fluide et OML sont présentés. Les différentes forces agissant sur les particules et qui déterminent leur comportement dans le plasma sont rappelées. Les méthodes et les outils de diagnostic du plasma et des particules tel que la cavité résonnante, la sonde électrostatique de Langmuir, sont décrits.



# Bibliography

- [1] P. Chabert and N. Braithwaite, *Physics of Radio-Frequency Plasmas*, (Cambridge Univ. Press, Cambridge, 2011).
- [2] P. K. Shukla, A. A. Mamun, *Introduction to Dusty Plasma Physics*, (IOP series of plasma Physics, 2002).
- [3] M. A. Liberman, A. J. Lichtenberg, *Principles of plasma discharges and materials processing*, (Wiley-Interscience Publication, 1994).
- [4] A. Bouchoule, *Dusty plasmas Physics, Chemistry and Technological Impacts in Plasma Processing*, (Wiley-Interscience Publication, Orleans, 1999).
- [5] A. A. Fridman, L. Boufendi, T. Hbid, B. V. Potapkin, and A. Bouchoule, *J. Appl. Phys.* **79**, 1303 (1996).
- [6] M. Henault, Ph. D. thesis, University of Orleans, Orleans, (2015).
- [7] M. S. Barnes, J. H. Keller, J. C. Forster, J. A. O'Neill, and D. K. Coultas, *Phys. Rev. Lett.* **68**, 313 (1992).
- [8] A. V. Ivlev, M. Kretschmer, M. Zuzic, G. E. Morfill, H. Rothermel, H. M. Thomas, V. E. Fortov, V. I. Molotkov, A. P. Nefedov, A. M. Lipaev, O. F. Petrov, Yu. M. Baturin, A. I. Ivanov, and J. Goree, *Phys. Rev. Lett.* **90**, 5 (2003).
- [9] E. O. Johnson, and L. Malter, *Phys. Rev.* **80**, 1 (1950).



# Chapter 3

## Experiment setup

### 3.1 Particle formation experiments

Low-pressure RF  $C_2H_2$ -Ar plasmas were used for the experiments of particle formation. In experiments, gas temperature could be controlled by a temperature regulation system: heated by electric heater and cold down by liquid nitrogen. Self-bias of plasma was observed by oscilloscope and averaged electron density was measured by microwave resonance cavity method.

#### 3.1.1 Plasma chamber

Plasmas were generated in a grounded cylindrical box of 13 cm inner diameter, which is equipped with a shower-type powered electrode (Fig. 3.1). The bottom of the box was closed with the grid of 20% transparency. This allows a vertical laminar flow of gases at the operating conditions. A cylindrical heater surrounds the discharge box, liquid nitrogen is flowed into a copper tube surrounding the cylindrical oven. The gas temperature is varied from room temperature up to 200°C and measured in the gas flow just below the bottom grid by thermocouple.

#### 3.1.2 Generator system

A "Cesar 133" radio frequency generator and an L-type LC matching box are used for the plasma ignition. As the particle formation is also sensitive to the discharge power, a stable generator and a good match point are very important for the experiment. An older generator was used but because of the instability of the power supply, it has been changed to a new and more stable one.

#### 3.1.3 Gas injection system

In this work, 3 types of gases will be used: Ar,  $C_2H_2$  and  $O_2$ . Ar and  $O_2$  come from the laboratory gas lines and  $C_2H_2$  comes from a dedicated gas bottle. A gas mass-flow controller can regulate the flux for each gas. After passing through the mass-flow controller, the gas will be mixed and injected into the chamber. Figure 3.2 shows the gas lines.

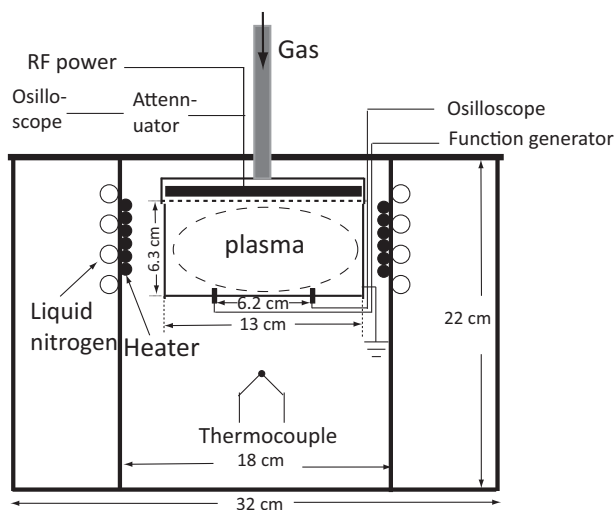


Figure 3.1: Schematic of experimental setup. The plasma box is put into the inner vessel for heating and cooling gases which is thermally isolated by the outer chamber.

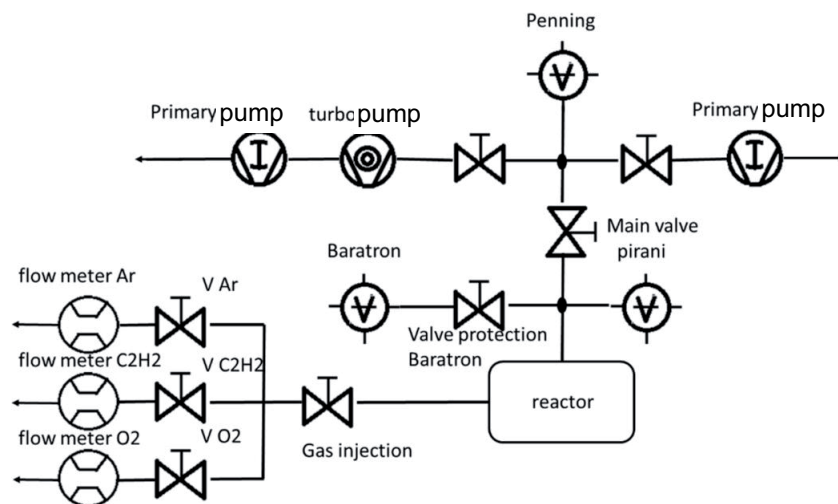


Figure 3.2: Schematic of gas feeding and pumping system.

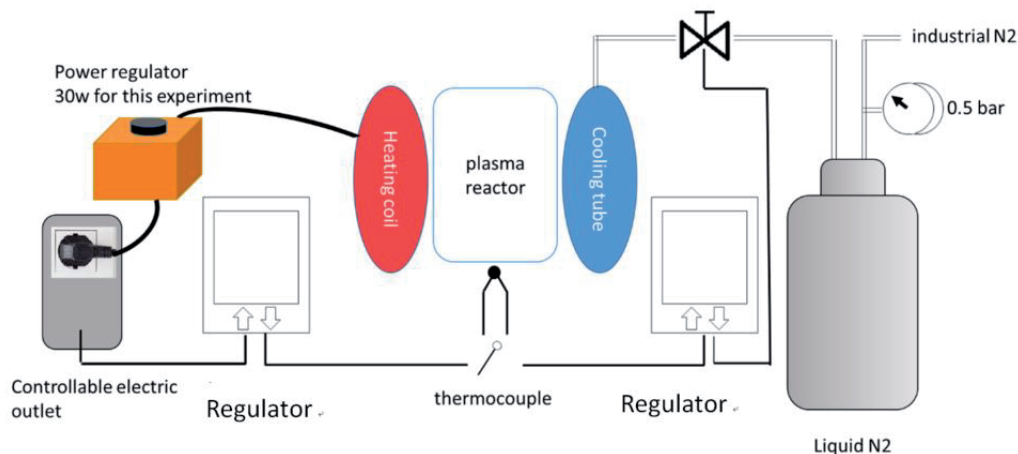


Figure 3.3: Schematic of temperature regulation system.

### 3.1.4 Pumping system

This chamber has two pumping lines: primary pumping line and secondary pumping line side by side. A primary pump can pump the chamber to primary vacuum, and then there is a switch allowing passing the chamber to the secondary pumping line, which consists of another primary pump next to a turbo-molecular pump. A valve from the chamber protects Baratron gauge.

### 3.1.5 Temperature regulating system

In order to regulate the temperature, there are a heating part and a cooling part surrounding the chamber (Fig. 3.3). The heating part consists of an electric power supply and a programmable thermometer related to a thermocouple located inside the reactor. The electric power supplier, type of ATOMS-A5040PX, is connected to the heating coil in the chamber as described above. It delivers a power controllable AC output power with 50 Hz of frequency and 40 V of voltage. To fix the temperature, a control part is needed. A thermocouple measures the gas temperature at the exit of the inner chamber. It is connected to the programmable thermometer, Type of EURPTHERM-FC1310002765, control an electric outlet to which the electric power supplier is connected. When the gas temperature is lower than setting temperature, the electric outlet is connected, when the gas temperature is above the setting temperature, the thermometer will control the electric outlet, let it to be disconnected so the electric power supplier can stop and heating coil can stop heating. For this reactor, a constraint of the thermo-resistance of the rubber joint limit the highest temperature to 100 °C. In the cooling processes, a tank of liquid N<sub>2</sub> is used as the refrigerant. Another programmable thermometer for the low temperature range is used to regulate the temperature. Same as the first one, it measures the gas temperature at the exit of the discharge box and it control the valve of liquid N<sub>2</sub>.

### 3.1.6 Diagnostics tools

The self-bias voltage and the electron density are the two main parameters we focused on in this work. The self-bias voltage can be measured through a filter and an attenuator using an oscilloscope. The electron density will be measured with the microwave resonance method by a signal generator.

The microwave generator can output a signal by periodically sweeping its frequency surround the resonance frequency, for this chamber it is 1631 MHz. The signal is to be sent to the inner box of the reactor through an antenna. At the bottom of the inner box of the reactor, two antennas were symmetrically placed to the centre, with a distance of 6 cm to each other. The microwave signal is sent to one antenna and received by the other after having resonance with the chamber.

In order to analyze the frequency of microwave signal, a reference saw tooth signal is used to synchronise the measurement. It indices the start and end frequencies of the frequency sweeping.

The three signals: the self-bias voltage, the resonated microwave signal and the frequency indicate signal are monitored and recorded by the Tektronix DPO 7254 oscilloscope, which has 4 channels and is able to save the data via USB port. The signals are both DC coupled with 1 M $\Omega$  input resistance. There is an electron density simulated cord programmed by Dr.Goëtan WATTIEAUX.

## 3.2 Particle behaviours experiments

Experiments to determine particle behaviours in the plasma were performed in a PK-3 plus plasma chamber.[14, 12] The PK-3 is a laboratory originally designed for the investigation of the dusty plasma under micro gravity on board of the international space station. Its design has several advantage for the investigation such as the vast filed of view, smaller temperature gradient, more access ports for particle injectors or probes *ect.*[14, 12] In this theses, the plasma chamber of PK-3 laboratory was used with several modification of the configuration. (Fig. 3.4)

### 3.2.1 PK-3 plus chamber

The plasma chamber has 4 flank side walls in glass. The top and bottom sides are aluminum plates. The dimension of the chamber is 10 $\times$ 10 $\times$ 5.4 cm. The intrinsic chamber has a symmetric configuration for top and bottom sides. Both electrode can be powered by the RF power. When one is powered, the other is grounded. Two circular aluminum electrodes of 60 mm in diameter are set face to face on the center of top and bottom sides respectively. Each electrode is surrounded by a grounded aluminum ring of 15 mm in width. The distance between the electrodes is 30 mm. 4 ports are opened on each grounded ring, that allow the installation of particle injectors and the access of electric probes. The electrodes are thermally coupled to the chamber walls by an insulator of hight thermal conductivity, in order to prevent the temperature gradient between the electrodes and the structure.[14, 12] All components are fabricated from hight conductivity material (aluminum) and thermally coupled. That can prevent the temperature gradient within the discharge space, which is symmetrically enclosed by those thermally coupled components. The influence of the thermophoretic force is so that minimised.

The dimension of bottom electrode can be modified by superposing a smaller electrode on the intrinsic one. A larger grounded ring combined with the new electrode is put on the intrinsic electrode

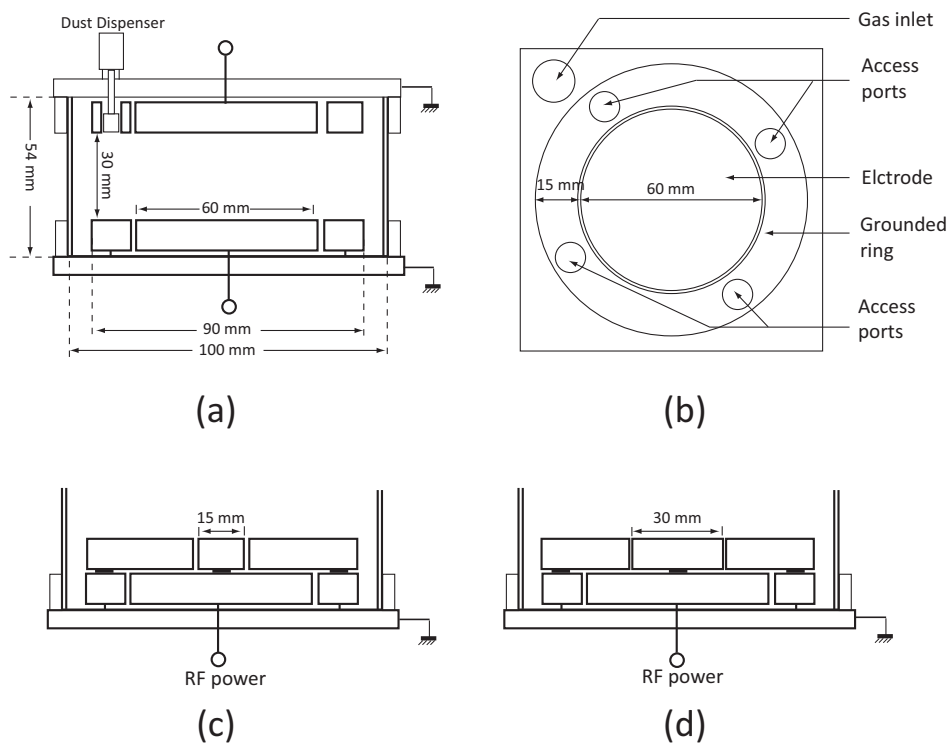


Figure 3.4: (a) Cross sectional view of the intrinsic PK-3 plus chamber with a dispenser of the dust particles. (b) Top view of the intrinsic PK-3 plus chamber. (c) Modification of the size of the bottom electrode to 15 mm in diameter. (d) Modification of the size of the bottom electrode to 30 mm in diameter.

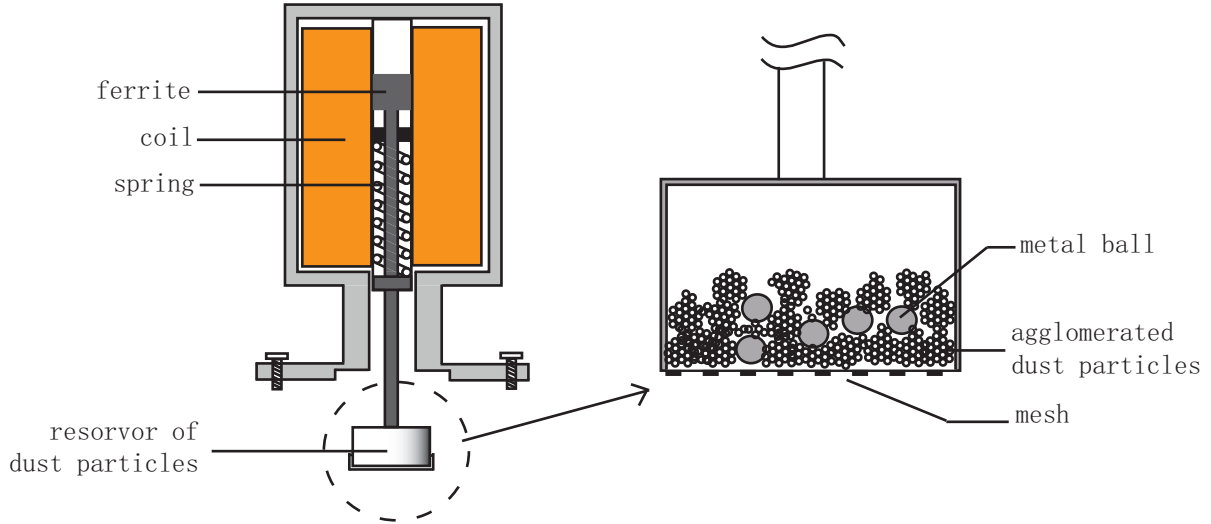


Figure 3.5: Cross sectional view of the particle injector with a zoomed view the reservoir of dust particles.

with a insulant. In the case of the modification of the bottom electrode, the distance between the top and the bottom electrodes become to 25 mm. The bottom electrode could be changed to a 15 cm and a 30 cm ones in diameter. (Fig. 3.4 (c) and (d))

### 3.2.2 Particle dispenser

Two dispensers of particles were set on the top of the PK-3 chamber.[3] (Fig. 3.5) The dispensers consists of a reservoir of dust particles and an agitation part. The reservoir contains dust particles with several metal ball of 1 mm in diameter inside. The bottom of the reservoir is closed by a mesh which is larger than the diameter of the contained particles. The agitation part consists of a movable ferrite surrounded by a coil, and connected to the reservoir by a spring. The reservoir was penetrated in the chamber. The particles agglomerate inside the reservoir so that they can be supported by the mesh although the last one is larger than the particles. When the injection, the coil is magnetised by a direct current, and the movable ferrite is stimulated. The reservoir is then agitated by the ferrite and the spring during the direct current. The metal balls inside of the reservoir can serve to crash the agglomeration of the dust particles, and then the deagglomerated particles fall down through the mesh into the chamber.

The direct current to shake the injector was supplied by a pulse generator (Fig. 3.6). Pulse period and pulse width could be regulated in order to regulate the shaking time of the injector. The amount of the injected particle could be roughly controlled. Larger the pulse width was, more the particles could be injected.



Figure 3.6: Front view of the pulse generator which is used to control the injection of the dust particles.

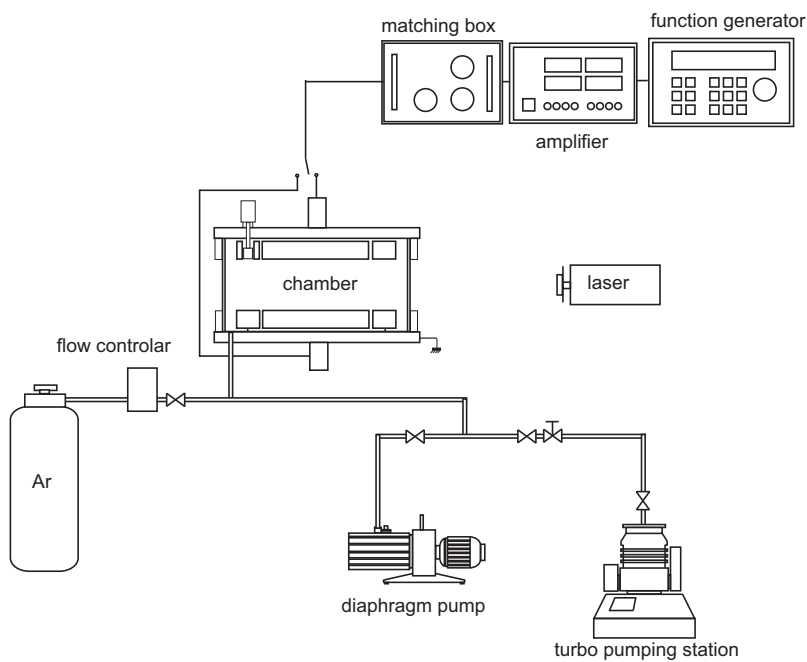


Figure 3.7: Schema of the laboratory with PK-3 plus chamber for experiments of the examination of the particle behaviours.

### 3.2.3 Gas and electric connection

The PK-3 chamber was supplied RF power by a function generator and an amplifier through a matching box. Argon gas was used as ambience gas. There was only one gas inlet on the PK-3 plus chamber was used, that can assure that there is not gas flow inside the chamber when the pressure reach stable. Gas flow was controlled by a SEC-E40 gas flow controller (Fig. 3.7 (a)). The gas controller has control range of 10/20/30/50/100/300/500/ SCCM (Standard cubic centimeter per minute) and 1/2/3/5/10 SLM (Standard litre per minute). Flow rate control rang is 2~100%, control accuracy is  $\pm 1\%$ . A Baratron type 722A Absolute Pressure Transducer was set near the gas inlet of the chamber to monitor the gas pressure (Fig. 3.7 (b)). A MVP 020-3 AC diaphragm pump by PFEIFFER VACUUM was used to create a primary vacuum (Fig. 3.7 (c)). The diaphragm pump has a nominal pumping speed 1.4 m<sup>3</sup>/min and a maximum exhaust pressure 1100 mbar. A HiCube 80 Eco turbo pumping station by PFEIFFER VACUUM was used to create a secondary vacuum (Fig. 3.7 (d)). The turbo pumping station consists of a turbo pump of HiPace 80 and a specially matched backing pump MVP 015-2. A schema of the laboratory is shown in Fig. 3.7.

### 3.2.4 Function generator and amplifier

A WF-1946B multifunction synchronizer was used as the function generator to generate RF signal and pulse-time modulation function (Fig. 3.9). It can generate sinusoidal waves, square waves, triangular waves, saw tooth waves, arbitrary waveforms, noise, and DC. Its oscillation frequency can be set from 0.01 Hz to 15 MHz. Frequency setting resolution is 0.01  $\mu$ Hz. The multifunction synchronizer has two signal channels. Each channel can be set independently and then the two signals can be coupled to one output signal. In the experiments, channel 1 was set to sinusoidal wave at 13.56 MHz, which is the RF signal for the generation of the RF discharge. Peak to peak voltage was as regulation parameter. Channel 2 was reserved for the pulse-time modulation, which was set to duty cycle variable rectangular waves, wave frequency and pulse duty cycle were regulation parameters. The maximum output peak to peak voltage of the multifunction synchronizer is 20 V, setting resolution is 1 mV. The output voltage is too low to ignite RF discharge, A Thamway 145T-4766ADU RF amplifier was used to amplify the output signal of the function generator (Fig. 3.10). The frequency band of the amplifier is 10 ~ 30 MHz, the maximum output power was 50 W. The amplifier has an output channel of the amplified RF power and two monitoring channel with -40 dB for the forward and reversing signal. The output signals with -40 dB can be monitored by a oscilloscope. The gain of amplification in this experimental configuration was nearly 10000 times for power, therefore 100 times for amplitude of voltage.

### 3.2.5 Optic system

A laser type of NEO-50SG by NEOARK was used to illuminate the dust particles in plasmas (Fig. 3.12). The laser consists of a head of laser diode (Fig. 3.12 (a)) and a Q-switch power supplier (Fig. 3.12 (b)). The laser beam was 532 nm in wavelength and 50 mW in maximum mean power.

The laser light scattered by dust particles was received by a CCD (Charge-coupled device) camera from an orthogonal direction to the laser beam. Two type of CCD were used depending on situations. A colour CCD camera type of WAT-231S2 by Watec was used to observe and to determine the levitation



(a)



(b)



(c)



(d)

Figure 3.8: (a) Gas flow controller. (b) Baratron gauge. (c) Diaphragm pump. (d) Turbo pumping station. A combination of a turbo pump and a backing diaphragm pump.



Figure 3.9: Front view of the WF-1946B multifunction synthesizer.



Figure 3.10: Front view of the Thamway 145T-4766ADU RF amplifier.



Figure 3.11: The front panel of the Agilent B2901A precision source/measurement unit.



(a)



(b)

Figure 3.12: Laser of NEO-50SG. (a) laser head by laser diode. (b) power supply of Q-switch.

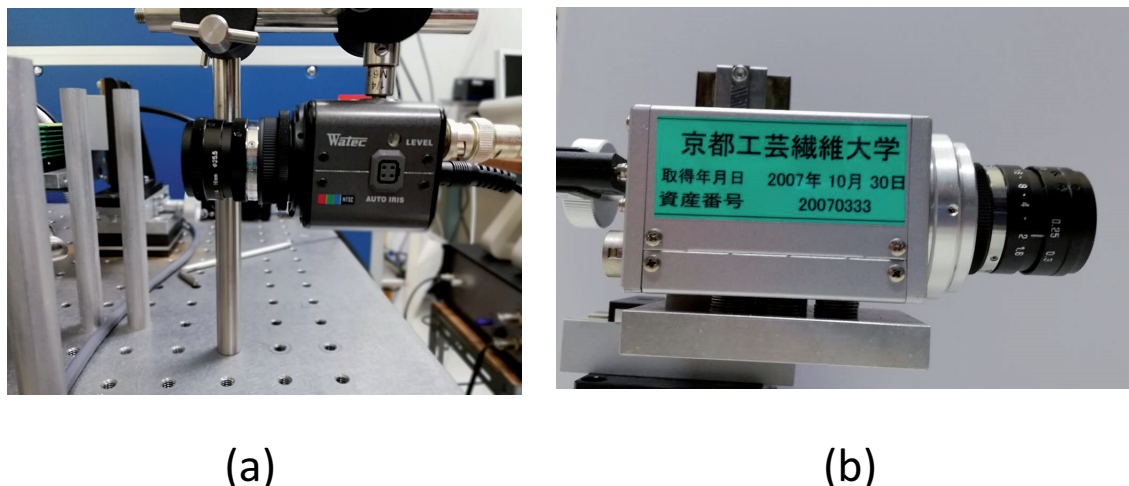


Figure 3.13: (a) Colour CCD camera WAT-231S2. (b) Monochrome high speed camera K-II.

of dust particles (Fig. 3.13 (a)). It has resolution of  $768(H) \times 494(V)$ , with pixel size  $6.35(H) \times 7.4(V)$   $\mu\text{m}$ . A monochrome high speed camera type of K-II by KATO KOKEN was used to observe particle dynamic (Fig. 3.13 (b)). Frame rate could be set from 50 to 1000 FPS (Frame per second).

### 3.2.6 Double probe method

A double langmuir probe could be set into the chamber from the access port on the top side, as shown in Fig. 3.14. The probe was made by two tungsten wires enwrapped by insulating. Two naked tips situated at the end of the probe. The size of tips was 0.35 mm in diameter, 8 mm in length. Two tips were separated 7 mm from each other. The probe has a form like the letter "L". The tips at the end of the probe could reach the center of the chamber. The probe was movable in vertical direction. The tips could sweep along the centre axis from bottom to top. The displacement of the probe was monitored by a vernier scale with a resolution of 0.1 mm.

A B2901A precision source/measurement unit by Agilent was used for the measurement of double probe method. The unit consists of a function generator as the source part and a measurement part which could measure the voltage and current. There are 6 connection ports to adapt both 2-wire and 4-wire measurement. The 2-wire connection mode was used during ore experiments, and the low terminal connection was set to be floating. The source part could be set as voltage or current source with the maximum output power of 31.8 W. The voltage source has 4 ranges from  $\pm 200$  mV to  $\pm 200$  V. The current source has 10 ranges from  $\pm 100$  nA to  $\pm 3$  A. In the practice, output voltage and current should ensure that  $IV < 31.8$  A. The minimum resolution of the voltage as same as that of the current is 1% of the rang. For the measurements of our experiments, voltage source was used, and with the rang of  $\pm 20$  V and  $\pm 200$  V were concerned depending on plasma conditions. Measurement part has 4 ranges for the voltage measurement from  $\pm 200$  mV to  $\pm 200$  V, and 10 ranges for current

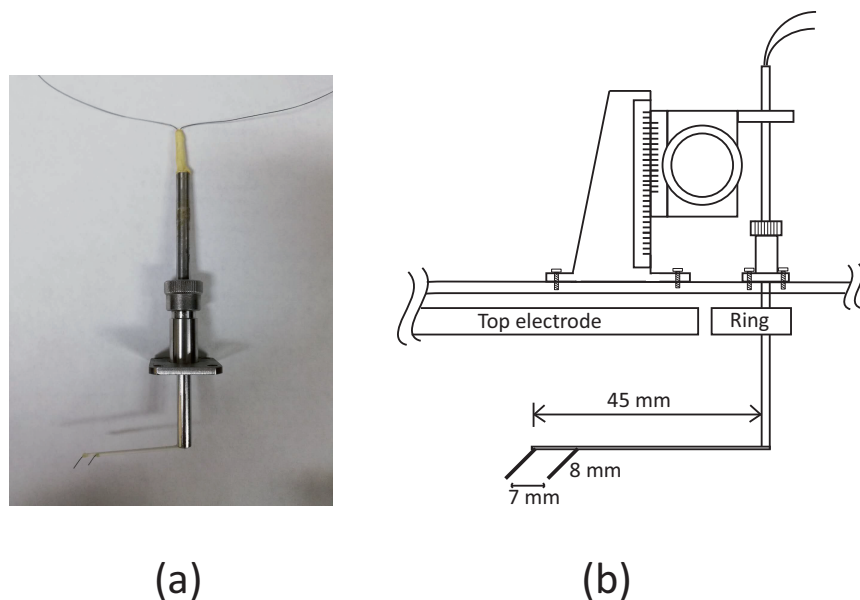


Figure 3.14: Schema of the installation of the double probe on the PK3 plus chamber (b) with a photo of the double probe (a).

measurement from  $\pm 100$  nA to  $\pm 3$  A. The resolution of voltage measurement as same as that of the current is  $10^{-6}$  of the range. For the measurements of our experiments, currents were measured in the range of  $\pm 100$   $\mu$ A with an accuracy of  $(\pm 0.02 + 25$  nA).

In order to calculate the electron temperature  $T_e$  and ion density  $n_i$  from the current-voltage curve of the double langmuir probe, a program is made by Matlab. Logarithmic plot method is taken in this program. The ion current saturation and electron current area can be distinguished automatically or manually. Often manual mode is applied. The advantage of the manual mode is to be able to exclude error data points. Figure 3.15 shows the interface of the Matlab program.

### 3.3 French summery

Les dispositifs expérimentaux mis en œuvre pour réaliser les travaux de recherche relatives aux deux parties de cette thèse sont décrits dans cette chapitre. Pour la partie de l'étude liée à la formation des particules, les expériences ont été effectuées au laboratoire GREMI (Orléans, France). Le réacteur est de forme cylindrique et est équipé de plusieurs moyens de diagnostic en particulier d'un module de régulation de la température des gaz qui permet de contrôler la cinétique chimique pour la formation des particules. Deux paramètres clé pour le suivi des phases de formation des nanoparticules sont la tension d'auto-polarisation, que nous avons enregistré de façon continue sur un oscilloscope, et la densité électrique moyenne est mesurée par la méthode de cavité micro-onde résonnante. La description de l'ensemble est détaillée dans ce chapitre. Pour la partie de l'étude liée au comportement et au

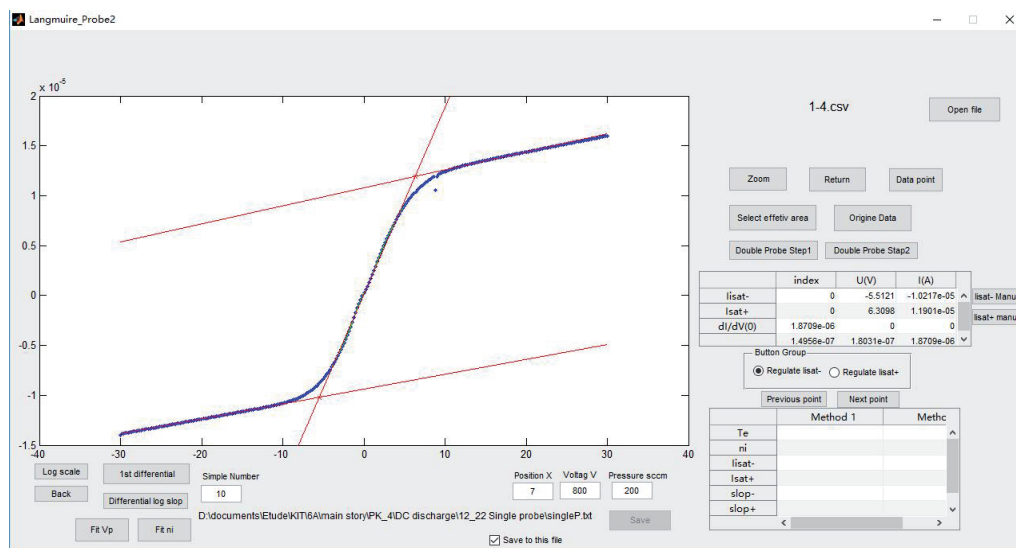


Figure 3.15: Interface of the double probe method calculation program.

transport des nuages denses de particules, les expériences ont été effectuées au KIT (Kyoto, Japon). Un réacteur du type PK3-plus avec modification a été utilisé. La température électronique et la densité ionique sont mesurées par la méthode de la double sonde de Langmuir.

# Bibliography

- [1] H. M. Thomas, G. E. Morfill, V. E. Fortov, A. V. Ivlev, V. I. Molotkov, A. M. Lipaev, T. Hagl, H. Rothermel, S. A. Khrapak, R. K. Suetterlin, M. Rubin-Zuzic, O. F. Petrov, V. I. Tokarev, and S. K. Krikalev, *New J. Phys.* **10**, 033036 (2008).
- [2] A. G. Khrapak, V. I. Molotkov, A. M. Lipaev, D. I. Zhukhovitskii, V. N. Naumkin, V. E. Fortov, O. F. Petrov, H. M. Thomas, S. A. Khrapak, P. Huber, A. Ivlev, and G. Morfill, *Contrib. Plasma Phys.* **56**, 253 (2016).
- [3] M. Boudihib, Ph.D. thesis, University of Orleans, Orleans, 2017.



## Chapter 4

# Nucleation time of nano-particles in low pressure C<sub>2</sub>H<sub>2</sub>/Ar RF plasmas

### 4.1 Introduction

In silane (SiH<sub>4</sub>) plasmas, which is one of the most reactive gases used for silicon-based devices manufacturing, a three-step-process has been proposed for formation of the dust particles.[9, 10] The process includes, (i) nucleation and formation of nanoparticles with size of around 2-3 nm, (ii) agglomeration of the nanoparticles to a size of about 50 nm, and (iii) growth to particles of few  $\mu\text{m}$  due to radical deposition on their surfaces. These steps were accurately identified in different experimental conditions. In parallel, several studies investigated influences of dust particles on the plasma and discharge parameters such as electron and ion densities, electron temperature and self-bias voltage that also affect the physical and chemical phenomena behind the formation of dust particles.[11, 12, 13, 14, 15] After the plasma ignition, negative ions are produced by dissociative attachment. These negative ions, recognized as the main nuclei for the nanoparticles formation, initiate chain reactions with parent molecules of gas.[16, 17] The first small nuclei can grow up to form nanoparticles with a critical size around 2-3 nm.[12] The nanoparticles formed in this step are still small, however they slightly affect the discharge and properties of plasmas. When the nanoparticles reach to a critical concentration (about  $10^{11}$  to  $10^{12}$   $\text{cm}^{-3}$ ), agglomeration occurs and they can grow up very rapidly with size up to about 50 nm.[11, 12] During this phase, the dust particle charge up by electron attachment and when they reach this size the Coulomb repulsion stops the agglomeration. Thus the plasmas and discharge parameters are strongly modified. This second step can be clearly identified by observing the time evolution of several parameters such as self-bias voltage, electron density, optical emission from the plasma and the intensity of scattered light by the particle.[11, 12, 13] In the third step, the agglomerated particles grow up to micrometer by sticking of radicals on their surfaces.[12, 13]

In this work, we focus our interest on the first step. We measured time where the transition between the first and second phases occurs. This time gives a clear indication on the nanoparticles nucleation in low pressure C<sub>2</sub>H<sub>2</sub>/Ar RF plasmas. This step is very sensitive to the experimental conditions such as gas temperature, and has been already observed for formation of silicon particles in SiH<sub>4</sub>/Ar

plasmas.[9, 10, 12, 14, 18] The nucleation of carbon particles is analyzed with referring to the kinetic model for the  $SiH_4/Ar$  plasmas. An analytical solution of the nucleation time is derived and four coefficients are found to give the best fit based on the kinetic model. In addition to the temperature, effects of gas pressure and discharge power on the nucleation are discussed in the model including nanoparticle dynamics of diffusion and charging, which show good agreement for the nucleation time with that obtained in the experiments.

## 4.2 Experimental

In the experiments, the gas temperature is varied from room temperature up to  $200^\circ C$  and measured in the gas flow just below the bottom grid by thermocouple. For gas temperature below  $0^\circ C$ , liquid nitrogen is flowed into a copper tube surrounding the cylindrical oven, which is obviously stopped. Microwave resonant cavity method was used for measurements of electron density.[14, 19, 20] It gives an average value of the electron density over all the plasma volume. The time evolution of self-bias voltage is recorded during the nanoparticles nucleation and growth. In this work, the self-bias voltage was the main parameter to accurately determine the time where occurs the transition from the nucleation phase to the agglomeration one. This parameter is directly related to the charged species that are collected on the powered electrode mainly electrons and positive ions. It allows detecting appearances of nanoparticles in the plasmas.[21, 22] In fact, the nanoparticles appearing in the plasma gas phase affect the electron collision frequency and thus the electron flux to the powered electrode is modified.

In experiments, temperature was changed from 267 to 375 K. Pressure and discharge power were set from 40 to 80 Pa and from 6 to 20 W, respectively. Gas mixture ratio of  $[C_2H_2]$  to  $([C_2H_2]+[Ar])$  was 0.02. After each sequence of measurement, the plasma box is cleaned with oxygen plasma to remove film deposited on wall inside the box to avoid any drift of the discharge impedance.

## 4.3 Results and Discussion

Dependence of electron density on discharge power was studied with pure Ar plasmas before the experiments of particle formation. A microwave resonant cavity method was applied to measure electron density. Spatial mean value of electron density could be obtained with the method. As shown in Fig. 4.1, power dependence of electron density is linear. At different pressure, intercepts of the linear fit have slightly shifted. One can linearly fit the electron density as  $n_e = aP_{RF} + bP + c$ . The  $n_e$ ,  $P_{RF}$  and  $P$  are electron density, discharge power and gas pressure, respectively. The  $a, b, c$  are constant coefficients.

Figure 4.2 shows time evolution of self-bias voltage observed for  $C_2H_2/Ar$  plasma. The self-bias voltage,  $V_{dc}$  appears immediately when a plasma is ignited, and the absolute value of the self-bias voltage  $|V_{dc}|$  slightly decreases with time. Decreasing of  $|V_{dc}|$  is due to nanoparticle formation (a) and when the agglomeration phase starts we observe a drastic decrease of  $|V_{dc}|$  (b). This second decrease is due to the loss of electrons by attachment on the dust particles.[12, 23] This time evolution of  $|V_{dc}|$  is compared with that of the laser light transmission, which was used to detect particle formation. It was

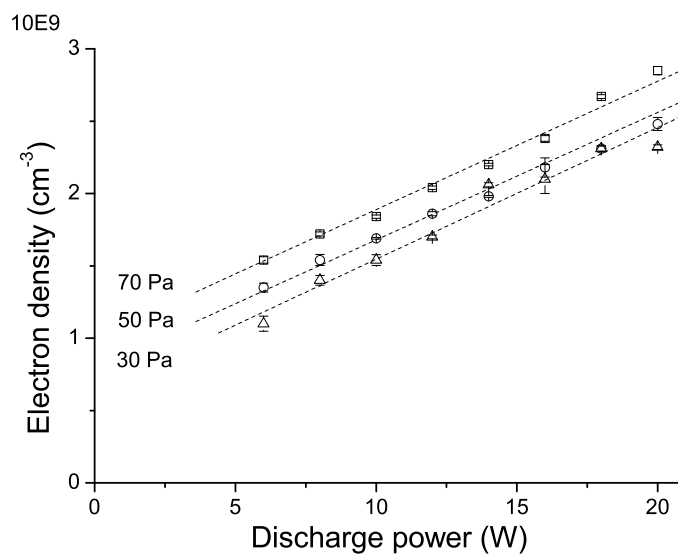


Figure 4.1: The electron density depending on the discharge power measured in pure Ar plasmas by microwave resonant cavity method at 30, 50 and 70 Pa.

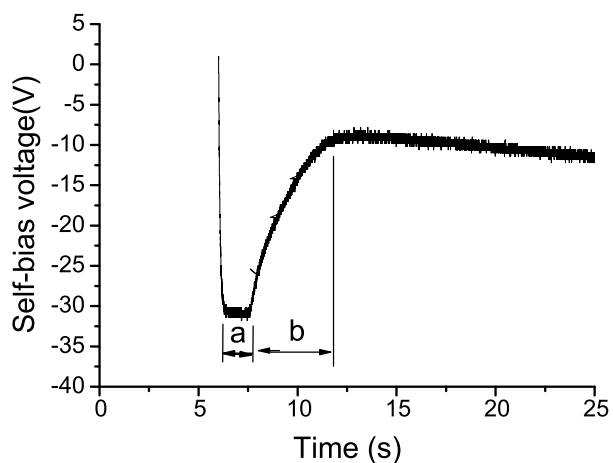


Figure 4.2: Time evolution of the self-bias voltage after ignition of a plasma. When the plasma generated, negative self-bias voltage appeared. It remained constant while the nucleation phase shown by "a" and its absolute value reduced after the agglomeration phase "b" started.

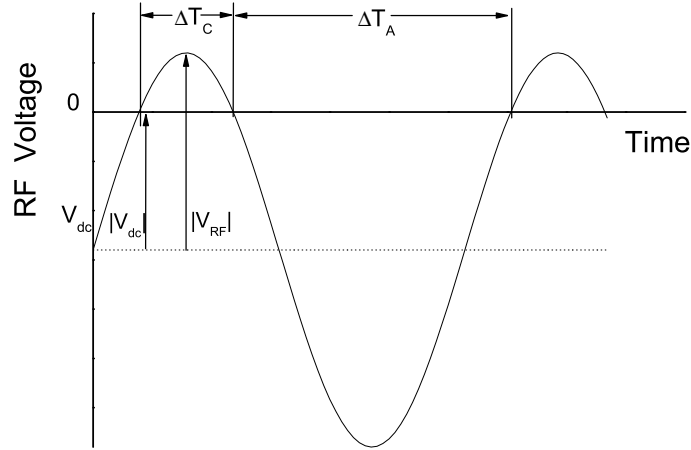


Figure 4.3: Schematic of RF voltage at a powered electrode with a self-bias voltage  $V_{dc}$ . In the capacitively coupled RF plasmas, a mean value of RF voltage is deviated from 0 V to  $-|V_{dc}|$ . The time interval during  $V_{RF} > 0$  (noted as  $\Delta T_C$ ) becomes shorter than the time interval during  $V_{RF} < 0$  (noted as  $\Delta T_A$ ). This inequality of the time duration can recompense the inequality of transport speed between electron and ion fluxes.

shown that the drastic decreasing of  $|V_{dc}|$  was found to occur at the same moment as the beginning of agglomeration.[24]

During the first few RF periods after the plasma ignitions in a capacitively coupled discharge, the self-bias voltage appears at the same time as the space charge sheaths.[25] It is caused by electrons accumulation in the coupling capacitance which is coupled in series with the powered electrode. Figure 4.3 gives the time evolution of the powered electrode after the establishment of  $V_{dc}$  and the sheaths. the  $\Delta T_C$  represents the time duration where the powered electrode behaves as a cathode ( $V_{RF} > 0$ ), and the  $\Delta T_A$  is the time duration where the powered electrode behaves as an anode ( $V_{RF} < 0$ ). In the cathode period ( $\Delta T_C$ ), electron current is collected onto the powered electrode, and the total negative charge collected during this period,  $Q_-$  can be expressed as

$$Q_- = \Delta T_C n_e \bar{v}_e S_{RF}, \quad (4.1)$$

where  $n_e, \bar{v}_e, S_{RF}$  are electron density, mean drift speed of electron during the cathode period and electrode surface, respectively. In the anode period, ion current goes toward the powered electrode, and positive charges reach to the capacitance. A total of the positive charges during this period,  $Q_+$  can be expressed by

$$Q_+ = \Delta T_A n_i v_B S_{RF}, \quad (4.2)$$

where  $n_i, v_B$ , are ion density and Bohm speed, respectively. At the steady state, in the whole RF

period, the total of the charges on the capacitance should be zero. Thus we have

$$\Delta T_C n_e \bar{v}_e S_{\text{RF}} = \Delta T_A n_i v_B S_{\text{RF}}, \quad (4.3)$$

$$\Delta T_C + \Delta T_A = 1/f_{\text{RF}}, \quad (4.4)$$

where  $f_{\text{RF}}$  is the RF frequency. An expression of  $\Delta T_C$  can be obtained as

$$\Delta T_C = \frac{1}{f_{\text{RF}} \left(1 + \frac{n_e \bar{v}_e}{n_i v_B}\right)}. \quad (4.5)$$

In Fig. 4.3, one can obtain an expression of  $|V_{\text{dc}}|$

$$\begin{aligned} |V_{\text{dc}}| &= |V_{\text{RF}}| \sin \left( \frac{\pi}{2} - \frac{\Delta T_C}{2} 2\pi f_{\text{RF}} \right) \\ &= |V_{\text{RF}}| \cos (\Delta T_C \pi f_{\text{RF}}) \\ &= |V_{\text{RF}}| \cos \left( \frac{\pi}{1 + \frac{n_e \bar{v}_e}{n_i v_B}} \right), \end{aligned} \quad (4.6)$$

where  $\Delta T_C \in \left(0, \frac{1}{2f_{\text{RF}}}\right]$ . The  $|V_{\text{dc}}|$  decreases with decreasing of electron density  $n_e$  in this regime of cosine function.

During the nucleation phase of dust particles, when their size is of a few nanometers ( $<5$  nm), [12, 26] their charge is still low and cannot exceed one elementary charge. Thus the effect of the small dust particles on the electron density can be neglected. [12, 13] Thus during nucleation,  $|V_{\text{dc}}|$  dose not change so much. when the small particles start to grow up by agglomeration, the electron density decreases significantly and this causes a drastic decrease of  $|V_{\text{dc}}|$ .

In Fig. 4.2, part "a" indicates the nucleation phase, where the self-bias voltage remains approximately constant. In this phase, negative ions such as  $\text{C}_2\text{H}^-$  are produced by dissociative attachment. They are the nucleus from which start the formation of the nanoparticles. [27] The part "b" during which  $|V_{\text{dc}}|$  substantially decreases, is related to agglomeration of the nanoparticles. These last accumulate to a critical concentration around  $10^{11}$  to  $10^{12}$  in the plasma gas phase. The average distance between two nanoparticles becomes very small and thus they start agglomerating. As soon as the agglomeration starts electron attachment becomes very important. [14] As described above, decrease of electron density leads a decrease of  $|V_{\text{dc}}|$  at the beginning of agglomeration. Here, the time interval from plasma ignition to beginning of agglomeration is called nucleation time. It is measured directly from the time evolution of the self-bias voltage. Figure 4.4 shows the nucleation time in function of the RF power at a constant pressure (60 Pa) for different gas temperatures. Figure 4.5 shows the nucleation time in function of the RF power for different pressures but keeping constant the gas temperature at 325 K. These graphs indicate that the nucleation time decreased with increasing the discharge power, which means that power depositing on the plasmas enhances chemical reactions for nucleation. In Fig. 4.6, dependence of the nucleation time on the temperature is deduced from Fig. 4.4. The nucleation time increases with increasing the temperature. This means that heating the gases slow down the chemical reactions behind the nanoparticle nucleation and growth. The same tendency as  $\text{SiH}_4/\text{Ar}$  RF plasmas is obtained in previous works. [14, 28]

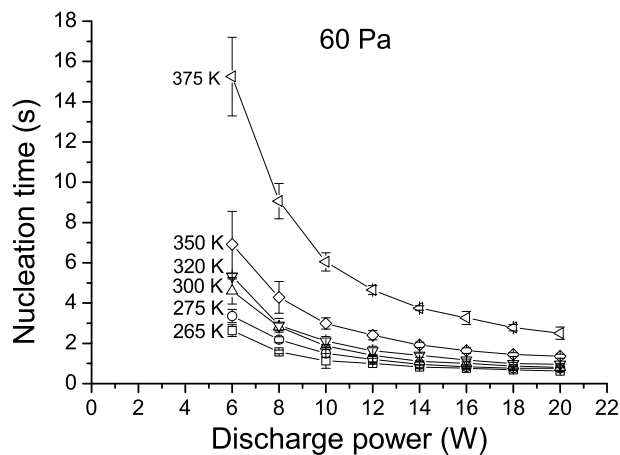


Figure 4.4: The nucleation time depending on the discharge power from 6 to 20 W as a parameter of the temperature from 265 to 375 K at a constant pressure of 60 Pa. The nucleation time decreased with increasing the discharge power.

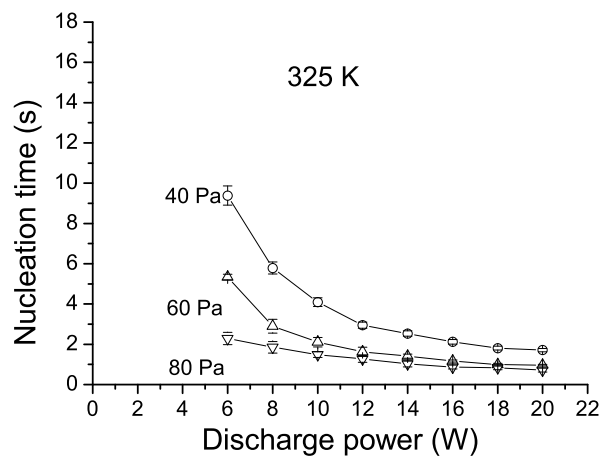


Figure 4.5: The nucleation time depending on the pressure from 6 to 20 W as a parameter of the pressure from 40 to 80 Pa at a constant temperature of 325 K. The nucleation time decreased with increasing the discharge power.

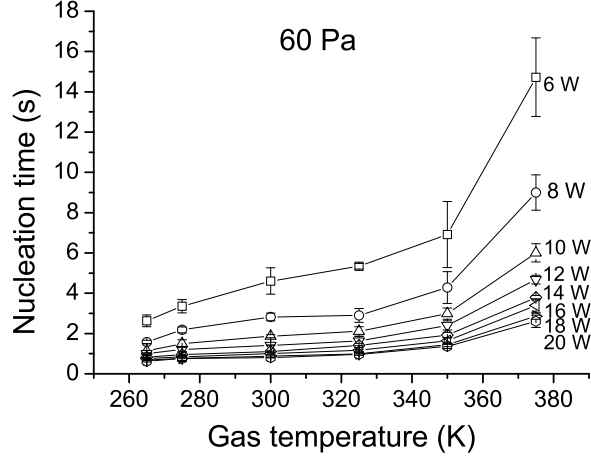
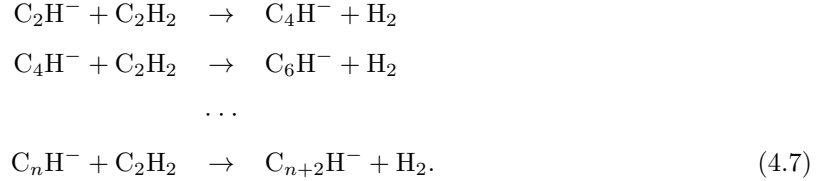


Figure 4.6: The nucleation time depending on the temperature from 265 to 375 K as a parameter of the discharge power from 6 to 20 W at a constant pressure of 60 Pa. The graph was reproduced from Fig. 4.5.

In this work, we used for  $C_2H_2/Ar$  chemistry the same kinetic model for nucleation and growth of nanoparticles as for  $SiH_4/Ar$  one.[12] Nucleation can be considered as chain reactions between  $C_2H^-$  and the parent molecule of  $C_2H_2$  with a rate constant of  $k_{i-m}$ , [16, 29]



The negative ions of  $C_2H^-$  are produced by dissociative electron attachment with a rate constant of  $k_{ad}$ , [12, 28]



Conversely, the negative ions are lost by recombination with  $Ar^+$  positive ions with a rate constant of  $k_{ii}$ ,



In the model, rates of chemical reactions for nucleation depend on vibrational energy of  $C_2H_2$  molecules. Molecules vibration excitation is due to electron collisions and is lost to kinetic energy through the collisions with abundant Ar atoms, which corresponds to vibrational-translational VT relaxation.[12, 30] The gas temperature affects the rate constant of  $k_{i-m}$ , as indicated in the following expression

$$k_{i-m} = k_0 N^{2/3} \exp \left[ - \left( \Lambda + \frac{B\Delta T}{3T_{00}^{4/3}} \right) - P_{VT} N^{2/3} \right], \tag{4.10}$$

where

$$\Delta T = T - T_{00},$$

and

$$\Lambda = \ln \left[ \left( k_{VT}[C_2H_2] + k_{VT}[Ar] + P_{VT} \frac{D}{R^2} \right) / (k_{ev}n_e) \right]. \quad (4.11)$$

In the formulae,  $k_0$ ,  $N$ ,  $B$ ,  $T$ ,  $T_{00}$ ,  $P_{VT}$ , and  $n_e$  are a constant, atomic number of C<sub>n</sub>H<sup>-</sup> being  $n + 1$ , the Landau-Teller parameter, temperature, room temperature of 300 K, VT relaxation parameter, and electron density in plasmas, respectively. The  $\Lambda$  describes effects of electron impact consisting of contribution and loss of vibration energy in the VT relaxation of C<sub>2</sub>H<sub>2</sub> molecules with Ar and walls, where  $k_{VT}$  is the VT relaxation rate coefficient can be considered equal to  $10^{-12}$  for C<sub>2</sub>H<sub>2</sub>,  $D$  is a diffusion coefficient, and  $R$  is a characteristic distance to the walls, in accordance with the experimental conditions in which  $D = 3 \times 10^3$  cm<sup>2</sup>/s and  $R = 3$  cm, and  $[C_2 H_2]=0.02 \times ([C_2H_2]+[Ar])=\eta n_0$  (hereafter, gas mixture ratio of C<sub>2</sub>H<sub>2</sub> is expressed by  $\eta$ ). Taking conditions of an ideal gas, one has  $n_0 = P/(k_B T)$  where  $P$  and  $k_B$  are pressure and the Boltzmann constant, respectively. Regarding  $\Lambda$  shown by Eq. (4.11) with  $k_{VT}n_0 \gg P_{VT} \frac{D}{R^2}$  taken into account,

$$\begin{aligned} \exp(-\Lambda) &= \left[ (k_{VT}[C_2H_2] + k_{VT}[Ar] + P_{VT} \frac{D}{R^2}) / (k_{ev}n_e) \right]^{-1} \\ &= \left[ \left( k_{VT}n_0 + P_{VT} \frac{D}{R^2} \right) / (k_{ev}n_e) \right]^{-1} \\ &\simeq \frac{k_{ev} n_e}{k_{VT} n_0}. \end{aligned} \quad (4.12)$$

A characteristic time of the chain reaction  $\tau$  can be defined as

$$\tau = \frac{1}{k_{i-m}[C_2H_2]}, \quad (4.13)$$

which should be re-written according to the experimental conditions and Eqs. (4.10) and (4.12) to

$$\begin{aligned} \tau^{-1} &= k_0 N^{2/3} \exp(-\Lambda) \exp \left[ -B \frac{\Delta T}{3T_{00}^{4/3}} \right] \exp \left[ -P_{VT} N^{2/3} \right] \times \eta n_0 \\ &\simeq k_0 N^{2/3} \frac{k_{ev} n_e}{k_{VT} n_0} \exp \left[ -B \frac{\Delta T}{3T_{00}^{4/3}} \right] \exp \left[ -P_{VT} N^{2/3} \right] \times \eta n_0 \\ &\simeq \frac{\eta k_0 k_{ev}}{k_{VT}} N^{2/3} n_e \exp \left[ -P_{VT} N^{2/3} \right] \exp \left[ -B \frac{\Delta T}{3T_{00}^{4/3}} \right]. \end{aligned} \quad (4.14)$$

In a capacitively coupled discharge the electron density  $n_e$  can be considered to be proportional to discharge power  $P_{RF}$ . Thus the characteristic time of chain reaction can be expressed by

$$\tau \simeq \alpha_1 \frac{1}{P_{RF}} \exp(\beta \Delta T), \quad (4.15)$$

and the parameters  $\alpha_1$ ,  $\beta$  are given by

$$\begin{aligned} \alpha_1 &= \frac{k_{VT}}{\eta k_0 k_{ev}} N^{-2/3} \exp(P_{VT} N^{2/3}), \\ \beta &= \frac{B}{3T_{00}^{4/3}}. \end{aligned}$$

The characteristic time of reaction chain depends exponentially on the gas temperature and is inverse proportional to the RF power. Experimentally, the nucleation time, was found to depend on gas pressure. A. A. Fridmant *et al.*[12] reported that the first small particles can grow due to the reaction chain till reaching to a specific size. Above that size, negative-positive ion recombination proceeds faster than the reaction chain. The concentration of small particles increases until reaching the critical value. Here a multi-body collision process between small particles leads to their agglomeration. The total collision rate for agglomeration can be written as  $k_c = \sigma v [1 + 1/\ln(\frac{n_{\text{crit}}}{n_p})]$ , where  $n_{\text{crit}}$  is defined as the critical concentration which is proportional to  $1/\sigma R$  ( $\sigma$  is cross section of particle collision, and  $R$  is particle interaction mean radius), and  $n_p$  is the particle concentration. When the particle concentration  $n_p$  approaches to the critical value  $n_{\text{crit}}$ , the collision rate strongly increases.[12] The critical concentration is thus strongly related to  $\sigma$  and  $R$ . Furthermore, it is also reported that the critical concentration does not experimentally depend on temperature.[12] During their growth, the generated nanoparticles are submitted to two competitive phenomena: loss by thermal diffusion and trapping due their charging which causes electrostatic trapping in the plasma bulk. This means that if the diffusion time is longer than the charging time,  $t_{\text{dif}} > t_{\text{charge}}$ , the nanoparticles tend to be accumulated in the plasmas and their concentration will increase to reach the critical value which is given by

$$n_{\text{crit}} = \Delta n_{\text{reac}} \frac{t_{\text{dif}}}{t_{\text{dif}} + t_{\text{charge}}} t, \quad (4.16)$$

where  $\Delta n_{\text{reac}}$  designates the number of nanoparticles generated by the reaction chain (Eq. (4.7)) per unit time and unit of volume, and  $t$  is the time to transit from nucleation to agglomeration. The  $t_{\text{dif}}/(t_{\text{dif}} + t_{\text{charge}})$  gives residence probability of the nanoparticles in plasmas. The  $\Delta n_{\text{reac}}$  can be expressed as

$$\Delta n_{\text{reac}} = k_{i-m} [\text{C}_2\text{H}^-] [\text{C}_2\text{H}_2]. \quad (4.17)$$

The density of the negative ions can be deduced from the different contributions for their formation and their loss that are the dissociative attachment (Eq. (4.8)), the ion-ion recombination (Eq. (4.9)) and the particles nucleation reaction (Eq. (4.17)).

$$\frac{d[\text{C}_2\text{H}^-]}{dt} = k_{\text{ad}} n_e [\text{C}_2\text{H}_2] - k_{\text{ii}} [\text{Ar}^+] [\text{C}_2\text{H}^-] - k_{i-m} [\text{C}_2\text{H}_2] [\text{C}_2\text{H}^-]. \quad (4.18)$$

This differential equation can be easily resolved and the solution is

$$[\text{C}_2\text{H}^-] = \frac{k_{\text{ad}} n_e [\text{C}_2\text{H}_2]}{k_{\text{ii}} [\text{Ar}^+] + k_{i-m} [\text{C}_2\text{H}_2]} \exp\left(-\frac{t}{\tau_{\text{ad}}}\right), \quad (4.19)$$

with

$$\tau_{\text{ad}} = \frac{1}{k_{\text{ii}} [\text{Ar}^+] + k_{i-m} [\text{C}_2\text{H}_2]}. \quad (4.20)$$

The rate constants are estimated  $k_{\text{ii}} \sim 10^{-7}$  cm<sup>3</sup>/s and  $k_{i-m} \sim k_0 \sim 10^{-12}$  cm<sup>3</sup>/s [27]. Before agglomeration starts, plasma neutrality requires  $n_e = [\text{Ar}^+] + [\text{C}_2\text{H}_2^+] \sim [\text{Ar}^+]$ . Typical value of electron density in the used experimental condition is  $n_e \sim 10^9$  cm<sup>-3</sup>. The  $[\text{C}_2\text{H}_2]$  can be estimated from  $\eta P/(k_B T) \sim 10^{14}$  cm<sup>-3</sup>. Thus the order of magnitude of  $\tau_{\text{ad}}$  is  $10^{-2}$  s. The nucleation time is about 0.5 s  $\sim$  18 s in the experiments. It is clear that  $[\text{C}_2\text{H}^-]$  reaches to the steady state during the

nucleation phase and its value is

$$[C_2H^-] = \frac{k_{ad}n_e[C_2H_2]}{k_{ii}[Ar^+] + k_{i-m}[C_2H_2]}. \quad (4.21)$$

Substituting Eq. (4.21) for  $[C_2H^-]$  in Eq. (4.17) we obtain

$$\Delta n_{\text{reac}} = k_{i-m}[C_2H_2] \frac{k_{ad}n_e[C_2H_2]}{k_{ii}[Ar^+] + k_{i-m}[C_2H_2]}$$

As mentioned above, before the agglomeration phase we have  $n_e = [Ar^+] + [C_2H_2^+]$  in plasma bulk. Since  $[Ar^+] \gg [C_2H_2^+]$ , one can note  $[Ar^+]/n_e = \bar{n}_e \sim 1$ .

The diffusion and charging times are derived from thermal motion of nanoparticles in the ambient gas mainly composed of Ar, and charging by the orbit-limited model,[13, 31, 32, 33] respectively,

$$t_{\text{dif}} = \frac{3\sqrt{\pi}L^2\sigma}{2\sqrt{2}k_B} \sqrt{\frac{M}{k_B}} \frac{P}{T^{3/2}}, \quad (4.22)$$

$$t_{\text{charge}} = k_\tau \frac{\sqrt{k_B T_e}}{an_e}, \quad (4.23)$$

where  $L$ ,  $\sigma$ ,  $M$ ,  $k_\tau$ ,  $T_e$  and  $a$  are a characteristic length from the center of a plasma to the walls, a cross section for collision between the nanoparticles and Ar, mass of the nanoparticles, a constant involving ratios of mass and temperature for electron to ion, electron temperature, and radius of the nanoparticles.

The nucleation time given by the Eq. (4.16) is

$$t = n_{\text{crit}} \frac{1}{\Delta n_{\text{reac}}} \frac{t_{\text{dif}} + t_{\text{charge}}}{t_{\text{dif}}}. \quad (4.24)$$

Substituting  $k_{i-m}$  of Eq. (4.10) in the formula given by Eq. (4.22) we have,

$$\begin{aligned} \frac{n_{\text{crit}}}{\Delta n_{\text{reac}}} &= \frac{n_{\text{crit}}k_{ii}}{\eta k_{i-m}k_{ad}n_0^2\bar{n}_e} + \frac{n_{\text{crit}}}{k_{ad}n_e[C_2H_2]} \\ &= \frac{n_{\text{crit}}k_{VT}k_{ii}}{\eta k_0 N^{2/3} k_{ev} k_{ad} \bar{n}_e \exp(-P_{VT}N^{2/3}) n_0 n_e} \exp(\beta\Delta T) + \frac{n_{\text{crit}}}{\eta k_{ad} n_e n_0} \\ &= \frac{n_{\text{crit}}k_{VT}k_{ii}k_B}{\eta k_0 N^{2/3} k_{ev} k_{ad} \bar{n}_e \exp(-P_{VT}N^{2/3})} \frac{T}{n_e P} \exp(\beta\Delta T) + \frac{n_{\text{crit}}k_B}{\eta k_{ad}} \frac{T}{n_e P} \\ &= \alpha_2 \frac{T}{n_e P} \exp(\beta\Delta T) + \alpha_3 \frac{T}{n_e P}, \end{aligned} \quad (4.25)$$

where  $n_0 = P/k_B T$ ,

$$\alpha_2 = \frac{n_{\text{crit}}k_{VT}k_{ii}k_B}{\eta k_0 N^{2/3} k_{ev} k_{ad} \bar{n}_e \exp(-P_{VT}N^{2/3})}, \quad (4.26)$$

$$\alpha_3 = \frac{n_{\text{crit}}k_B}{\eta k_{ad}}, \quad (4.27)$$

From the Eqs. (4.22) and (4.23) we can deduce,

$$\frac{t_{\text{dif}} + t_{\text{charge}}}{t_{\text{dif}}} = 1 + \frac{2\sqrt{2}k_\tau k_B^2 \sqrt{T_e}}{3\sqrt{\pi}aL^2\sigma\sqrt{M}} \frac{T^{3/2}}{Pn_e} \quad (4.28)$$

$$= 1 + \alpha_4 \frac{T^{3/2}}{n_e P}, \quad (4.29)$$

with

$$\alpha_4 = \frac{2\sqrt{2}k_\tau k_B^2 \sqrt{T_e}}{3\sqrt{\pi}aL^2\sigma\sqrt{M}}. \quad (4.30)$$

In the expression of Eq. (4.24), substituting Eqs. (4.25) and (4.29) for  $n_{\text{crit}}/\Delta n_{\text{reac}}$  and  $(t_{\text{dif}} + t_{\text{charge}})/t_{\text{dif}}$ , the nucleation time is finally obtained as

$$t = \left[ \alpha_2 \frac{T}{n_e P} \exp(\beta \Delta T) + \alpha_3 \frac{T}{n_e P} \right] \left[ 1 + \alpha_4 \frac{T^{3/2}}{n_e P} \right]. \quad (4.31)$$

The nucleation times given by Eq. (4.31) were fitted to the experimental data for the RF powers from 6 to 20 W and for the temperature of 300 and 375 K and presented in Fig. 4.7. In the figure, the pressures is considered as a parameter, (a) 40, (b) 60 and (c) 80 Pa. When the fitting parameters were set to be  $\alpha_2 = 4 \times 10^{13}$ ,  $\alpha_3 = 4 \times 10^{13}$ ,  $\alpha_4 = 6 \times 10^{13}$ ,  $\beta = 0.015$ , and  $n_e = 9 \times 10^{13} P_{\text{RF}} + 5 \times 10^{11} P + 2 \times 10^{14}$ . The nucleation times derived analytically have good agreement with the data obtained experimentally. Although verification of the fitting parameters to be reasonable is complicated, it is significant that the nucleation time can explain phenomena of nucleation in the experiments at analytical level. With increasing RF power, electron density,  $n_e$  increases and  $[\text{C}_2\text{H}^-]$  produced by dissociative electron attachment also increases. The nucleation rate,  $\Delta n_{\text{reac}}$  is enhanced, and  $\tau_{\text{charge}}$  is reduced by increasing  $n_e$ . Therefore the nucleation time decreases with increasing discharge power, which possibly results in increasing concentration of nanoparticles in plasmas. Increasing pressure leads to increase the parent molecule of  $[\text{C}_2\text{H}_2]$  and  $[\text{C}_2\text{H}^-]$ . The  $\Delta n_{\text{reac}}$  increased by the molecule and negative ion, and the diffusion time  $\tau_{\text{dif}}$  proportional to the pressure in Eq. (4.22) reduce the nucleation time. With increasing temperature, the VT relaxation rate is enhanced, resulting in the slowing down of the reaction chain of Eq. (4.7). The  $\tau_{\text{dif}}$  is also reduced in Eq. (4.22). The nucleation time gets longer with the temperature and the concentration of nanoparticles spends a longer time to reach its critical value.

## 4.4 Conclusion

The nucleation times were measured with varying the discharge and parameters such as RF power, gas temperature and pressure in low-pressure  $\text{C}_2\text{H}_2/\text{Ar}$  plasmas by recording self-bias voltage. Dependencies of the nucleation times on these parameters were explained by using a kinetic model combined the vibration-transition energy relaxation mechanism and dynamics of nanoparticles in plasmas. It was significant that loss of nanoparticles was taken into account to derive the nucleation time defined by a period up to agglomeration phase. The nano-particles can be lost on the walls by diffusion if they are not charged. Once the nano-particles get negative charges, they are confined in the plasmas due to an electrostatic force at the sheath edge. The ratio of diffusion time and charging time determines a probability of the nanoparticles to be remaining in the plasma. The model involving the loss dynamics of the nanoparticles and the two fitting parameters succeeded in comprehension the dependence of the nucleation time on discharge power, gas temperature and pressure obtained experimentally.

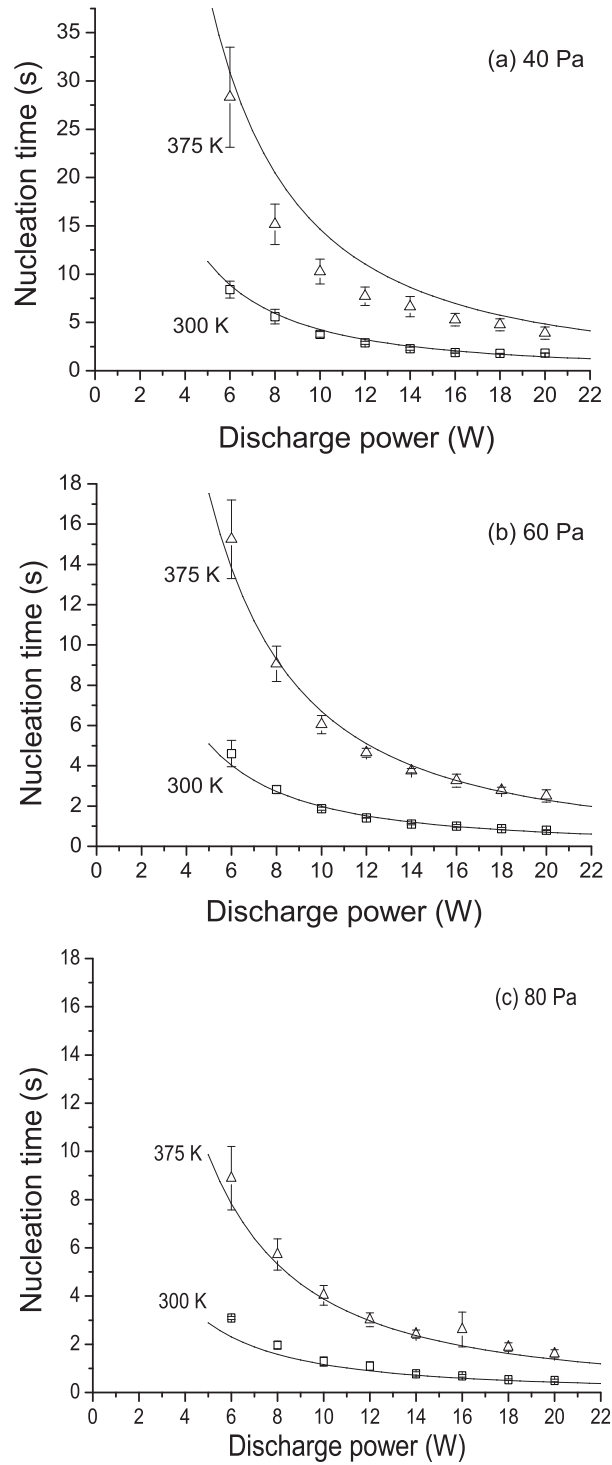


Figure 4.7: The nucleation times in the model given by Eq. (4.24) were fitted to the experimental data in the discharge power from 6 to 20 W for the temperature representative of 300 and 375 K as a parameter of the pressure of (a) 40, (b) 60 and (c) 80 Pa.

## 4.5 French summery

Dans ce chapitre sont présentés les résultats de l'étude de la formation des particules. Les expériences ont été effectuées dans un plasma RF généré dans un mélange gazeux composé de  $C_2H_2/Ar$  avec un ratio de flux bien défini. La formation des particules peut être déterminée par trois étapes: la nucléation, l'agglomération, et la croissance par dépôt en surface. Dans cette partie, nous avons focalisé notre attention sur l'étape de nucléation en étudiant les effets de la puissance RF, la pression et la température du gaz sur le temps de nucléation. L'évolution temporelle de la tension d'auto polarisation de la décharge est observée comme un indice pour détecter la fin de l'étape de nucléation. Les résultats montrent que le temps de nucléation augmente avec l'augmentation de la température mais diminue avec celle de la puissance et la pression. Cela dit, plus la température est basse, la puissance et la pression sont hautes, plus la nucléation est rapide. La dépendance de la nucléation sur la température est expliquée par le mécanisme de la relaxation de vibrationnelle-translationnelle des molécules  $C_2H_2$ . En effet l'excitation vibrationnelle joue le rôle d'énergie d'activation des réactions chimiques de ces molécules avec les clusters  $C_xH_y^-$ . Celle de la puissance et de la pression est expliquée par la concurrence entre le temps de charge et de diffusion. La nucléation est réalisée par une série de réaction en chaîne. Les petites particules doivent ensuite être chargées au moins une fois pour rester confinées dans le plasma, sinon elles diffusent et sont perdues. Le diagnostic du plasma montre que l'augmentation de la puissance augmente la densité électronique, et cela augmente la probabilité de charge. Dans l'autre côté, l'augmentation de pression réduit le parcours libre moyen, et par conséquent, aide à confiner les particules. Un calcul quantitatif, basé sur ces mécanismes, est effectué et les résultats obtenus sont en bon accord avec ceux déterminés expérimentalement.



# Bibliography

- [1] G. S. Selwyn, J. E. Heidenreich, and K. L. Haller, *Appl. Phys. Lett.* **57**, 1876 (1990).
- [2] S. J. Choi and M. J. Kushner, *J. Appl. Phys.* **74**, 853 (1993).
- [3] G. M. Jellum and D. B. Graves, *J. Appl. Phys.* **67**, 6490 (1990).
- [4] M. J. McCaughey and M. J. Kushner, *J. Appl. Phys.* **69**, 10 (1991).
- [5] M. Lennox and S. Coulombe, *J. Nanopart. Res.* **14**, 1245 (2012).
- [6] R. L. Merlino, *Plasma Physics Applied* (Research Signpost, Kerala, India, 2006) p. 73.
- [7] D. A. Mendis and M. Rosenberg, *Annu. Rev. Astron. Astrophys.* **32**, 419 (1994).
- [8] K. Takahashi and K. Tachibana, *J. Appl. Phys.* **89**, 893 (2001).
- [9] L. Boufendi and A. Bouchoule, *Plasma Sources Sci. Technol.* **3**, 262 (1994).
- [10] C. Courteille, Ch. Hollenstein, J. -L. Dorier, P. Gay, W. Schwarzenbach, A. A. Howling, E. Bertran, G. Viera, R. Martins, and A. Macario, *J. Appl. Phys.* **80**, 2069 (1996).
- [11] A. Bouchoule, A. Plain, L. Boufendi, J. Ph. Blondeau and C. Laur, *J. Appl. Phys.* **70**,1991 (1991).
- [12] A. A. Fridman, L. Boufendi, T. Hbid, B. V. Potapkin, and A. Bouchoule, *J. Appl. Phys.* **79**, 1303 (1996).
- [13] K. De Bleecker and A. Bogaerts, *Phys. Rev. E* **73**, 026405 (2006).
- [14] L. Boufendi, A. Bouchoule and T. Hbid, *J. Vac. Sci. Technol* **A14**, 572 (1996).
- [15] W. Long, *Chin. Phys. Soc.* **48** 1072 (1999).
- [16] J. Winter, J. Berndt, S. -H. Hong, E. Kovacevic, I. Stefanovic, and O. Stepanovic, *Plasma Sources Sci. Technol.* **18**, 034010 (2009).
- [17] Ch. Hollenstein, J. -K. Dorier, J. Datta, L. Sansonens, and A. A. Howling, *Plasma Sources Sci. Technol.* **3**, 278, (1994).
- [18] A. A. Howling, J. L. Dorier, and Ch. Hollenstein, *Appl. Phys. Lett.* **62**, 1341 (1993).
- [19] B. Agdur and B. Enander, *Appl. Phys.* **33**,575,(1962).

- [20] A. Bouchoule, "Dusty plasmas: Physics, Chemistry and Technological impacts in Plasma Processing" Wiley, New York. (1999).
- [21] L. Boufendi, J. Gaudin, S. Huet, G. Viera, and M. Dudemaine, *Appl. Phys. Lett.* **79**, 4301 (2001).
- [22] R. J. Wu and R. I. Miller, *J. Appl. Phys.* **67**, 1051 (1990).
- [23] M. Hundt, P. Sadler, I. Levchenko, M. Wolter, H. Kersten, and K. Ostrikov, *J. Appl. Phys.* **109**, 123305 (2011).
- [24] M. Cavarroc, M. Ch. Jouanny, K. Radouane, M. Mikikian and L. Boufendi, *J. Appl. Phys.* **99** 064301 (2006).
- [25] M. A. Lieberman, and A.J.Lichtenberg, "Principles of Plasma Discharges and Materials Processing", John Wiley and Sons, Hoboken, (2005)
- [26] M. Henault, Ph. D. thesis, University of Orleans, Orleans, 2015.
- [27] J. Winter and A. Leukens, *Proc. 14th Int. Symp. on Plasma Chemistry (Prague) (ISPC14)*,(1999).
- [28] L. Boufendi, M. Ch. Jouanny, E. Kovacevic, J. Berndt and M. Mikikian, *J. Phys. D: Appl. Phys.* **44**, 174035 (2011).
- [29] S. Hong, J. Berndt, and J. Winter, *Plasma Sources Sci. Technol.* **12**, 46 (2003).
- [30] A. Fridman, *Plasma Chemistry* (Cambridge Univ. Press, Cambridge, 2008) p. 978.
- [31] K. De Bleecker and A. Bogaerts, *J. Appl. Phys.* **88**, 151501 (2006).
- [32] A. V. Ivlev, M. Kretschmer, M. Zuzic, G. E. Morfill, H. Rothermel, H. M. Thomas, V. E. Fortov, V. I. Molotkov, A. P. Nefedov, A. M. Lipaev, O. F. Petrov, Yu. M. Baturin, A. I. Ivanov, and J. Goree, *Phys. Rev. Lett.* **90**, 5 (2003).
- [33] J. Goree, *Plasma Sources Sci. Technol.* **3**, 400 (1994).

# Chapter 5

## Pulse-time modulation

### 5.1 Introduction

Pulse-time modulation of RF power is to superimpose a rectangle wave to the RF fundamental signal in order to have an intermittent of plasma generation (Fig. 5.1). The rectangle wave consists of a period of zero voltage and that of non-zero. During the period of zero voltage (off-period), the RF power is not supplied to the plasma. The plasma is generated by the RF power in the period of non-zero voltage (on-period). The RF power of plasmas is thus turned on and shut off alternatively. It is reported that the plasma parameters are significantly affected by the pulse-time modulation.[2, 3] The frequency and duty cycle ratio of the rectangle wave can be regulated in order to obtain specified time of on-period and off-period.

After the RF power is turned off as the case of off-period, two phenomena occur in plasmas: relaxation of electron temperature and decay of plasma density.[4, 5]

During  $T_e$  relaxation, electrons lose their energy by collision with neutrals.[4, 5] Note  $\tilde{T}_e = T_e/T_n$  as dimensionless electron temperature where  $T_n$  is neutral molecular temperature. The time evolution of  $\tilde{T}_e$  is

$$\frac{d\tilde{T}_e}{dt} = -\frac{\tilde{T}_e - 1}{\tau_t}, \quad (5.1)$$

where  $1/\tau_t$  indicates time scale of  $T_e$  relaxation

$$\frac{1}{\tau_t} = 2\sqrt{\frac{m_e}{m_i}} \frac{v_{T_i}}{l_{en}} \sqrt{\tilde{T}_e}. \quad (5.2)$$

where  $v_{T_i} = \sqrt{8k_B T_i / (\pi m_i)}$  and  $l_{en}$  are thermal velocity of ions and mean free path of electron-neutral respectively.

Decay of plasma density is due to the lost of electrons and ions by recombination and diffusion from center of the plasma to walls. Since in low pressure cold plasmas the ionisation degree and the pressure are both low, the recombination effect is very weak. The diffusion effect is mainly taken into account. In early time, the space remain quasi-neutral with  $n_e = n_i = n_{i,e}$ . Note  $\tilde{n} = n_{i,e}/n_{\text{neutral}}$  as dimensionless plasma density, where  $n_{\text{neutral}}$  is density of neutral particles. The time evolution of  $\tilde{n}$  is

$$\frac{d\tilde{n}}{dt} = -\frac{\tilde{n}}{\tau_D}, \quad (5.3)$$

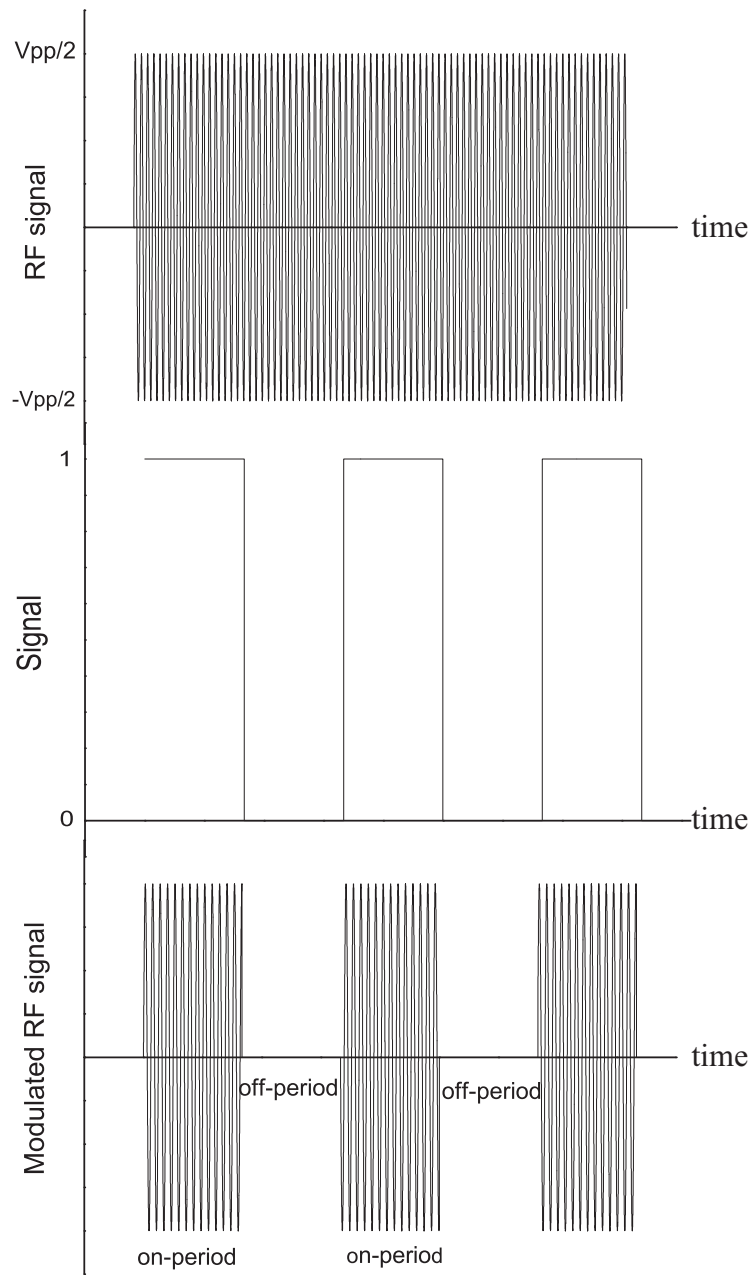


Figure 5.1: A pulse-time modulated RF signal. Superposing a rectangle wave to the RF fundamental signal, one can control to turn on/off a plasma.

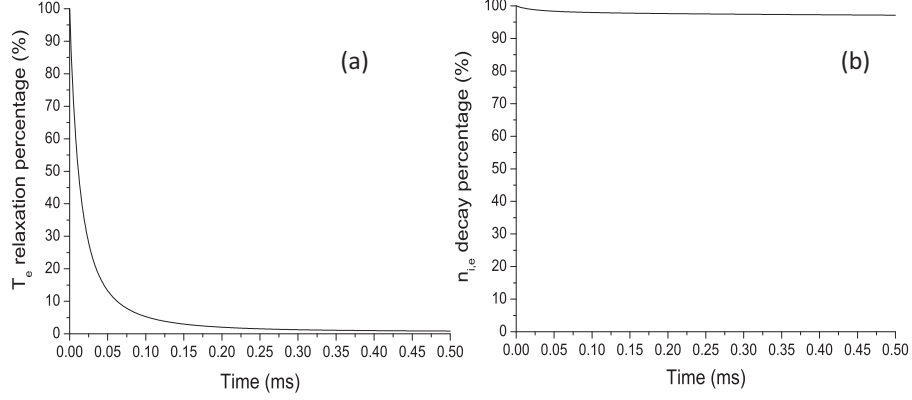


Figure 5.2: Simulation result of the time evolution of  $T_e$  relaxation (a), and plasma density decay (b).

where  $\tau_D$  is the time scale of plasma loss due to ambipolar diffusion. The time scale  $\tau_D$  is determined by the ambipolar coefficient  $D_a$  and a characteristic diffusion length  $\Lambda$  as

$$\tau_D^{-1} = \frac{D_a}{\Lambda^2} \simeq \frac{l_{in} v_{Ti}}{3\Lambda^2} (1 + \tilde{T}_e), \quad (5.4)$$

where  $l_{in}$  is mean free pass of ion-neutral. With the decay of plasma density, the debye length enlarge. When the ratio of the debye length to the diffusion length  $\lambda_{De}/\Lambda$  reach a critic value, the diffusion of electrons and ions has no longer ambipolar diffusion aspect but should treated separately as free diffusion.[5]

$$\frac{dn_e}{dt} = -\frac{\tilde{n}}{\tau_{De}}, \quad (5.5)$$

$$\frac{d\tilde{n}_i}{dt} = -\frac{\tilde{n}}{\tau_{Di}}, \quad (5.6)$$

The goal of pulse-time modulation is to modify plasma parameters. Electron temperature cool down during the off-period by the  $T_e$  relaxation, and the next on-period comes before the plasma completely decaying. The off-period is the key to reach this goal.

A numerical simulation and experimental measurements were preformed in order to fix the optimal modulation frequency.

## 5.2 Numerical simulation

As shown in Eqs. 5.2 and 5.4, both time scale of  $T_e$  relaxation  $\tau_t$  and decay plasma density  $\tau_D$  depend on  $\tilde{T}_e$ , and  $\tilde{T}_e$  varies as time. To exam the time evolution of the  $T_e$  relaxation and the decay of plasma density, a numerical simulation was performed. The simulation period was 0 ~ 0.5 ms with step of 1  $\mu$ s. Real scale of PK-3 plus chamber, hight  $H = 0.03$  m and radius  $R = 0.05$  m, was taken to calculate the characteristic diffusion length  $\Lambda$ . For cylindrical geometry,  $\Lambda$  could be estimated by[1]

$$\Lambda^{-2} \simeq \left(\frac{\pi}{H}\right)^2 + \left(\frac{2.4}{R}\right)^2. \quad (5.7)$$

A typical value of electron temperature  $T_e = 4$  eV for the PK-3 plus chamber was taken as the initial electron temperature. The neutral temperature was set at 300 K.

The simulation results are shown in Fig. 5.2. (a) and (b) of Fig. 5.2 show time evolution of  $T_e$  relaxation and  $n_{i,e}$  decay respectively. The effect of relaxation and decay are represent by the percentage of the on time value to the initial value. Electron temperature decreases monotonically with time as shown in Fig. 5.2 (a). Within  $0 \sim 0.05$  ms the electron temperature has a dramatically decreasing, it is cooled down to 10% of its attachments initial value at end of 0.05 ms. At end of 0.5 ms, that is less than 1%. In the case of plasma density decay as shown in Fig. 5.2 (b), the plasma density decrease with time but slowly within  $0 \sim 0.5$  ms. Only 3% of plasma density loss in this time interval. Such decreasing is not enough to enlarge the debye length to the critical value. The diffusion regime can still be considered as ambipolar diffusion, and the bulk of plasma is still quasi neutral in this time interval.

The time scale of the  $T_e$  relaxation is much smaller than that of the plasmas density decay. That gives the possibility to modify electron temperature while keeping plasma on by the time-pulse modulation. The off-period should be set within the interval that longer than the time scale of the  $T_e$  relaxation and shorter than that of the plasma density decay. The simulation results show that  $0.05 \sim 0.5$  ms is a favorable one. During the off-period, electron temperature has enough time to cool down, but the majority of electrons and ions remain in the bulk of plasmas. Electrons are reheat up by the next on-period to keep the plasma. One can consider that the plasma is turned on continually in whole period rather than to consider that the plasma is turned off in the off period and re-ignited by the next on-period.

### 5.3 Experiment

The effects of pulse-time modulation on electron temperature and ion density were studied in the PK-3 plus chamber. The pulse-time modulated signals were generated by the function generator by superimpose two channels. Argon gas was fed to the chamber and the flow was set to 400 SCCM. The pressure was maintained at 200 mtorr (26 Pa). The RF voltage (peak-to-peak) was set at 100 V. Modulation frequency and modulation duty cycle were parameters. The double-probe method was employed for the measurement of electron temperature and ion density. three experiments were preformed. 1) To fix the modulation duty cycle at 50% by varying the modulation frequency from 60 kHz to 1 kHz. The electron temperature and the ion density were evaluated. 2) To fix on-time period at 0.05 ms by varying the off-time period from 0.01 ms to 0.15 ms. The electron temperature was evaluated. 3) To fix off-time period at 0.05 ms by varying the on-time period from 0.01 ms to 0.15 ms. The electron temperature was evaluated. The electron temperature and the ion density were measured at 10 points along the centre axis of the chamber. Each measurement was repeated 3 times.

### 5.4 Results and discussion

Figure 5.3 shows the results of experiment 1). As the duty cycle was fixed at 50%, it equals to the off-period. The data at point 0 is the electron temperature without time-pulse modulation. (Fig. 5.3

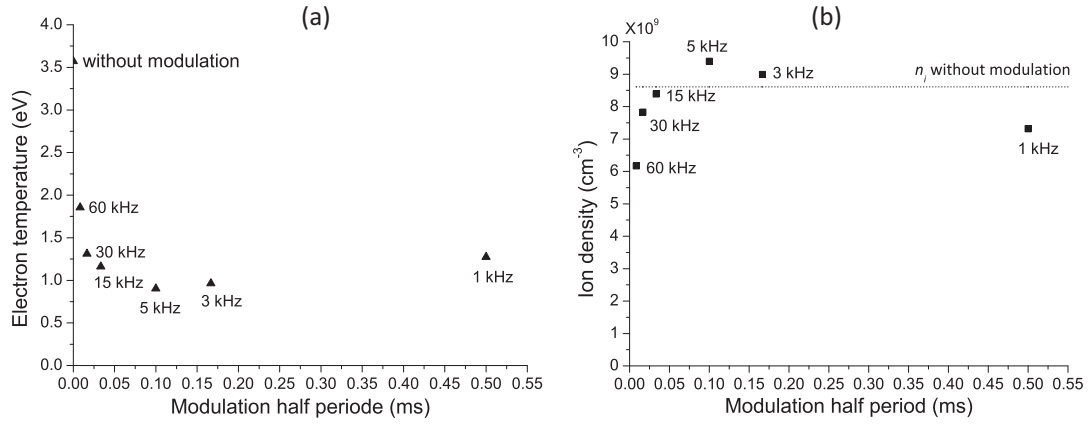


Figure 5.3: Measurement results of experiment 1). Evolution of  $T_e$  (a) and  $n_i$  (b). Axe X is half period of the modulation cycle.

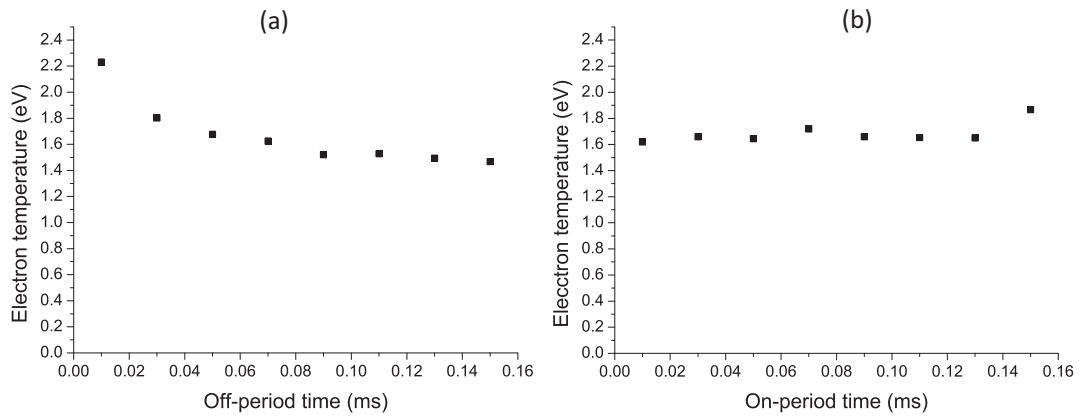


Figure 5.4: Measurement results of experiment 2) and 3). (a) Evolution of  $T_e$  with off-period while keeping on-period at 0.05 ms. (b) Evolution of  $T_e$  on-period while keeping off-period at 0.05 ms

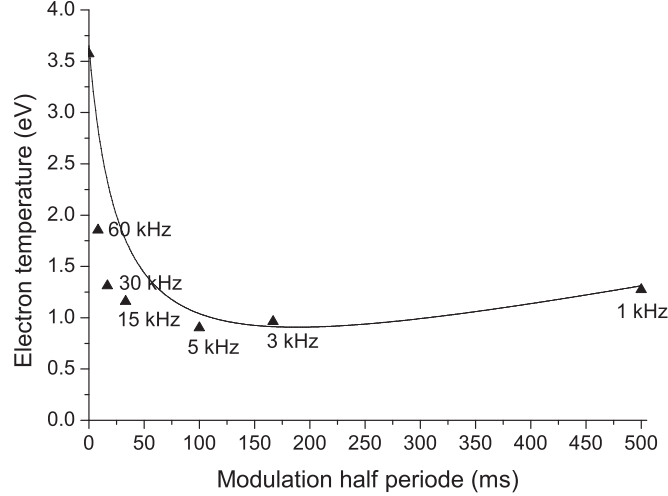


Figure 5.5: Fitting of evolution of  $T_e$  with half period while keeping duty cycle at 50%. Triangle symbols are experiment data, line is fitting curve.

(a)) Electron temperature decreased from 60 kHz to 5 kHz and increased from 5 kHz to 1 kHz. Ion density shows inverse evolution tendency to the electron temperature one. (Fig. 5.3 (b)) The ion density drops by applying the time-pulse modulation of 60 kHz in frequency compare to that without modulation and increase by changing the frequency from 60 kHz to 5 kHz, and then decrease from 5 kHz to 1 kHz. When the frequency is set at 5 kHz and 3 kHz, the ion densities are higher than that without modulation, *i.e.* the density enhancement occurs.

The measured electron temperature should be considered as the mean value of whole period cycle. As the duty cycle was fixed at 50% in experiment 1), decreasing of the frequency leads both of the increasing of the off-period and that of the on-period. The non monotonic evolution of electron temperature in experiment 1) could be supposed as the result of combined effect of the off-period and the on-period. Experiment 2) and 3) are to examine separately those two effects. Figure 5.4 (a) shows the result of the experiment 2), the off-period varies from 0.01 ms to 0.15 ms while the on-period remains at 0.05 ms. The electron temperature decreases monotonically. Furthermore, it shows that after around 0.05 ms the electron temperature decrease but more slowly than that from 0.01 ms to 0.05 ms. Figure 5.4 (b) shows the result of the experiment 3), the on-period varies from 0.01 ms to 0.15 ms while the off-period remains at 0.05 ms. The electron temperature practically do not change with the on-period from 0.01 ms to 0.13 ms and increases suddenly at end of 0.14 ms.

Three factors of pules-time modulation should be taken into account: off-period for the time of relaxation and decay, on-period for the time of power coupling and duty cycle for the percentage of mean RF power. Experiment 1) shows that the changing of electron temperature is not due to the duty cycle. Experiment 3) shows that within 0.01 ~ 0.13 ms both on-period and duty cycle do not affect on the electron temperature. By combining the experiment 2) and 3) to compare with the experiment 1), one can see that the decreasing of electron temperature from 60 kHz (half period 0.008 ms) to 5 kHz (half period 0.1 ms) is due to the increasing of the off-period, *i.e.*  $T_e$  relaxation time. The increasing

of electron temperature from 5 kHz to 1 kHz in experiment 1) corresponds to that of experiment 3) from 0.13 ms to 0.14 ms, due to the increasing of on-period. By taking into account of this aspect and calculate the mean value of electron temperature based on the  $T_e$  relaxation equation (Eq. 5.1), the results of experiment 1) can be fitted as shown in Fig. 5.5.

The decay of plasma density does not take significant influence within the time interval of the experiments, the changing of ion density measured in experiment 1) is not caused by the effect of the plasma density decay. For the condition of the experiments, ion density can be considered to be equal to electron density, thus the the notion of plasma density can be used. The evolution of the plasma density in experiment 1) can be assumed to be due to the changing of the electron temperature and the diminution of mean RF power by the pulse-time modulation. Comparer to the reference one, the mean RF power decreases to 50% due to the duty cycle. That is the cause of the diminution of ion density when applying the pulse-time modulation of 60 kHz in frequency. While the frequency varies from 60 kHz to 1 kHz, the percentage of RF power remain the same. When the electron temperature changes, the plasma density has to change inversely to compensate it, in order to keep the same coupled power. When the electron temperature become small enough as like for 5 kHz and 3 kHz, the plasma density can increase even higher than the reference one, that is the mechanism of the density enhancement by the pulse-time modulation.

## 5.5 Conclusion

Effects of the pulse-time modulation to the plasma parameters were investigated. The pulse-time modulation can be used as a method to modify the electron temperature. Three factors of the pulse-time modulation: off-period, on-period and duty cycle were studied for the PK-3 plus chamber. When off-period increase, the electron temperature decrease. The most significant decrease of the electron temperature occurs within the time interval  $0.01 \sim 0.1$  ms of the off-period. When on-period is shorter than 0.13 ms, it dose not influence to the electron temperature but when it increases to longer than 0.15 ms, the electron temperature increase with it. The percentage of coupled RF power has not influence to the electron temperature. To conclude the optimal modulation frequency is 10 kHz. The electron temperature can be regulated by regulating the duty cycle.

## 5.6 French summery

Le rôle de la modulation temporelle de l'impulsion de la puissance RF est étudiée dans ce chapitre. En superposant un signal rectangulaire au signal RF, ce dernier peut être ainsi allumé et coupé par les impulsions. La modulation a pour effet de baisser la température électronique. L'effet est examiné en jouant sur la durée du plasma allumé et celle où le plasma est éteint ainsi que le rapport cyclique. La diminution de la température électronique est due à la relaxation pendant la phase plasma éteint. Pour réguler la température électronique, la durée de zéro voltage doit être assez long pour que les électron aient le temps de se relaxer tout en assurant que le plasma ne disparaisse pas. Il est trouvé entre 0.01 et 0.1 ms la diminution de la température électronique est plus important. Une fois la durée

de la phase plasma éteint fixée, le changement de celle de la phase plasma allumé n'influence pas la température électronique.

# Bibliography

- [1] J. Goree, Plasma Sources Sci. Technol. **3**, 400, (1994).
- [2] H. Sugai, K. Nakamura, Y. Hikosaka, and M. Nakamura, J. Vac. Sci. Technol. **A13**, 887 (1995).
- [3] S. Samukawa, H. Ohtake and T. Mieno, J. Vac. Sci. Technol. **A14**, 3049 (1996).
- [4] L. Couëdel, A. A. Samarin, M. Mikikian, and L. Boufendi, Phys. of Plasmas **15**, 063705, (2008).
- [5] A. V. Ivlev, M. Kretschmer, M. Zuzic, G. E. Morfill, H. Rothermel, H. M. Thomas, V. E. Fortov, V. I. Molotkov, A. P. Nefedov, A. M. Lipaev, O. F. Petrov, Yu. M. Baturin, A. I. Ivanov, and J. Goree, Phys. Rev. Lett. **90**, 5 (2003).



# Chapter 6

## Analysis methods

### 6.1 Introduction

Based on the theoretical aspect described in Chapter 2, a calculation method can be developed to analyze plasma parameters and forces acting on particle for each real experiment condition in the PK-3 plus chamber. In the calculation, the bulk and sheath of plasmas are dealt separately, and then boundary conditions are discussed in order to combine the two parts. Finally, the transport behaviours of particles in whole space of chamber could be analysed.

In the bulk of plasmas, ambipolar diffusion is considered as the dominant phenomenon.[4] A fluid model is taken, and a numerical solution is discussed in order to calculate the spacial distribution of ion density.[18, 19] Ion flow and electric field can be deduced by the ambipolar diffusion theory.[1, 24, 3]

For the sheath of plasmas, Child-Langmuir model is taken.[1, 24, 3, 23] The potential  $V(z)$ , electric field  $E(z)$  and ion density  $n_i(z)$  in function of distance from the walls can be deduced analytically. The boundary conditions is discussed between the Child-Langmuir sheath and ambipolar diffusion regime, and the sheath length can be determined.[1, 24, 3]

Particle charge in the bulk and sheath of plasmas have different aspect. The difference is mainly due to the different structure of the sheath around the small dust particle and macroscopic chamber walls.[1, 24, 3] In the bulk of plasmas, the presence of dust particle can be considered as a small potential perturbation, whose influence distance can be characterised by the debye length  $\lambda_{DL}$ . In the sheath of plasmas, electron depletion around particle should be taken into account.[8, 9, 10]

### 6.2 Numerical solution of fluid model

A fluid model was applied to calculate spatial distributions of ion density in plasmas.[4, 18, 19] In the plasmas, electrons and ions diffuse from the ionization centre to the walls. Electrons are much faster than ions in diffusion. Centres of negative and positive charges separated a bit lead to an electric field. Electrons get slowed down and ions are accelerated by this electric field. Finally, ions and electrons diffuse together by so-called ambipolar diffusion. Loss of electron-ion pairs on the walls is compensated by ionization. In our case, the electron-ion recombination can be neglected.[1, 24, 3, 4, 18, 19]

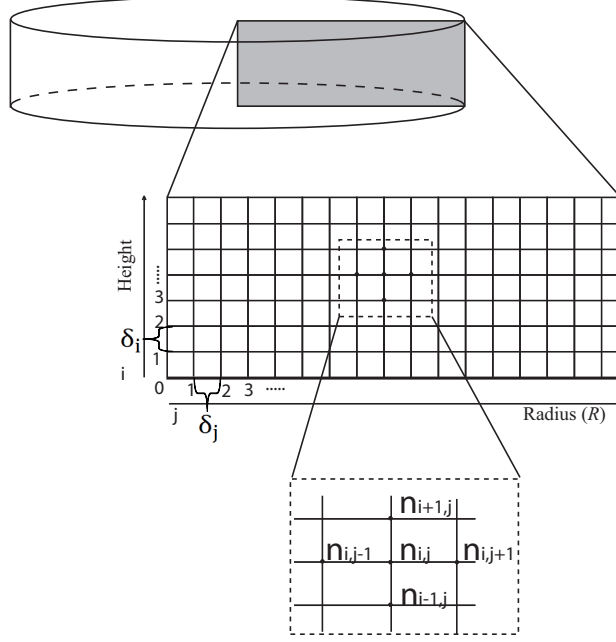


Figure 6.1: Lattice for numerical solution. Half of cross section of the chamber is the numerical treatment area.

The ions and electrons follow can be calculated by the ambipolar diffusion and continuity equation[4, 8, 11, 12]

$$\begin{cases} \mathbf{\Gamma} = -D_a \nabla n, \\ -\nabla \cdot \mathbf{\Gamma} + \nu_{iz} n = 0. \end{cases} \quad (6.1)$$

In the equations,  $\mathbf{\Gamma}$ ,  $D_a$ ,  $n$ ,  $\nu_{iz}$  are flux, ambipolar diffusion coefficient, electron/ion density and ionization rate, respectively. These two equations give

$$D_a(\Delta n) + \nu_{iz} n = 0. \quad (6.2)$$

In a cylindrical coordinate system  $(r, \theta, z)$  with  $\theta$ -symmetry one has,

$$\Delta n = \frac{1}{r} \frac{\delta n}{\delta r} + \frac{\delta^2 n}{\delta r^2} + \frac{\delta^2 n}{\delta z^2}, \quad (6.3)$$

where  $r$  and  $z$  are radial distance and height, respectively. A half area of cross-section of the reactor is taken into account (Fig. 6.1). The area is divided into elements by a grid of the radius ( $r$ ) and height ( $z$ ) axes with intervals. Indexes of the radius and height directions are noted by  $j$  and  $i$ , respectively. The intervals in these directions are represented by  $\delta_j$  and  $\delta_i$ , respectively. For each element of  $n_{i,j}$  corresponding to the density on a lattice point on the grid,

$$\begin{cases} \frac{\partial n_{i,j}}{\partial r} = \frac{n_{i,j+1} - n_{i,j-1}}{2\delta_j}, \\ \frac{\partial^2 n_{i,j}}{\partial r^2} = \frac{n_{i,j+1} + n_{i,j-1} - 2n_{i,j}}{\delta_j^2}, \\ \frac{\partial^2 n_{i,j}}{\partial z^2} = \frac{n_{i+1,j} + n_{i-1,j} - 2n_{i,j}}{\delta_i^2}, \\ r = j\delta_j. \end{cases} \quad (6.4)$$

We can find an equation

$$(2\frac{\nu_{iz}}{D_a}j\delta_j^2\delta_i^2 - 2j\delta_i^2 - 2j\delta_j^2)n_{i,j} + (2j-1)\delta_i^2n_{i,j-1} + (2j+1)\delta_i^2n_{i,j+1} + 2j\delta_j^2n_{i-1,j} + 2j\delta_j^2n_{i+1,j} = 0. \quad (6.5)$$

The ratio of ionization rate to ambipolar diffusion coefficient,  $\frac{\nu_{iz}}{D_a}$  is treated as a fitting parameter. In the capacitively coupled plasmas, the ionization rate is not homogenous. Depending on configuration of electrodes and discharge condition, there is an area where the ionization rate is much higher than other parts. In this calculation, the highly ionization area is defined which generates the ions and electrons dominated by the ionization and diffusion. The area is connected to the sheath facing wall through a diffusion area dominated by the diffusion only. (Fig.??) The total flux of ions at the ionization boundary is equal to that at a plasma-sheath boundary, i.e.  $\Gamma_{iz}A_{iz} = \Gamma_s A_s$ , where  $\Gamma_{iz}$ ,  $\Gamma_s$ ,  $A_{iz}$ ,  $A_s$  are ion flux at ionization area, that at plasma sheath, surface of ionisation area and that around the sheath, respectively. A relationship of the ion flux at the plasma sheath boundary and that at the ionization boundary can be expressed by a factor of dimension of area at the boundaries. The condition at the plasma sheath boundary is determined by the Bohm criterion,  $v_B = \sqrt{eT_e/m_i}$ , where  $v_B$ ,  $e$ ,  $T_e$ ,  $m_i$  are the Bohm speed for ions, elementary charge, electron temperature, and mass of ion, respectively. The ion density at the boundary is given as  $n_s = \Gamma_s/v_B$ .

The calculation area is dispersed by  $N_j$  and  $N_i$  grid points in radial and height direction, respectively. In total, there are  $N = N_i N_j$  gride points. For each gride points, one equation can be established as shows Eq. (6.5). If the density in each gride point is treated as unknown, one can establish  $N$  equations for  $N$  unknowns. Note the density at 1st row 1st column  $n_{1,1}$  as the 1st unknown  $x_1$ , the density at 1st row, 2nd column  $n_{1,2}$  as the 2nd unknown  $x_2$ , then the density  $n_{i,j}$  as unknown  $x_I$ , where  $I = I = iN_j + j$ . Equation (6.5) for all  $N$  unknowns can be written as

$$\left\{ \begin{array}{l} a_{1,1}x_1 + a_{1,2}x_2 \dots a_{1,N}x_N = b_1 \\ a_{2,1}x_1 + a_{2,2}x_2 \dots a_{2,N}x_N = b_2 \\ \vdots \quad \dots \quad \vdots \\ a_{I,1}x_1 + a_{I,2}x_2 \dots a_{I,N}x_N = b_I \\ \vdots \quad \dots \quad \vdots \\ a_{N,1}x_1 + a_{N,2}x_2 \dots a_{N,N}x_N = b_N \end{array} \right. \quad (6.6)$$

$a_{1,1} \dots a_{N,N}$  are equation coefficients. Once all coefficients are attributed a value, the equations can be resolved. For each element  $I = iN_j + j$  in the bulk of the plasma, by substituting Eq. (6.5) in to the  $I^{th}$  equation of Eq. (6.6), one have

$$\left\{ \begin{array}{l} a_{I,I} = (2\frac{\nu_{iz}}{D_a}j\delta_j^2\delta_i^2 - 2j\delta_i^2 - 2j\delta_j^2), \\ a_{I,I+1} = (2j+1)\delta_i^2, \\ a_{I,I-1} = (2j+1)\delta_i^2, \\ a_{I,I+N_j} = 2j\delta_j^2, \\ a_{I,I-N_j} = 2j\delta_j^2, \\ a_{I,others} = 0, \\ b_I = 0. \end{array} \right. \quad (6.7)$$

For the element  $I$  at the boundary, the equation coefficients are

$$\begin{cases} a_{I,I} = 1, \\ a_{I,others} = 0, \\ b_I = n_{\text{boundary}}. \end{cases} \quad (6.8)$$

Once the coefficients are set, unknowns can be resolved. Thus, spatial distribution of ion density  $n_i(r, z)$  in the bulk of the plasmas can be obtained.

In the calculation mentioned above, coefficients were taken from literatures.[9, 4] Ionisation area is a fitting parameter. In order to determine the spatial distribution of ion density  $n_i(r, z)$  for a given discharge condition, the calculation result should fit to the measured one dimensional data. This calculation method could be use to determine three dimensional spatial distribution of ion density from measured one dimensional data.

Figure 6.2 shows an example of the calculation result of the spatial distribution of ion density  $n_i(r, z)$ . Figures 6.2 (a) and (b) give the calculated  $n_i(r, z)$  for the discharge 100 mtorr (13 Pa) and 500 mtorr (66 Pa), respectively in pressure, 100 V in RF voltage. Several points on the centre axe of the chamber ( $r = 0$ ) could be measured by double-probe as shown in Fig. 6.3. The cross markers represent the experimentally measured data of ion density. The lines are the calculated results extracted from Fig. 6.2 at  $r = 0$ . One can see that under different gas pressure condition, the peak positions of ion density are different. The peak appears almost in the centre for the case 100 mtorr, and near the powered electrode for the case 500 mtorr. This is caused by the different ionisation area. In the calculation, the ionisation area is regulated in the way for the calculation results to fit to the measured data. According to the fitting result, the ionisation area is  $X \in [-15, 15], Y \in [6, 16]$  mm for the case 100 mtorr, and  $X \in [-15, 15], Y \in [1, 6]$  mm for the case 500 mtorr. Once the spatial distribution of ion density  $n_i(r, z)$  is determined, ambipolar flux can be deduced as shown in Fig. 6.4. The colour and arrows represent ion density and ambipolar flow, respectively.

### 6.3 Boundary condition at sheath edge and sheath structure

The sheath structure can be analytically resolved by using Child-Langmuir law.[1, 24, 3, 23]

$$\frac{\partial^2 V(z)}{\partial z^2} = -\frac{en_i(z)}{\epsilon_0}. \quad (6.9)$$

By taking into account our experimental conditions, mean free path of ions can be estimated around 0.1 mm which is smaller than the estimated sheath width. Collision sheath model should be taken, and ion mean speed in the sheath can be expressed as

$$\begin{aligned} u_i(z) &= \mu_i E(z) \\ &= -\mu_i \frac{\partial V(z)}{\partial z}, \end{aligned} \quad (6.10)$$

where  $\mu_i$  and  $E(z)$  are ion mobility and electric field, respectively. Since there is neither ion source nor drain in the sheath, ion current should remain constant,

$$J_i = en_i(z)u_i(z) = \text{constant}. \quad (6.11)$$

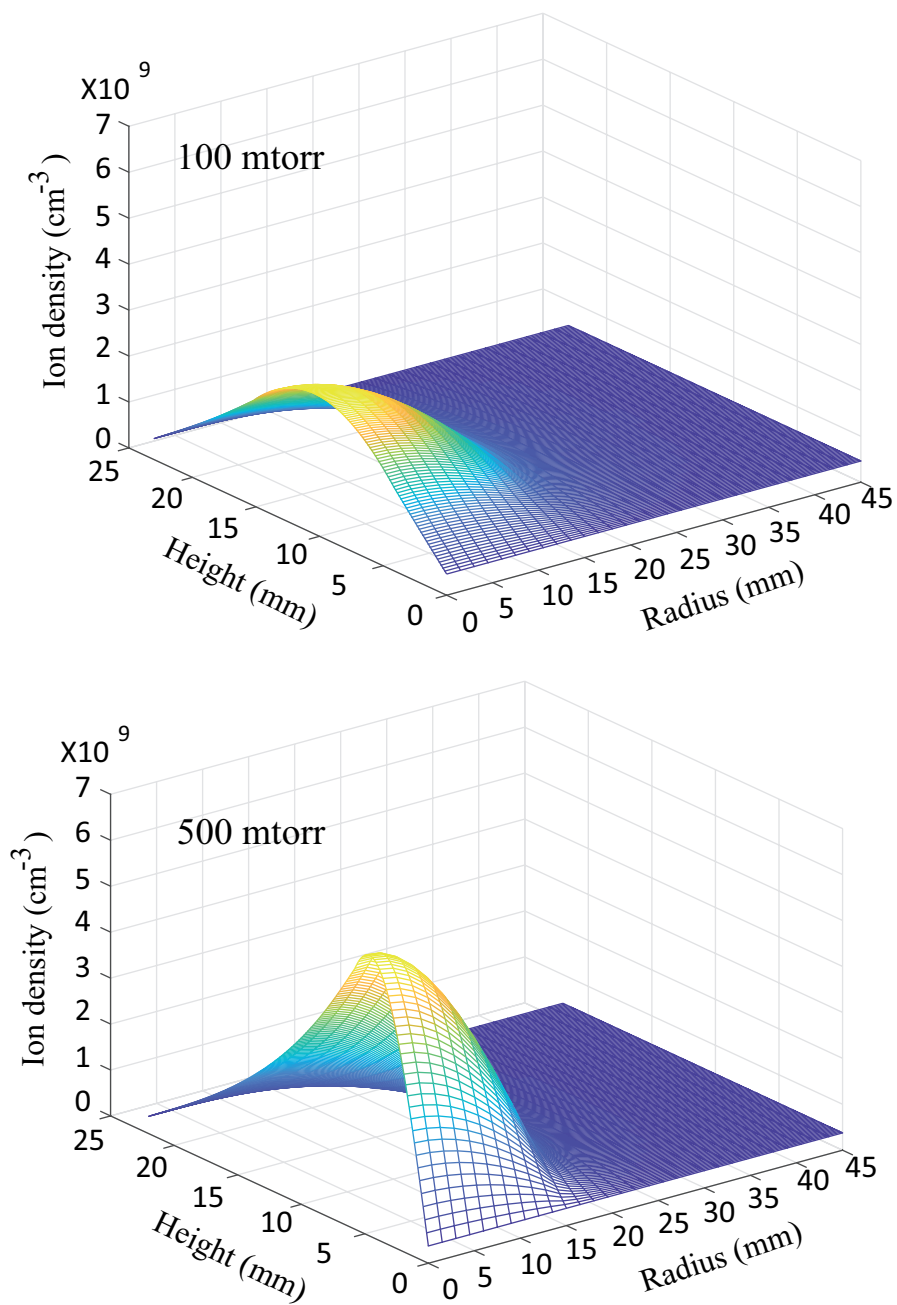


Figure 6.2: Calculation results of spatial distribution of ion density under conditions 100 and 500 mtorr in gas pressure, 100 V in RF voltage.

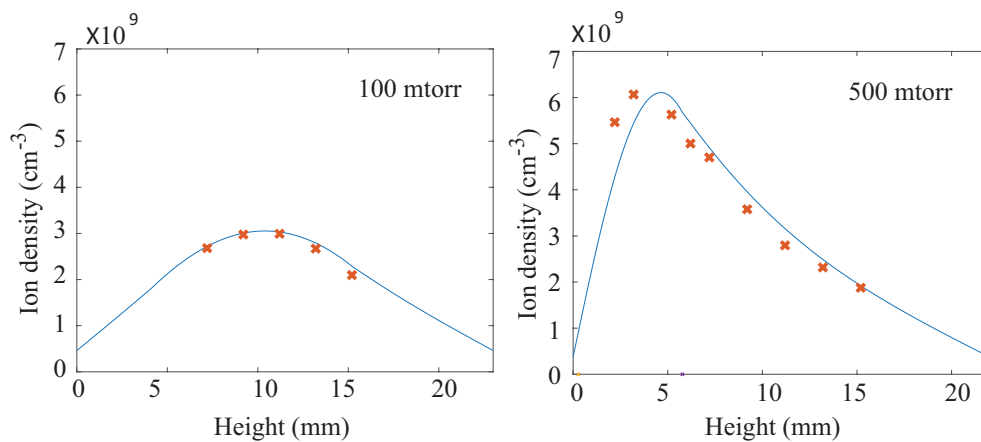


Figure 6.3: Calculated ion densities fit to the measurement data. Cross markers represent measured data, line represents calculated results.

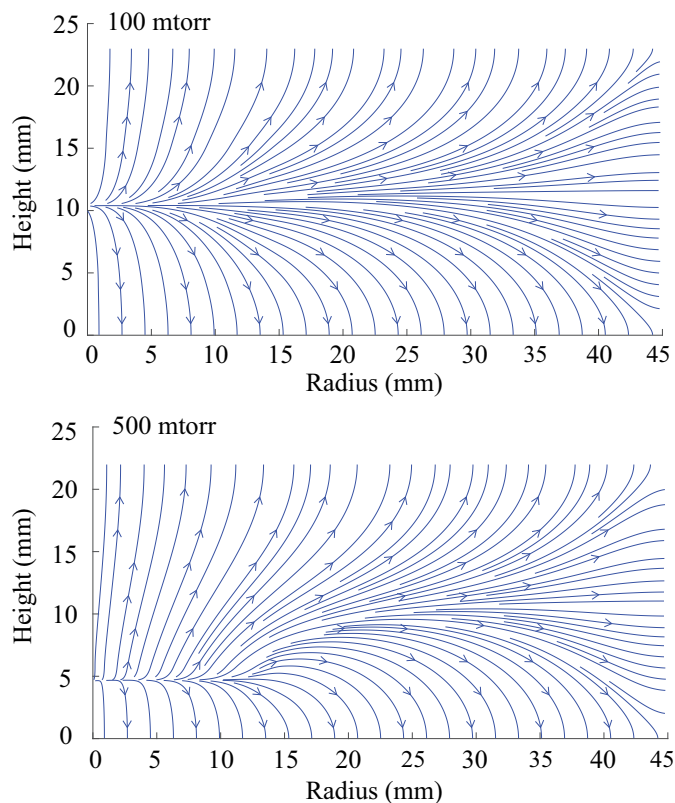


Figure 6.4: Ion flow direction calculated by using ambipolar diffusion model for the case of 100 and 500 mtorr in gas pressure, based on the spatial distribution of ion densities.

According to the Bohm criterion to form an ion sheath, ions have a mean velocity of  $u_B = \sqrt{(k_B T_e / m_i)}$  at the sheath edge.[1] This requires that the ion density at the sheath edge  $n_i(s) = \exp(-1/2)n_0 \approx 0.6n_0$ , where  $n_0$  is the ion density in the plasma bulk. The ion current is

$$J_i = 0.6en_0\sqrt{(k_B T_e / m_i)}. \quad (6.12)$$

By combining Eqs. (6.9), (6.10) and (6.12),  $V(z)$ ,  $E(z)$  and  $n_i(z)$  can be solved as:

$$V(z) = -\sqrt{\frac{8J_i}{9\epsilon_0\mu_i}}(D-z)^{\frac{3}{2}}, \quad (6.13)$$

$$E(z) = -\frac{\partial V(z)}{\partial z} = \sqrt{\frac{2J_i}{\epsilon_0\mu_i}}(D-z)^{\frac{1}{2}} \quad (6.14)$$

and

$$n_i(z) = \frac{\epsilon_0}{e} \frac{\partial E(z)}{\partial z} = \frac{\epsilon_0}{2e} \sqrt{\frac{2J_i}{\epsilon_0\mu_i}}(D-z)^{-\frac{1}{2}}. \quad (6.15)$$

Here,  $D$  is a constant when one choose the wall as  $z = 0$ . We determine the constant  $D$  and a sheath edge noted as  $S$ . Note that the constant  $D$  is not the sheath edge, since the ion density  $n_i(D)$  goes to infinity in Eq. (7.13). The sheath edge  $S$  should be located between  $z = 0$  and  $z = D$ . The Eqs. (7.11), (7.12) and (7.13) are available in an interval  $z \in [0, S)$ . The interval  $z > S$  corresponds to the pre-sheath region, where ions are accelerated to the Bohm speed by the local electric field from ambipolar diffusion [13]. The ambipolar diffusion give an ion current,

$$J_i(z) = en_i(z)u_i(z) = -eD_a \frac{\partial n_i}{\partial z}, \quad (6.16)$$

where  $D_a$  is ambipolar diffusion coefficient. Taking an approximation as  $D_a \approx \mu_i \frac{k_B T_e}{e}$ , the local electric field can be expressed as

$$E = -\frac{k_B T_e}{e} \frac{1}{n_i} \frac{\partial n_i}{\partial z}. \quad (6.17)$$

At the sheath edge, continuity condition of the electron field requires that

$$\lim_{z \rightarrow S^-} E(z) = \lim_{z \rightarrow S^+} E(z), \quad (6.18)$$

therefore

$$\sqrt{\frac{2J_i}{\epsilon_0\mu_i}}(D-S)^{\frac{1}{2}} = -\frac{k_B T_e}{e} \frac{1}{n_i(S)} \frac{\partial n_i}{\partial z} \Big|_{z=S}. \quad (6.19)$$

Taking the Bohm criterion and the ambipolar diffusion (Eq. (6.16)) into account, the continuity condition is given by

$$\sqrt{\frac{2J_i}{\epsilon_0\mu_i}}(D-S)^{\frac{1}{2}} = \frac{k_B T_e}{eD_a} u_B. \quad (6.20)$$

Therefore,

$$D-S = \left(\frac{k_B T_e u_B}{eD_a}\right)^2 \frac{\epsilon_0\mu_i}{2J_i} \approx \frac{\epsilon_0 u_B^2}{2J_i\mu_i}. \quad (6.21)$$

At a steady state in the plasma, time averaged ion and electron currents toward the walls

$$J_i = en_i(S)u_B, \quad (6.22)$$

and

$$J_e = en_e(S) \sqrt{\frac{k_B T_e}{2\pi m_e}} \exp\left[-\frac{e(V_{\text{wall}} - V_p(S))}{k_B T_e}\right], \quad (6.23)$$

have to be equal, where  $m_e$ ,  $V_{\text{wall}}$  and  $V_p(S)$  are electron mass, potential at the wall and plasma potential at the sheath edge. Therefore,

$$en_i(S)u_B = en_e(S) \sqrt{\frac{k_B T_e}{2\pi m_e}} \exp\left[-\frac{e(V_{\text{wall}} - V_p(S))}{k_B T_e}\right]. \quad (6.24)$$

At the sheath edge, the neutral condition  $n_i(S) = n_e(S)$  gives

$$V_{\text{wall}} - V_p(S) = -\frac{1}{2} \ln\left(\frac{m_i}{2\pi m_e}\right) \frac{k_B T_e}{e}. \quad (6.25)$$

Substituting  $V_{\text{wall}}$  and  $V_p(S)$  by the potentials of  $V(0)$  and  $V(S)$  obtained in the Child-Langmuir law (Eq. (7.11)). Then Eq. (6.25) is

$$-\sqrt{\frac{8J_i}{9\epsilon_0\mu_i}} D^{\frac{3}{2}} + \sqrt{\frac{8J_i}{9\epsilon_0\mu_i}} (D - S)^{\frac{3}{2}} = -\frac{1}{2} \ln\left(\frac{m_i}{2\pi m_e}\right) \frac{k_B T_e}{e}, \quad (6.26)$$

and derives

$$D = \left(\frac{eu_B^2}{2J_i\mu_i}\right)^{\frac{2}{3}} + \frac{1}{2} \ln\left(\frac{m_i}{2\pi m_e}\right) \left(\frac{8J_i}{9\epsilon_0\mu_i}\right)^{-\frac{1}{2}} \frac{k_B T_e}{e}^{\frac{2}{3}}. \quad (6.27)$$

The sheath edge is given as  $S = D - \frac{eu_B^2}{2J_i\mu_i}$ . Once the coefficient  $D$  and sheath edge  $S$  are determined, the potential, electric field and ion density in the plasma sheath can be calculated from electron temperature and ion density of the plasma bulk measured in the experiments. Figure 6.5 shows the profiles of the electric field  $E(z)$  and ion density  $n_i(z)$  calculated as examples. The solid curve is a solution of Child-Langmuir law, which is available for  $z < S$ . The  $z = S$  is considered as the sheath edge, where ions attain the Bohm speed. The region  $z < S$  is the sheath, where electron depletion occurs, and the region  $z > S$  is considered to have a quasi neutral condition. For  $z > S$ , the Child-Langmuir law being not available any longer, one should take the dotted curve which is the solution of ambipolar diffusion.

## 6.4 Particle charge in the bulk of plasma and in the sheath

### 6.4.1 Particle charge in the bulk of plasma

In the plasma bulk, one can consider a particle having a floating potential  $V_f$ , and the plasma potential is  $V_p$ . Ion thermal speed is much higher than ion drift speed. Then electrons and ions flows toward the particle can be expressed by the OML model as

$$\Gamma_e = \pi r_p^2 n_e \left[\frac{8k_B T_e}{\pi m_e}\right]^{\frac{1}{2}} \exp\left[\frac{e(V_f - V_p)}{k_B T_e}\right] \quad (6.28)$$

and

$$\Gamma_i = \pi r_p^2 n_i \left[\frac{8k_B T_i}{\pi m_i}\right]^{\frac{1}{2}} \left[1 - \frac{e(V_f - V_p)}{k_B T_i}\right], \quad (6.29)$$

respectively, where  $r_p$ ,  $n_e$ ,  $n_i$ ,  $k_B$ ,  $T_e$ ,  $T_i$ ,  $m_e$ ,  $m_i$ ,  $e$  are particle radius, electron density, ion density, Boltzmann constant, electron temperature, ion temperature, electron mass, ion mass and elementary charge,

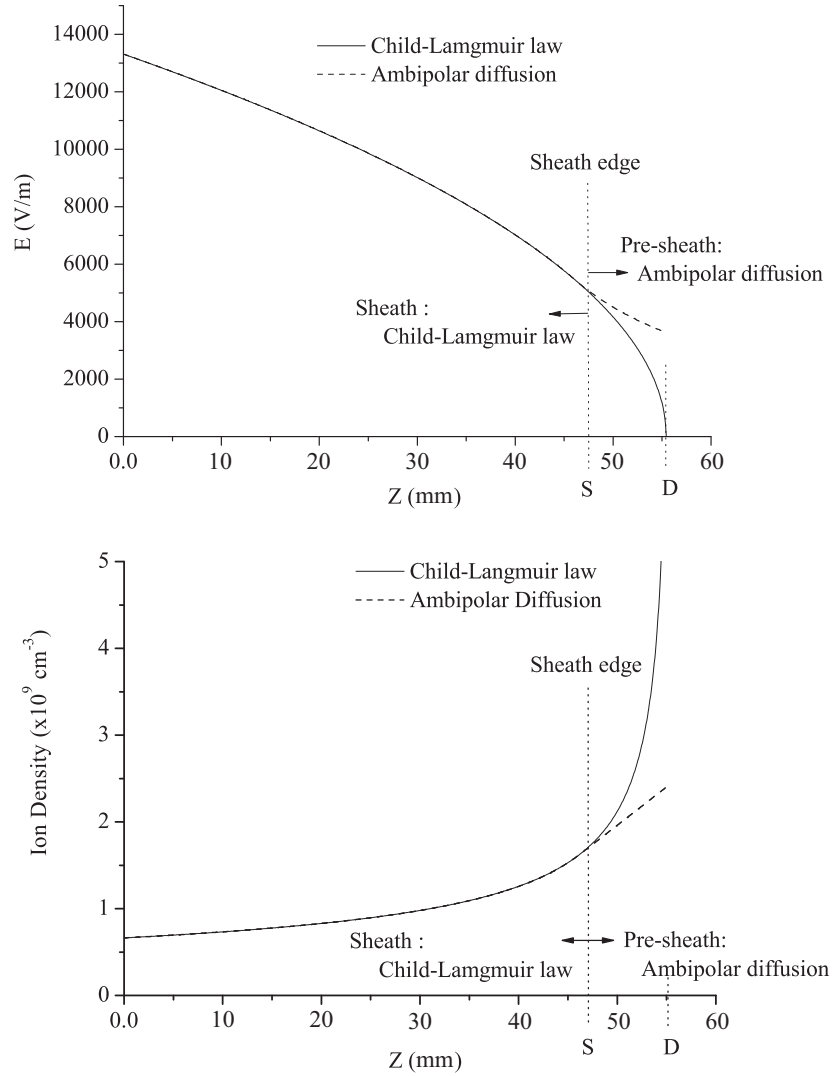


Figure 6.5: Electric field and ion density in sheath and pre-sheath calculated with the Child-Langmuir law (solid curve) and ambipolar diffusion (dotted curve). The  $S$  means sheath edge. In the interval  $z < S$ , one should take the solid curve. In the  $z > S$ , the dotted curve is taken.

respectively. A steady state requires that electron flow equals to ion flow. Thus from the equation  $\Gamma_e(V_f - V_p) = \Gamma_i(V_f - V_p)$ , the potential difference between particle and plasma bulk  $V_f - V_p$  can be determined, and particle charge can be expressed as

$$Q = (V_p - V_s)4\pi\epsilon_0 r_p \left(1 + \frac{r_p}{\lambda_{DL}}\right), \quad (6.30)$$

where  $\lambda_{DL}$  and  $\epsilon_0$  are linearized Debye length and vacuum permittivity.[14]

$$\lambda_{DL} = \frac{\lambda_{De}\lambda_{Di}}{\sqrt{\lambda_{De}^2 + \lambda_{Di}^2}}, \quad (6.31)$$

where  $\lambda_{De}$  and  $\lambda_{Di}$  are electron and ion Debye length respectively.[15]

### 6.4.2 Particle charge in the sheath

In the case of particles getting charge in the sheath, electron depletion and high ion drift speed toward the wall should be taken into account.[23, 8] Considering the potential of particle,  $V_p$ , the plasma potential, the plasma density and the electron temperature at the edge of pre-sheath are denoted  $V_s$ ,  $n_0$  and  $T_e$ , respectively. Ion density, ion drift velocity and space potential at the local in the sheath are as  $n_i(z)$ ,  $u_i(z)$  and  $V(z)$ , respectively. The electron and ion flows can be expressed by

$$\Gamma_e = \pi r_p^2 n_e \left[\frac{8k_B T_e}{\pi m_e}\right]^{\frac{1}{2}} \exp\left[\frac{e(V_f - V(z) + V(z) - V_p)}{k_B T_e}\right] \quad (6.32)$$

and

$$\Gamma_i = \pi r_p^2 n_i(z) u_i(z) \left[1 - \frac{e(V_f - V(z))}{\frac{1}{2} m_i u_i^2}\right], \quad (6.33)$$

respectively. The particle charge should take the simple capacitor model due to the electron depletion,

$$Q = (V_f - V_p)4\pi\epsilon_0 r_p. \quad (6.34)$$

In order to calculate the particle charge in the sheath, the ambient potential profile  $V(z)$  and the ion density distribution  $n_i(z)$  through the sheath are necessary.

## 6.5 Conclusion

The methods to calculate the spatial distribution of ion density, the sheath structure and particle charge are discussed in this chapter. Those methods are used in the next chapter in order to analyze quantitatively the transport behaviours of dust particle in the RF complex plasmas. The main work of this chapter is to adapt the calculation theory to our experiment setup, and combine the bulk of plasma and the plasma sheath in the calculation. Ion flux, electric field, particle charges can be calculated through whole space. The transport of dust particle from the bulk of plasmas to the sheath can be resolved numerically.

## 6.6 French summery

Les méthodes de calculs numériques sur l'analyse du plasma et des forces s'exerçant sur les particules dans le plasma sont discutées dans ce chapitre. Les modèles théoriques de base sont décrits dans le chapitre 2. Les travaux présentés dans ce chapitre concernent l'adaptation des modèles à la configuration réelle de nos expériences et d'en déduit des solutions numériques. La méthode de calculer numériquement la distribution spatiale de la densité plasma en 2 dimensions à partir des mesures par sonde Langmuir est basée sur le modèle de la diffusion ambipolaire. Les flux ambipolaires peuvent ainsi être calculés. La structure de la gaine plasma est décrite par la loi Child-Langmuir en discutant les conditions aux limites entre la gaine et le corps du plasma. Les charges des particules obtenues dans le corps plasma et dans la gaine sont de différentes. Basées sur les structures calculées de la gaine et le corps plasma, les charges des particules peuvent être résolues numériquement à travers du corps plasma et la gaine. Les méthodes présentées dans ce chapitre sont aussi utilisées dans le chapitre suivant pour l'analyse des comportement des particules dans le plasma.



# Bibliography

- [1] P. Chabert and N. Braithwaite, *Physics of Radio-Frequency Plasmas* (Cambridge Univ. Press, Cambridge, 2011).
- [2] M. A. Liberman, A. J. Lichtenberg, *Principles of plasma discharges and materials processing*, (Wiley-Interscience Publication, 1994).
- [3] A. Bouchoule, *Dusty plasmas Physics, Chemistry and Technological Impacts in Plasma Processing*, (Wiley-Interscience Publication, Orleans, 1999).
- [4] L. S. Frost, Phys. Rev. **105**, 2 (1957).
- [5] T. Gyergyek, and J. Kovačič, Phys. Plasmas **22**, 093511 (2015).
- [6] D. P. Lymberopoulos, and D. J. Economou, J. Res. Natl. Inst. Stand. Technol. **100**, 473 (1995).
- [7] T. Panagopoulos, and D. J. Economou, J. Appl. Phys. **85**, 7 (1999)
- [8] A. Douglass, V. Land, K. Qiao, L. Matthews, and T. Hyde, Phys. Plasmas **19**, 013707 (2012).
- [9] V. Land, L. S. Matthews, and T. W. Hyde, Phys. Rev. E, **81**, 056402 (2010).
- [10] A. Douglass, V. Land, L. Matthews, and T. Hyde, Phys. Plasmas **18**, 083706 (2011).
- [11] K. Takahashi, J. LIN, M. Hénalt, and L. Boufendi, IEEE Trans. Plasma Sci. **46**, 704 (2018).
- [12] M. Schwabe, and D. B. Graves, Phys. Rev. E **88**, 023101 (2013).
- [13] J. Goree, Plasma Sources Sci. Technol. **3**, 400 (1994).
- [14] H. M. Thomas, G. E. Morfill, V. E. Fortov, A. V. Ivlev, V. I. Molotkov, A. M. Lipaev, T. Hagl, H. Rothermel, S. A. Khrapak, R. K. Suetterlin, M. Rubin-Zuzic, O. F. Petrov, V. I. Tokarev, and S. K. Krikalev, New J. Phys. **10**, 033036 (2008).
- [15] P. K. Shukla, A. A. Mamun, *Introduction to Dusty Plasma Physics*, (IOP series of plasma Physics, 2002).



# Chapter 7

## Particle behaviours in RF plasmas

As mentioned in the introduction, in industries, researches of dusty plasmas has interests both to avoid dust contamination and to synthesis dust particles as materials from the plasmas.[1, 2, 3, 4]

The formation of dust particles from reactive gas is studied in the Chapter 4. This chapter focuses on the transport behaviours of dust particles in the RF plasmas.

It is known that in the RF plasmas, particles get negative charge and are confined in the plasmas.[6, 5, 7, 8, 9] The objective of this chapter is to make clear next points. 1) At which position in the chamber dust particles levitate. 2) How the dust particles transport when the discharge conditions are modified. 3) In which conditions dust particles can levitate in the plasmas or drop from them. 4) Dust particle behaviours in function of particle size. 5) To be able to control the transport of dust particles in the discharge chamber. In order to analyse the transport behaviours of dust particles, the charge[6, 5, 7, 8, 9, 10] and the forces[6, 5] acting on the dust particles are discussed.

Experiments were performed in the PK3-plus chamber[11, 12]. Industrially fabricated dust particles with determined diameter were used in the experiments. Dust particles could be injected into the reactor chamber by the injector[11, 13, 14], then illuminated by the laser of 523 nm in wavelength and observed by the CCD camera. Argon gas was fed as the discharge gas.[12] Pulse-time modulation, which is discussed in the Chapter 5, is applied to the RF power in order to regulate electron temperature. The frequency of the pulse-time modulation is set at 10 kHz, which is the optimal frequency to regulate the electron temperature for this experimental set up according to the results shown in the Chapter 5.

Duty cycle of the pulse-time modulation and peak-to-peak RF voltage are the main factors to regulate. The transport behaviours of dust particles are observed under the regulation of the two factors. The double-probe[15] is used to measure the plasma parameters. The calculation methods discussed in the Chapter 6 are applied. By substituting the measured plasma parameters to the calculation methods, the transport behaviours of dust particles are analysed numerically or analytically, and the mechanisms are explained.

Diagnostics of plasmas are performed before the observation of the behaviours of dust particles. How the electron temperature and ion density vary with the regulation of the pulse-time modulation and RF voltage is discussed. After knowing the character of the discharge, transport behaviours of the dust particles of mono-dispersed size were firstly studied. Then, the factor of particle size is investigated

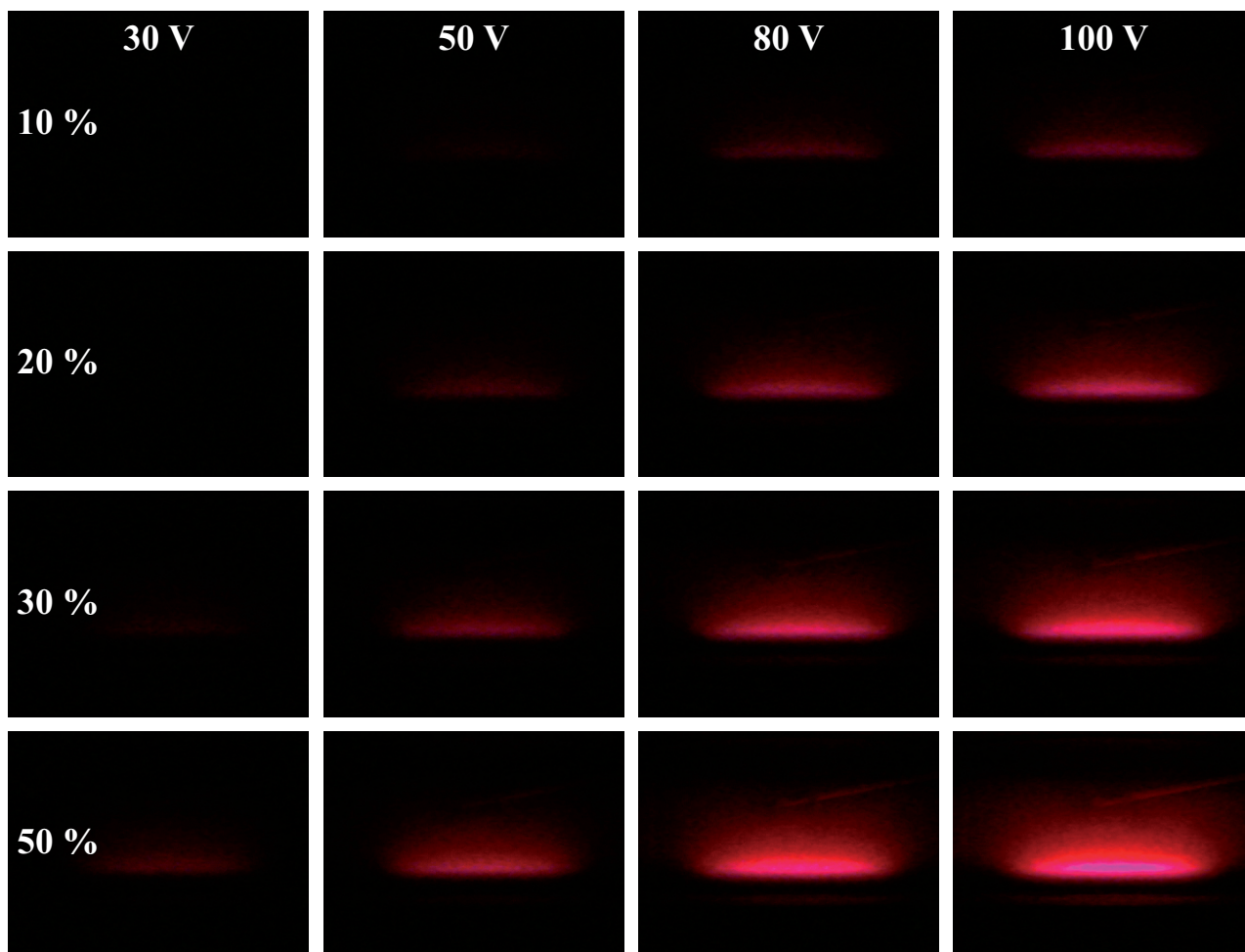


Figure 7.1: Photographes of RF plasmas under different discharge conditions. Pressure is 400 mtorr. Frequency of pulse-time modulation is 10 kHz. Duty cycle of pulse-time modulation varies from 50% to 10%. RF voltage varies from 30 to 100 V.

by injecting dust particles of two sizes into the plasmas. Finally, the realisation of classification of one size particles from other sizes in pulse-time modulated RF plasma is discussed.

## 7.1 Diagnostic of RF discharge

Diagnostics of plasma proprieties were performed in order to study how the presence of dusty particles, effect of pulse-time modulation and regulation of RF power give influence to the RF discharge. Light emissions were observed by the CCD camera, the electron temperature and ion density were measured by the double langmuir probe.[15]

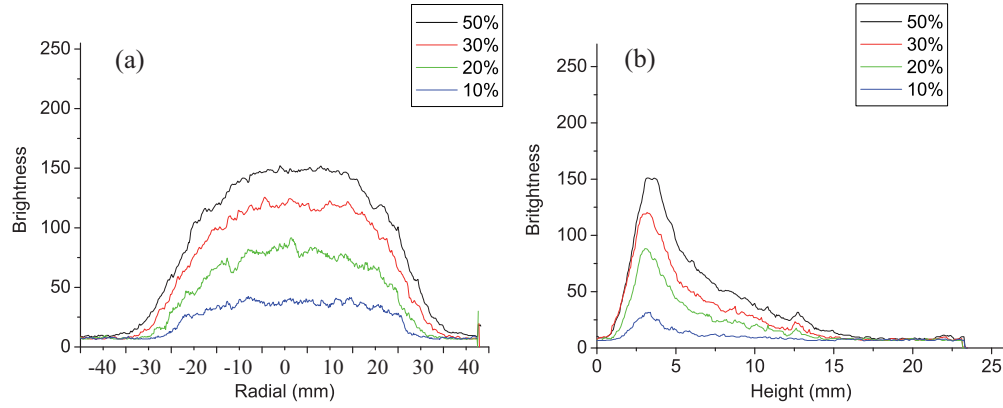


Figure 7.2: Plots of brightness extracted from the photographs in (a) radial and (b) height direction. Pressure is 400 mtorr. RF voltage is 100 V. Pulse-time modulation is applied with frequency of 10 kHz. Duty cycle of modulation varies from 50% to 10%.

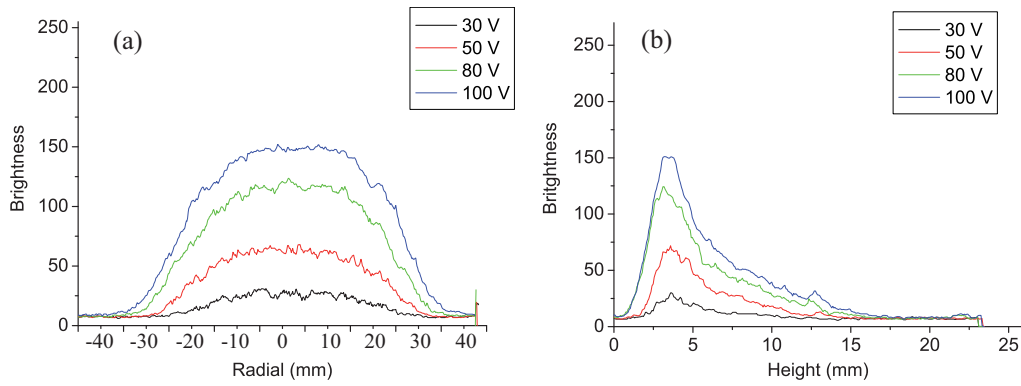


Figure 7.3: Plots of brightness extracted from the photographs in (a) radial and (b) height direction. Pressure is 400 mtorr. Pulse-time modulation is applied with frequency of 10 kHz and duty cycle of 50%. RF voltage varies from 100 to 30 V.

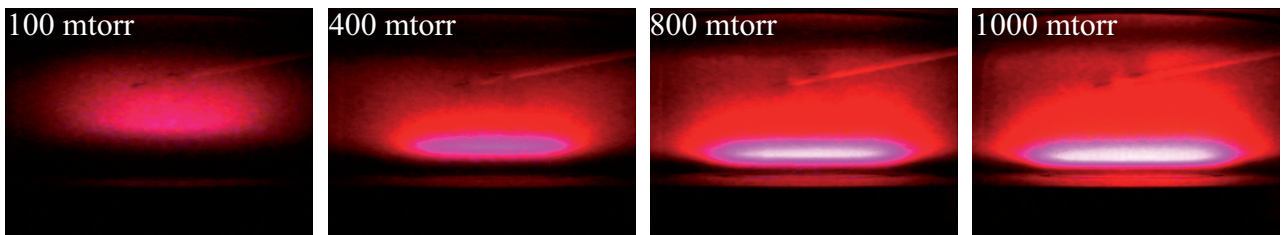


Figure 7.4: Photographs of RF plasmas under different gas pressure without pulse-time modulation. RF voltage is fixed to 100 V. Pressure varies from 100 to 1000 mtorr.

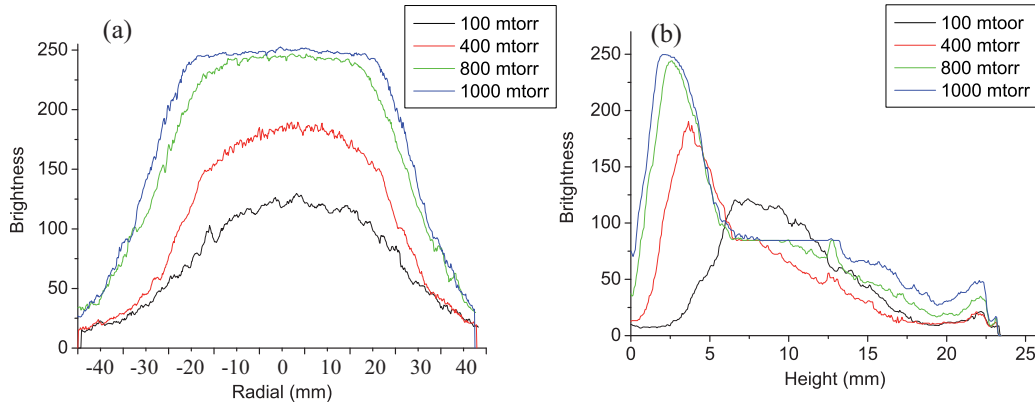


Figure 7.5: Plots of brightness extracted from the photographs in (a) radial and (b) height direction, in function of gas pressure. RF voltage is fixed to 100 V. Gas pressure varies from 100 to 1000 mtorr.

### 7.1.1 Light emission

Optic observations of the RF plasma under different discharge conditions were performed by the CCD camera. RF voltage was varied from 30 to 100 V. Pulse-time modulation was applied with 10 kHz in frequency, and duty cycle was varied from 50% to 10%. Pressure was varied from 100 to 1000 mtorr.

Figure 7.1 shows photographs of the RF plasmas when the pressure is fixed to 400 mtorr. Light emission weakens with decrease of RF voltage and duty cycle. Brightness of the photographs are extracted by imaging process. The 1-dimensional plots of brightness are extracted in vertical and horizontal directions, at radial centre and the peak point of the vertical plot of the brightness, respectively. Figures 7.2 (a) and (b) show the plot of the brightness in function of height and radial, respectively, under different duty cycles while RF voltage is fixed to 100 V. Figure 7.3 shows that under different RF voltages while the duty cycle of the pulse-time modulation is fixed to 50%. One can find a high bright area enlarge with increase of RF voltage and duty cycle.

Figure 7.4 shows photographs of the RF plasmas in function of pressure while the RF voltage is 100 V without pulse-time modulation. Pressure are 100, 400, 800 and 1000 mtorr. Figures 7.5 (a) and (b) show the 1-dimensional plots of the brightness in function of height and radial, respectively. One can see that while the pressure increases, The RF plasmas brighten and the high bright area moves from the centre in height direction to close to the powered bottom electrode. It means at different pressure, the PF plasmas have different centre.

### 7.1.2 Influence of presence of dusty particles to double langmuir probe measurements

The influence of the dust particles to the plasma parameters was examined. Electron temperature and ion density were compared between the cases with and without dust particles. A series of measurements of the electron temperature and ion density in function of height was performed without dust particles, and three other series of measurements were performed in the cases of different amount of dust particles

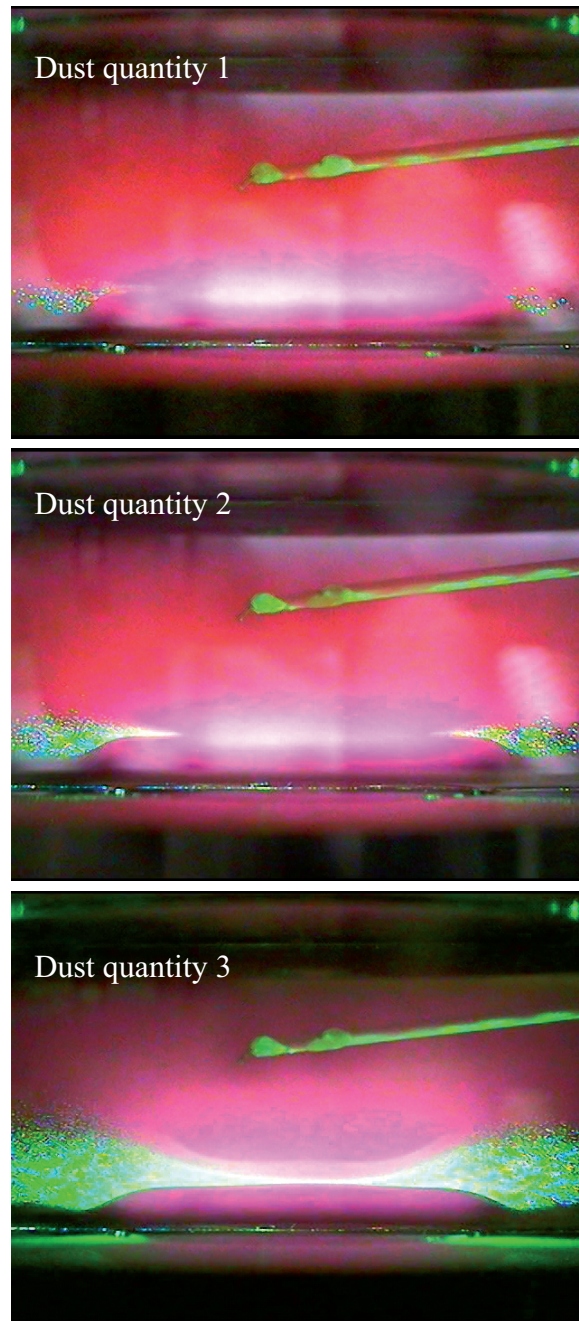


Figure 7.6: Different amount of dust particle in the reactor chamber while the double probe measurement was preformed.

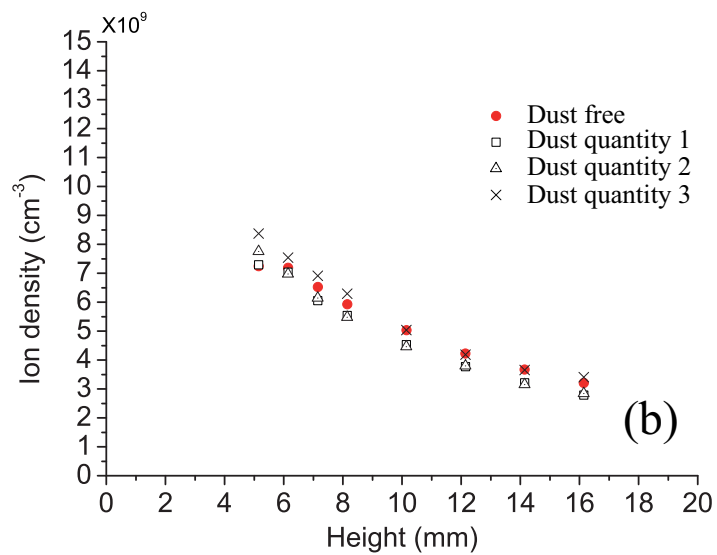
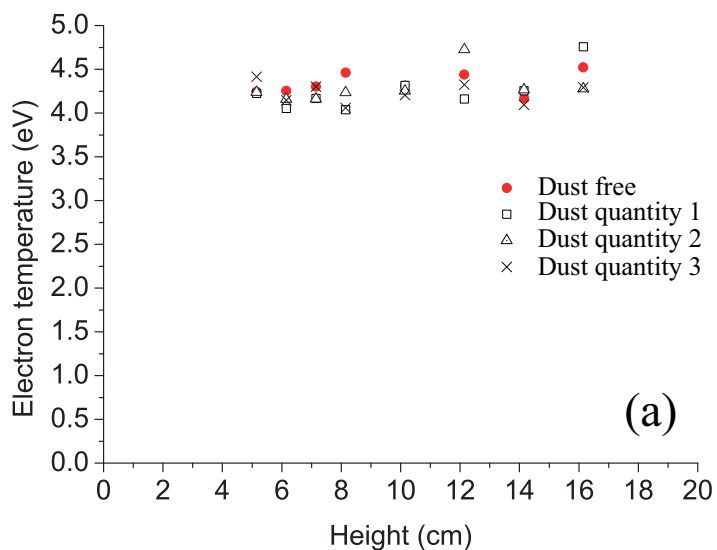


Figure 7.7: (a) Electron temperature and (b) ion density in function of height at the centre of the chamber with and without dust particles. Amount of dust particle in the chamber for each case was shown in Fig. 7.6.

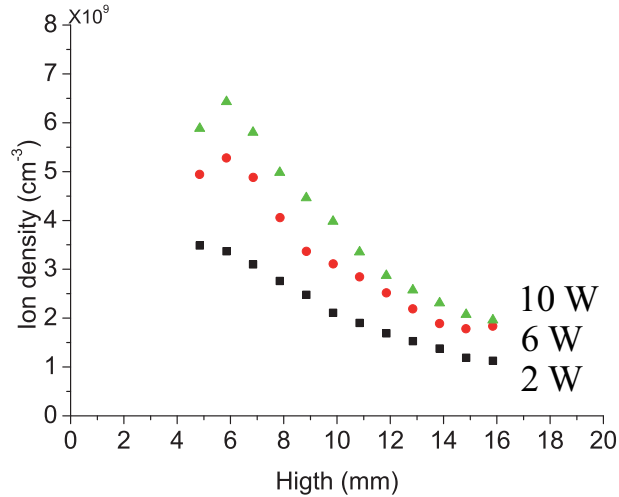


Figure 7.8: Ion density in function of height at the centre of the reactor chamber for the RF voltage of 2, 6 and 10 W.

in the plasmas. Figure 7.6 shows the amount of dust particles for the three cases of measurements with dust particles in the plasma. Figure 7.7 shows the measurement results of the electron temperature and ion density. Red markers in Figs. 7.7 (a) and (b) represent the electron temperature and ion density, respectively, measured without dust particles. One can see that the presence of dust particle of such amount (Fig. 7.6) dose not give much influence to the electron temperature and ion density for this experiment configuration. The enhancement of ion density by the presence of dust particles reported in other work[11] was not occurred. The difference is that in the case of the ion density enhancement, particles full up the plasma bulk, and form a void. Ions are confined by the dust particles and the ion density is enhanced in the void.[11] In our case, the small amount of dust particles can only influence the local place within several debye length. Results of measurements performed without dust particles are available for the discussion of particle behaviours.

### 7.1.3 Spatial distribution of ion density and electron temperature

Ion density and electron temperature in function of height were measured when RF were power 2, 6 and 10 W. Results are shown in Figs. 7.8 and 7.9 Ion density has a peak near the bottom electrode and increases with the increase of the RF power. Electron temperature dose not change with the measurement position nor with the RF power.

Electron temperature in function of duty cycle was measured when the pulse-time modulation was applied. The frequency was 10 kHz. Duty cycle varied from 90% to 10%. Figure 7.20 shows the electron temperature decreases with the decrease of the duty cycle, from 3.5 eV to 0.88 eV.

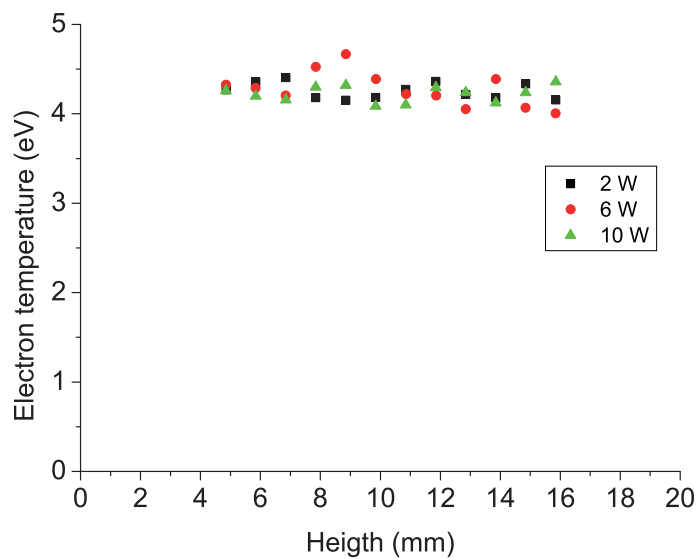


Figure 7.9: Electron temperature in function of height at the centre of the reactor chamber for the RF voltage of 2, 6 and 10 W.

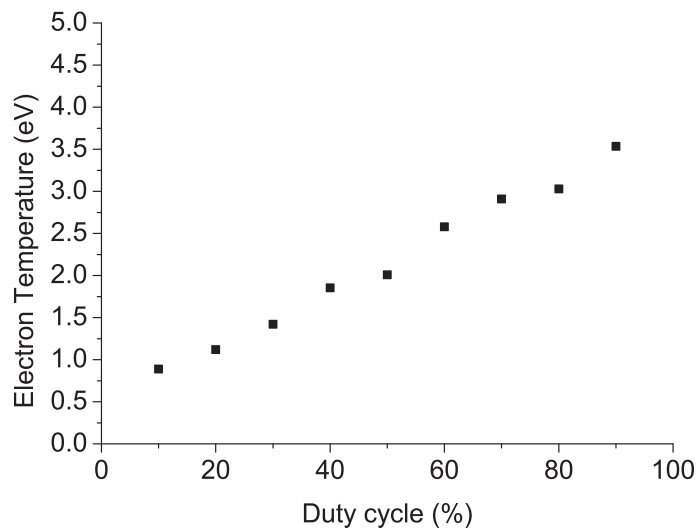


Figure 7.10: Electron temperature in function of duty cycle of the pulse-time modulation.

## 7.2 Levitating position and trajectory of dust particles transported to electrodes in dusty plasmas

### 7.2.1 Introduction

Particles of mono-dispersed size are injected into the plasmas. The levitating positions are investigated for each condition of RF voltage and pulse-time modulation. The dust particles in plasmas are charged negatively and affected by gravitational, ion drag and electrostatic forces.[5, 7] They levitate at positions where the forces get balanced in the plasmas. The positions were determined by charge of the dust particles, electric field and ion flux.[5, 7] Regulating plasma parameters can change the levitating position of the dust particles. When the forces are off balance, the dust particles fall down from the plasmas.

The positions of the dust particles when they levitate, the trajectory and the area of dust particle when they fall down from the the plasmas are in question.

### 7.2.2 Experiment

The experiments were performed in the PK-3 plus chamber with powered electrode in bottom side, and the electrode of 30 mm in diameter was used.[11] A small amount of SiO<sub>2</sub> particles of 1.05  $\mu\text{m}$  in diameter was injected into plasmas for each experiment. The amount of injected particles was controlled to be almost same for each experiment. Argon gas was fed to the chamber and the flow was set to be 4 SCCM. The pressure was maintained at 400 mtorr (52 Pa). The RF voltage (peak-to-peak) was varied from 25 V to 100 V. Pulse-time modulation was applied. The frequency of the pulse-time modulation was set to be 10 kHz. Duty cycle of the modulation was varied from 80% to 5%. A colour CCD camera with larger field of view was used to determinate levitating positions, and a monochrome high speed CCD camera with smaller field of view was used to observe the falling process of the dust particles.

### 7.2.3 Results

#### Levitating position of dust particles

Particles levitating in the plasmas were observed in three cases. 1) To vary the RF voltage from 100 V to 40 V without the pulse-time modulation. 2) To fix the RF voltage at 50 V by varying the duty cycle from 50% to 15%. 3) To fix the RF voltage at 100 V by varying the duty cycle from 50% to 15%.

Figure 7.11 shows evolution of levitating positions of the particles in function of the RF voltage. The right part of the cross section of the chamber was filmed by the camera. Left edge of the photographs is radial centre of the reactor chamber. A gap is shown in the photographs. That is the gap between the powered electrode (left) and the surrounding grounded ring (right). Distances indicated in photographs are the radial distances from the centre of the chamber. It is shown that the particles levitated in the centre of the chamber at lower RF voltage as 40 V, and they were repelled outward when the RF voltage increased. When the RF voltage was higher than 80 V, there was not particle in the centre, and the particles levitated above the edge of the powered electrode. The particle cloud has a ring like

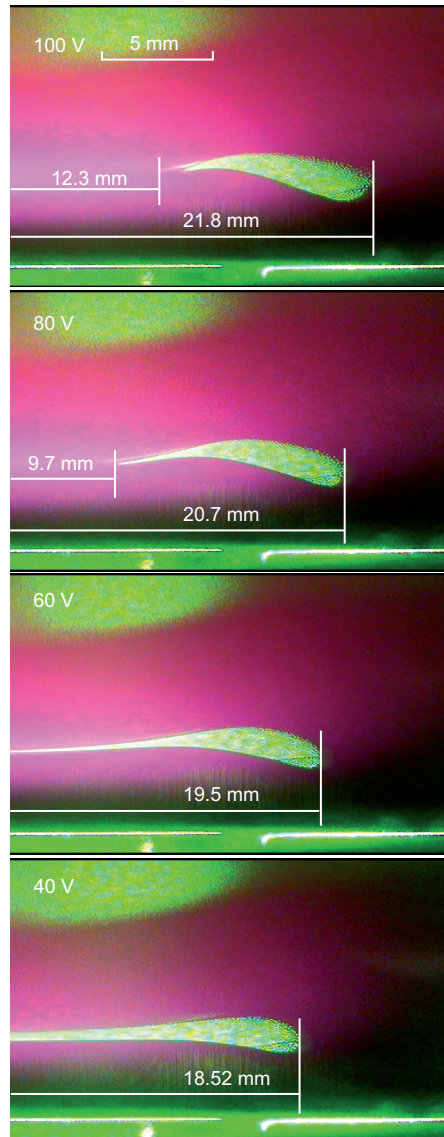


Figure 7.11: levitating positions of particles changes with RF voltage. Distances indicated in photographs are those from the centre of the chamber.

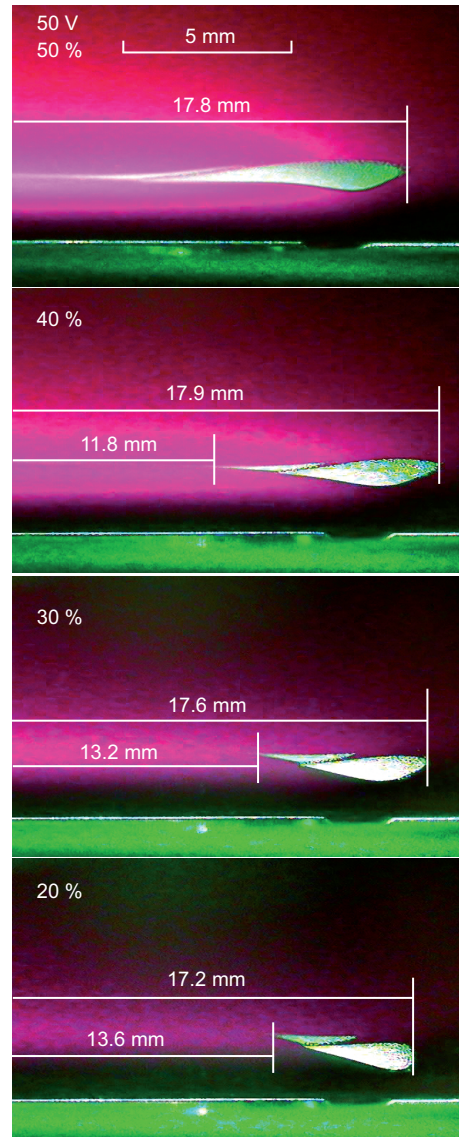


Figure 7.12: levitating positions of particles changes with modulation duty cycle, while the RF voltage is set at 50 V. Distances indicated in photographs are those from the centre of the chamber.

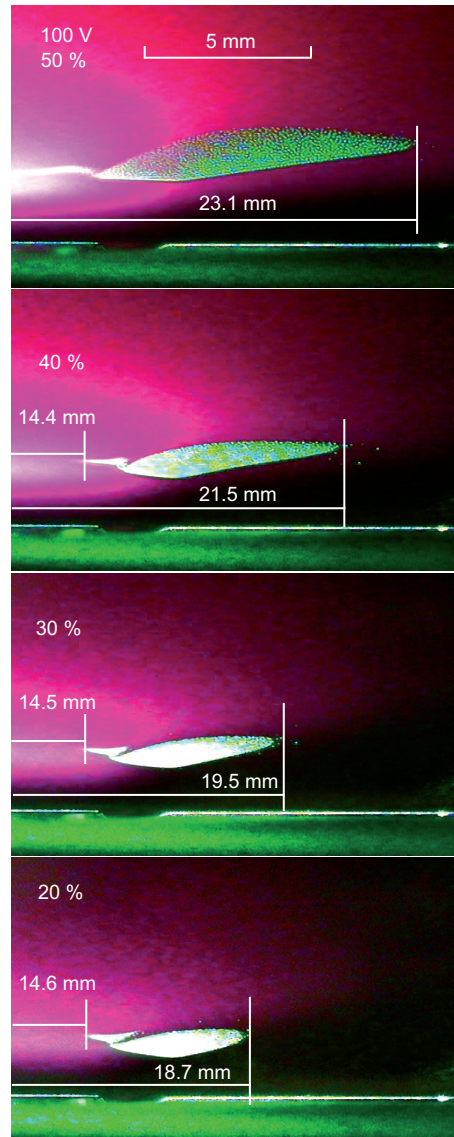


Figure 7.13: levitating positions of particles changes with modulation duty cycle, while the RF voltage is set at 100 V. Distances indicated in photographs are those from the centre of the chamber.

form in the 3-dimensional view. When the RF voltage increased from 80 V to 100 V, both radius of the inside edge and outside edge of the particle cloud increase, particles were entirely carried outward.

Figure 7.12 and 7.13 show evolution of the levitating positions of the particles in function of the modulation duty cycle when the pulse-time modulation is applied. Figure 7.12 shows the case that the RF voltage was 50 V. Initially particles levitated above the powered electrode, in the centre of the chamber. While the duty cycle decreased, the particles were repelled from the centre to the edge of the powered electrode and levitated above the gape. Figure 7.13 shows the case that the RF voltage was 100 V. Initially most of particles levitated above the surrounding grounded ring. While the duty cycle decreased, the particles go inward and finally levitated above the gape. By combining the figs. 7.12 and 7.13, one can see that the decrease of duty cycle result in the convergence of the particles around the edge of powered electrode.

### **Falling down positions of dust particles**

To observe the falling down process and examine the positions, two situations were taken into account: to fall the dust particles by maintaining the plasma on and to fall them by switching off the plasma.

When the RF voltage was 25 V and the duty cycle of modulation was 80%, the dust particles levitated above the the bottom side powered electrode. Decreasing the duty cycle, the dust particles in centre were repelled outward. When the duty cycle is decrease to 15%, the dust particles started to fall down to outside of the powered electrode in an area of 17.2 ~ 18.0 mm from the axis centre of the chamber. When the RF voltage was 50 V, the dust particles fall down into an area of 19.9 ~ 21.5 mm from the axis centre while the duty cycle decreased to 12 ~ 9%. When the RF voltage was 75 V, the dust particles fall down into an area 24.2 ~ 20.6 mm from the axis centre while the duty cycle decreased to 11% ~ 5%. (Fig. 7.14) Since the reactor chamber has axe symmetrical geometry, the fallen dust particles forme a fine ring on the bottom electrode as shown in Fig. 7.15 . Due to the RF voltage, particles can be controlled to fall in different areas.

When the RF voltage was shut down, the dust particles fell all together from the position where they were levitated. In the cases of the RF voltage 25, 50 and 75 V without pulse-time modulation, the dust particles were levitated above the bottom side powered electrode. After the RF voltage switched off, the dust particles fall down into circle areas whose radius were 21.9, 24 and 23.4 mm, respectively. The dust particles covered whole the powered electrode surface. (Fig. 7.16)

### **Falling down trajectory observed by hight speed camera**

The precesses of particles falling down were filmed by the hight speed camera with 200 FPS. The difference between the two cases were observed: (1) to fall the dust particle by switching off the plasma, (2) to fall the dust particle by applying time-pulse modulation and decreasing the duty cycle.

Particle tracking analyse was applied to the filmed falling processes.[16, 17] Position and speed of each particles were extracted for each frame. Figures 7.17 (a) and (b) shows the trajectories of dust particles when they were falling down for the case of (1) and (2) respectively. Figures 7.18 and 7.19 show the speed vector and position of each particles during the falling down process for the case of (1) and (2) respectively. The arrows represent the vector of speed of particles.

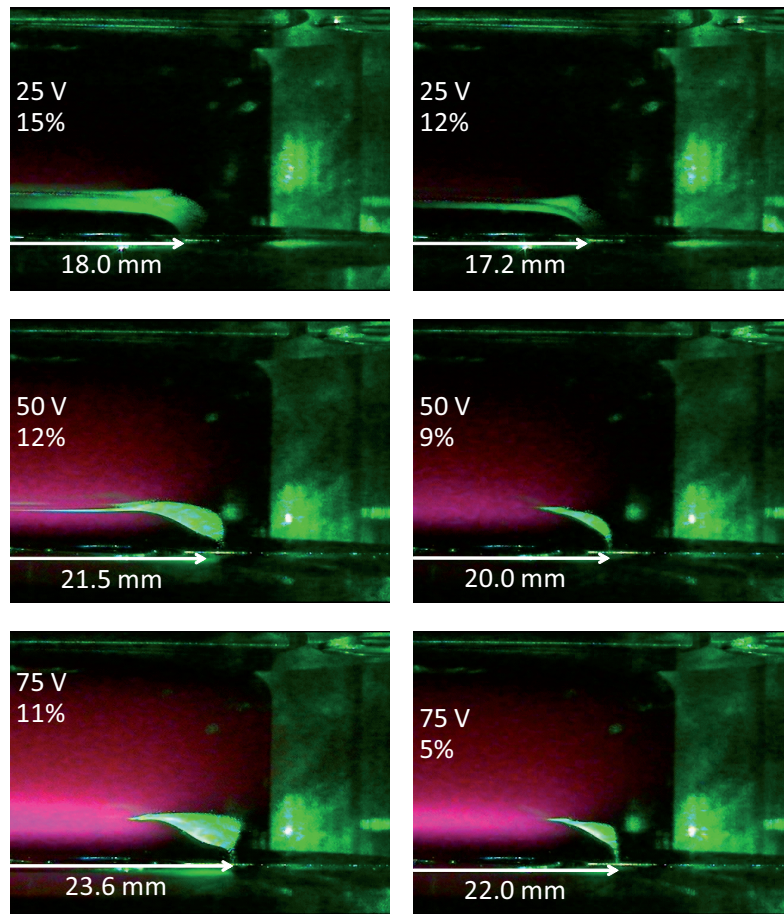


Figure 7.14: Particles fall down by applying time-pulse modulation and decreasing modulation duty cycle when the RF voltages are set at 25, 50 and 75 V.

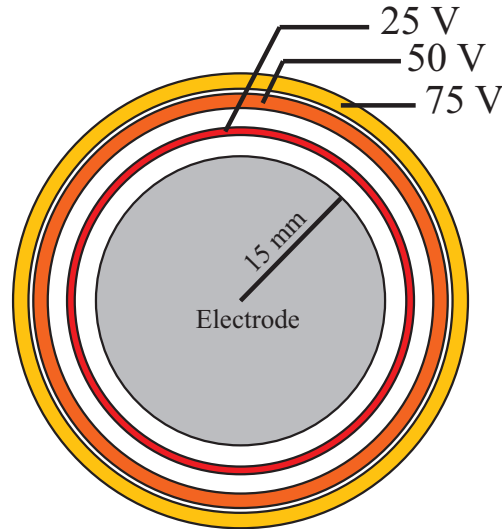


Figure 7.15: Top view of areas for particles fallen. Particles form rings with different diameters on the bottom side due to the RF voltage.

In the case (1), all particles started to fall down once the RF power was shut down. Particles gained vertical speed towards the bottom side by gravitational force. After almost  $125 \mu\text{s}$  the first particles reach the bottom side. Other particles continue to fall down till 1 s. Some particles gain horizontal speed near the electrode. That can be assumed to be caused of the charge remained in the particles and in the electrode. The electrode, connecting to a capacitance, takes time to neutralise its charge. After the shutting of RF power, electric field of ambipolar diffusion and sheath vanished, and then the electric field due to the charge remaining on the electrode establish.

In the case (2), plasma remains turned on. Decreasing duty cycle, particle at the lowest layer started to fall down while the others still levitate in the plasma. The particles falling down have an arcuated trajectory and avoid the powered electrode. Not only the gravitational force, but also a outward force act on the particles in horizontal direction.

#### 7.2.4 Discussion

Regulation of the duty cycle of time-pulse modulation and the RF voltage give influence to the particle levitation. Previous work shows that the time-pulse modulation can regulate the electron temperature of the plasma. Electron temperature decreases while the modulation duty cycle decreases. Ion density increases while the RF voltage increases. Ion density and electron temperature are the plasma parameters which are the cause of the particle behaviours of levitation and falling.

Particles are charged negatively in the bulk of plasma and the sheath. In the bulk of plasma, electron temperature and particle dimension are main factor for the particle charge. Figures 7.20 (a) and (b) shows the particle charge in function of electron temperature and ion density respectively. The charge of particle of  $1.05 \mu\text{m}$  in diameter is resolved numerically. Figure 7.20 (a) shows the result when electron temperature varies between  $0.5 \sim 5 \text{ eV}$ , while  $n_i = 4 \times 10^9 \text{ cm}^{-3}$ . Particle charge

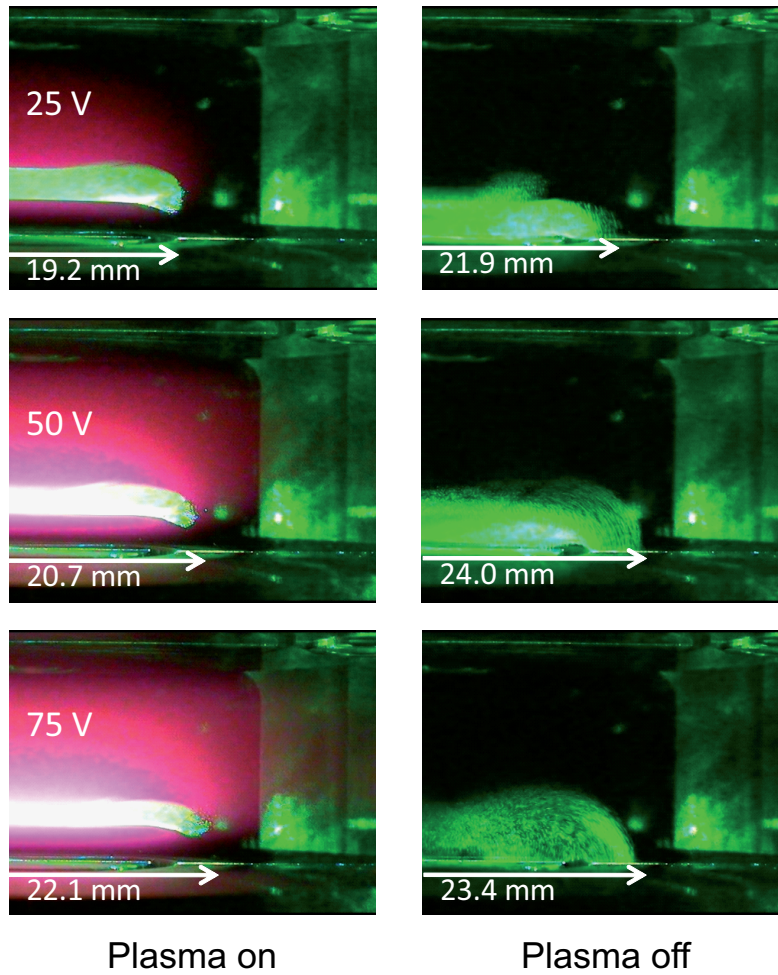


Figure 7.16: Particles fall down by shutting down RF power when the RF voltages are set at 25, 50 and 75 V.

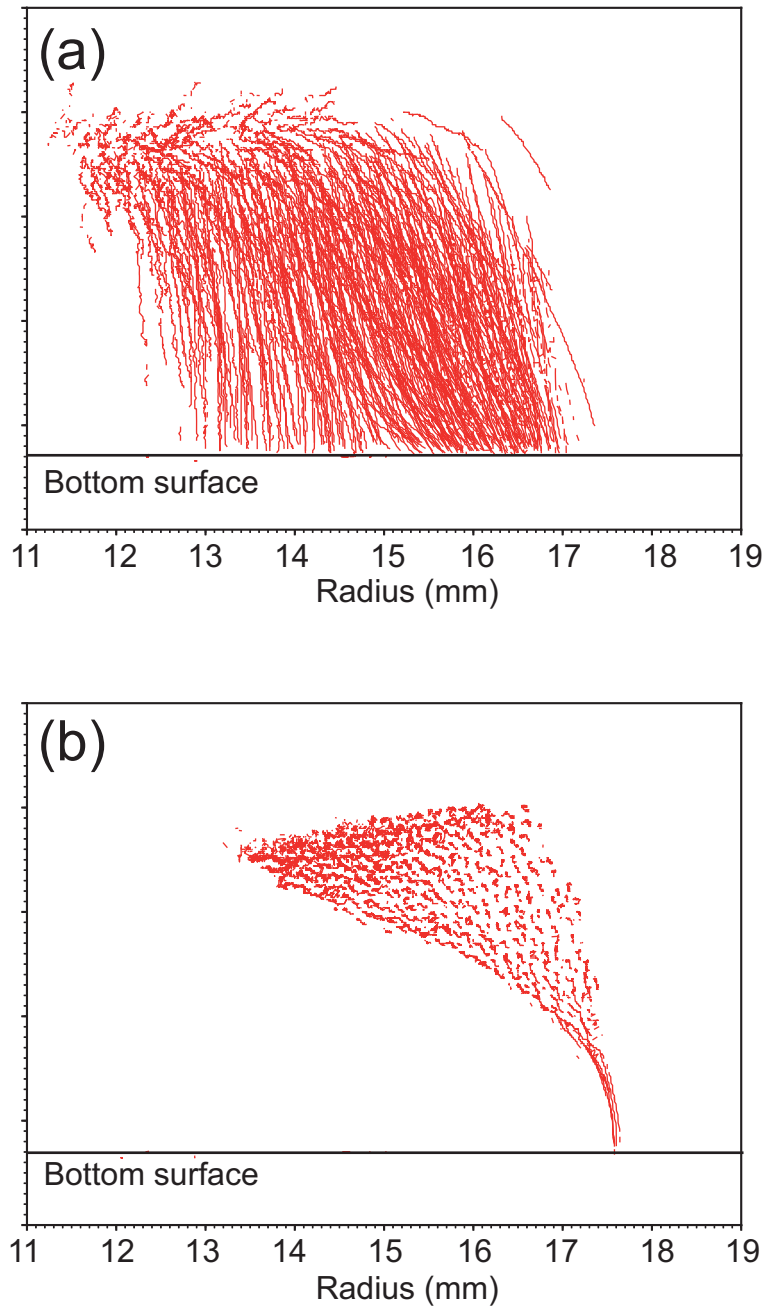


Figure 7.17: Falling down trajectory of particles observed by high speed camera. (a) The Falling down trajectory of particles by shutting down RF power. (b) The Falling down trajectory of particles by applying time-pulse modulation and decreasing modulation duty cycle.

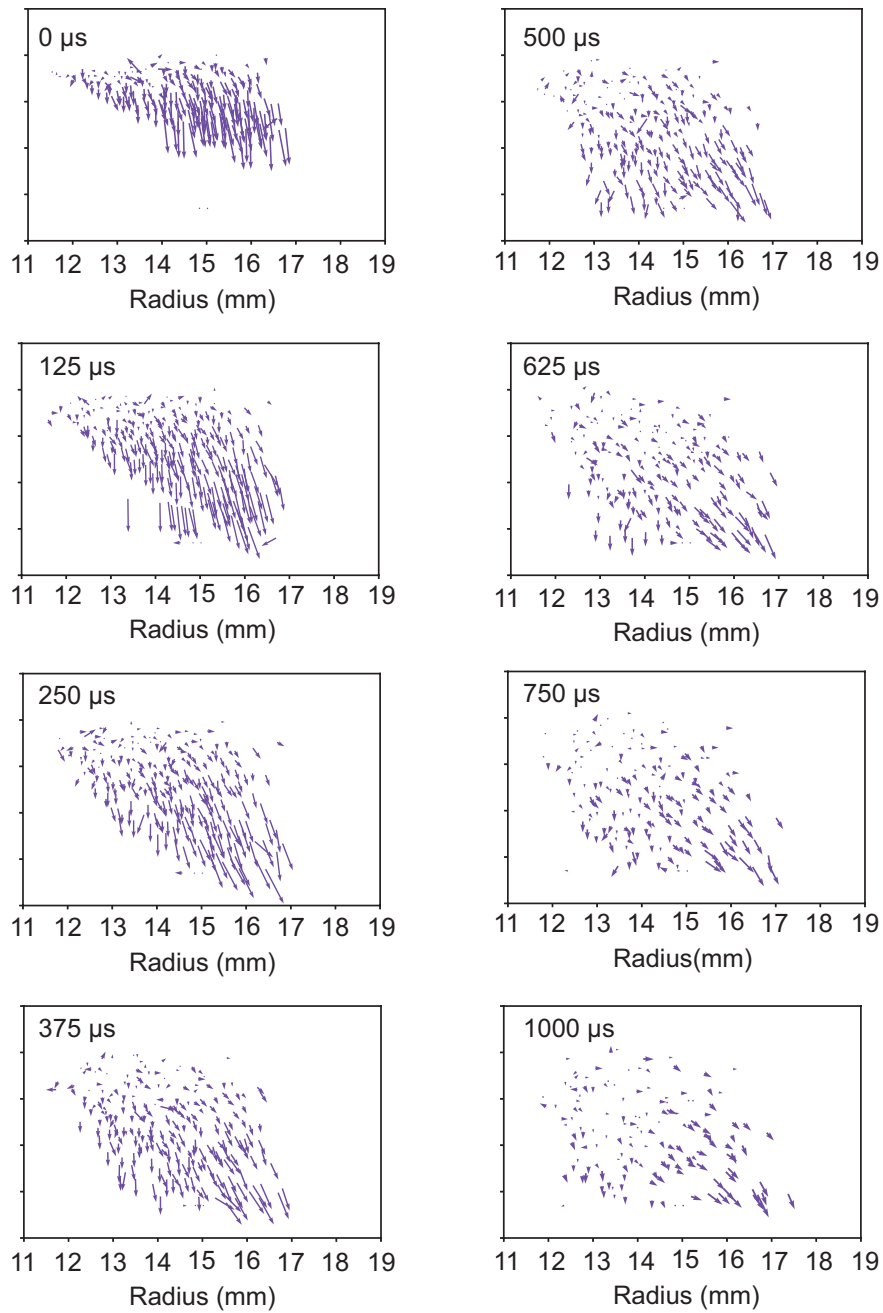


Figure 7.18: Falling down process of particles by shutting down RF power, Particles are filmed by high speed camera and analysed by particle tracking. Arrows represent particle speed and current position.

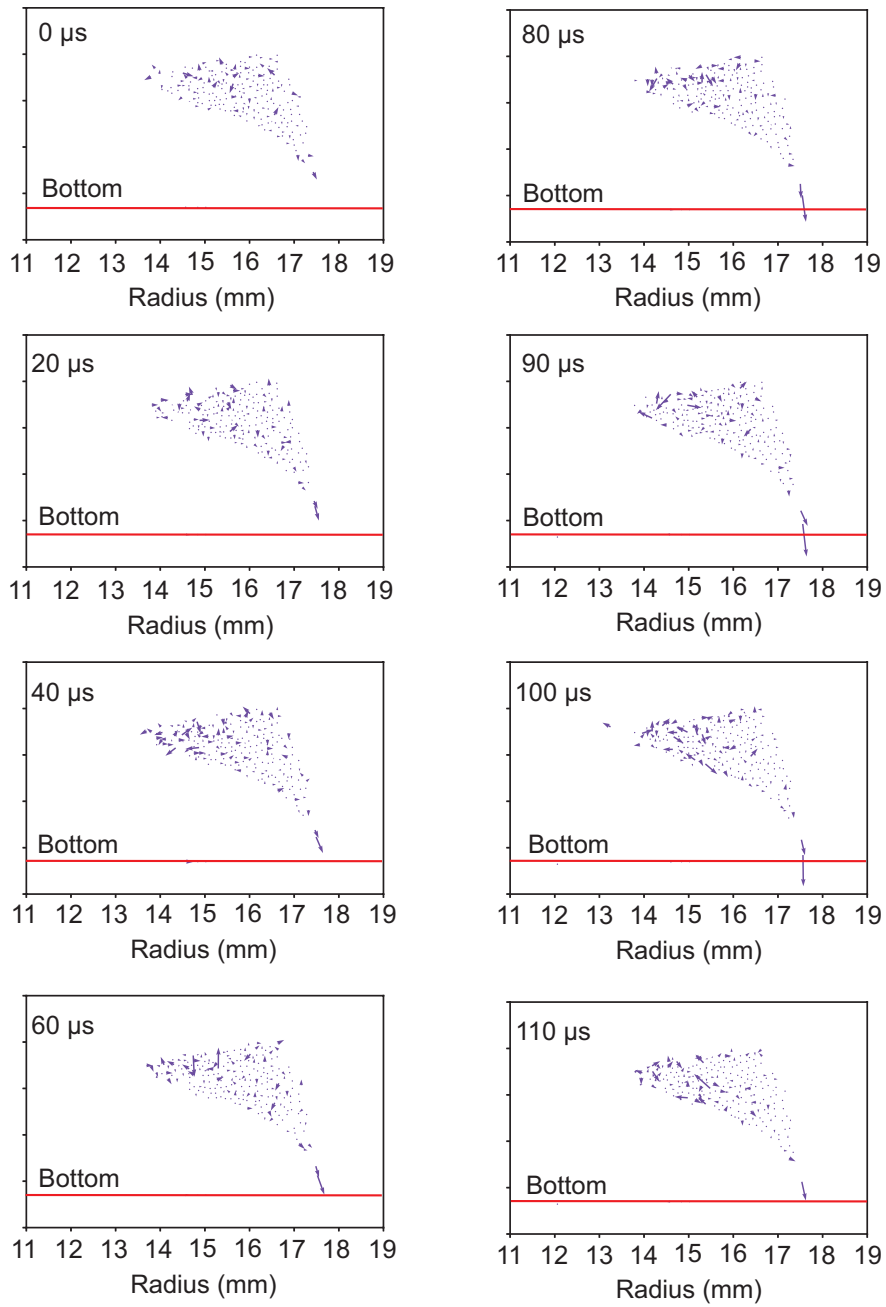


Figure 7.19: Falling down process of particles by applying time-pulse modulation and decreasing modulation duty cycle. Particles are filmed by high speed camera and analysed by particle tracking. Arrows represent particle speed and current position.

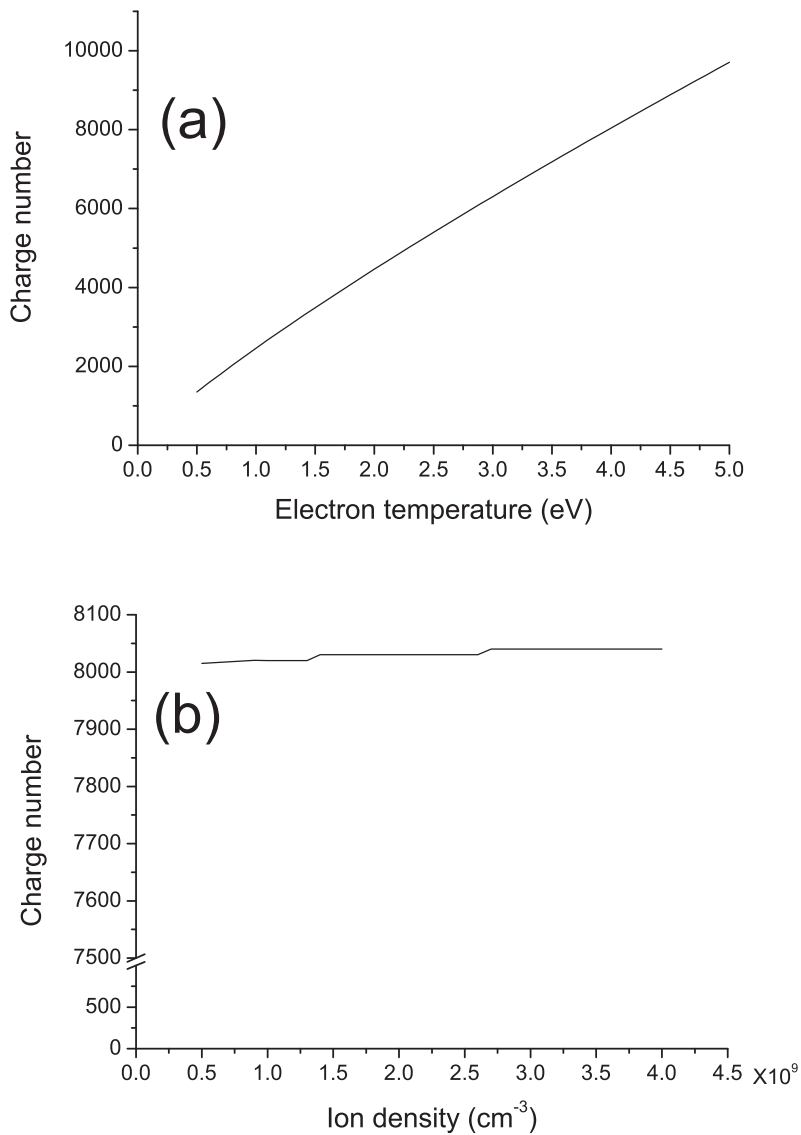


Figure 7.20: (a) Particle charge in function of electron temperature. (b) Particle charge in function of electron/ion density.

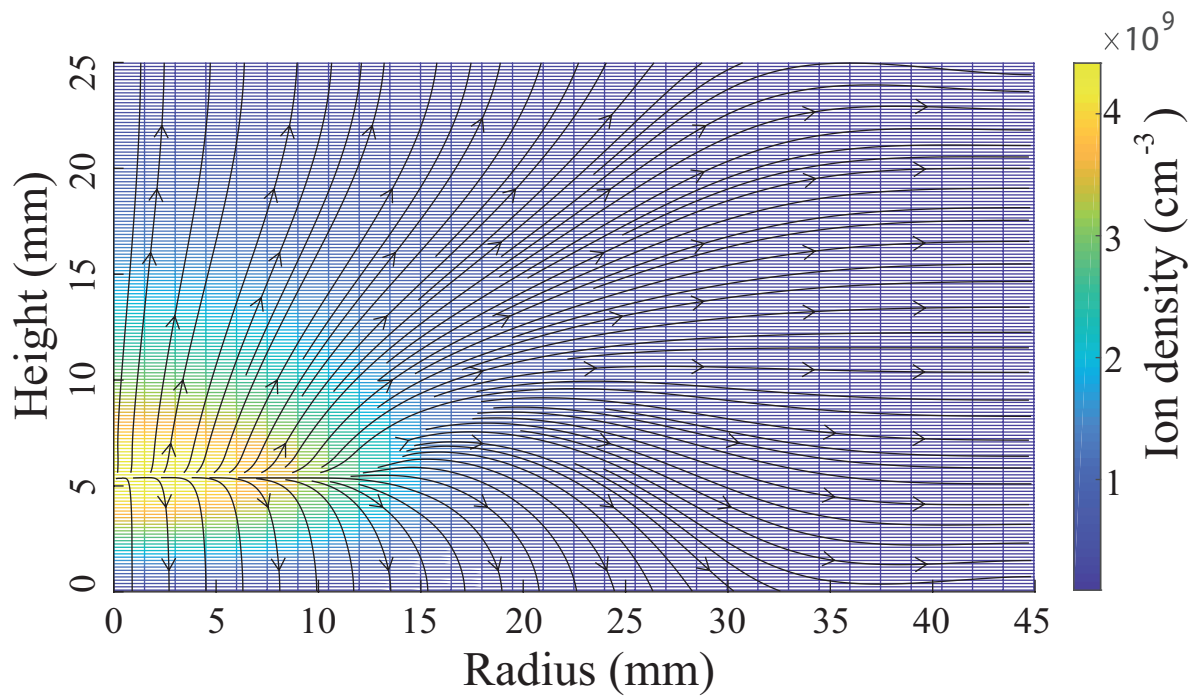


Figure 7.21: Simulated ion density distribution, represented by colour bar, and ion ambipolar flow direction, represented by stream with arrow. Half cross section of chamber is represented by radial axis and height axis.

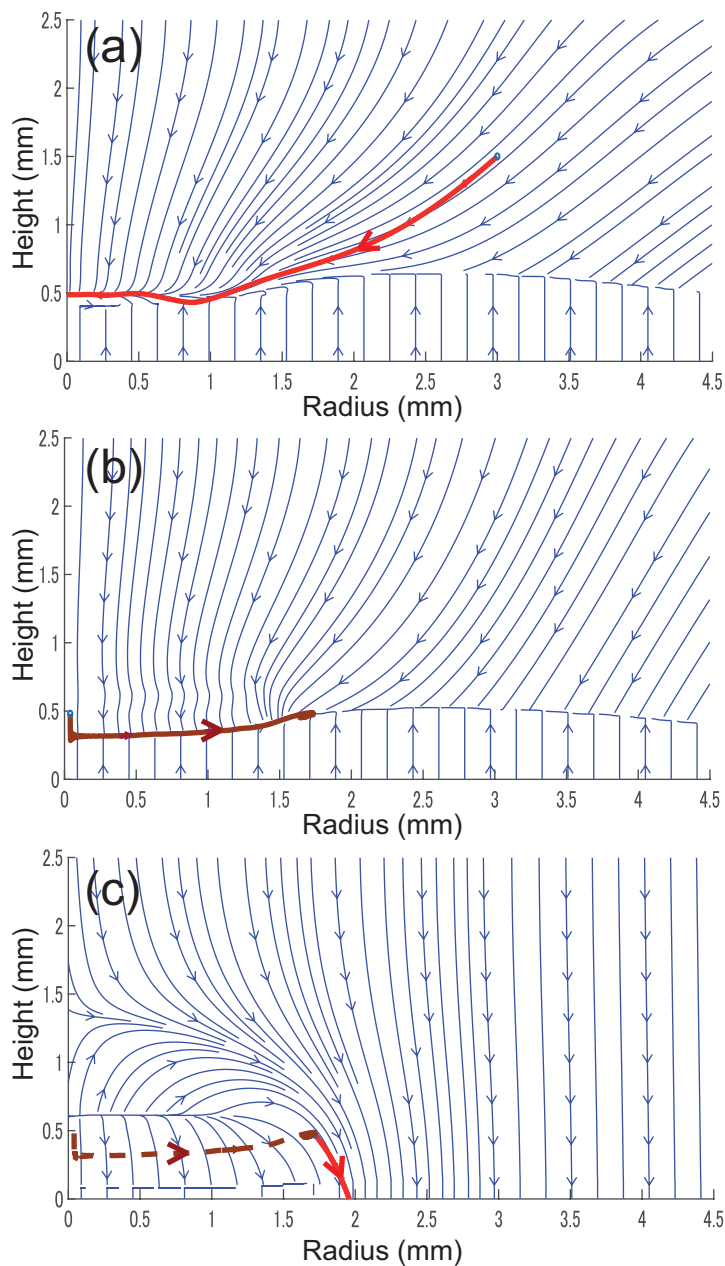


Figure 7.22: Simulated resultant force acting on the particle in a half cross section of chamber. RF voltage is 50 V in the case: (a) without modulation, (b) applying modulation with duty cycle 20% and (c) applying modulation with duty cycle 5%. The streams with arrow represent the direction of resultant force acting on particle. The red and brown line represent simulated trajectory of particle in this space.

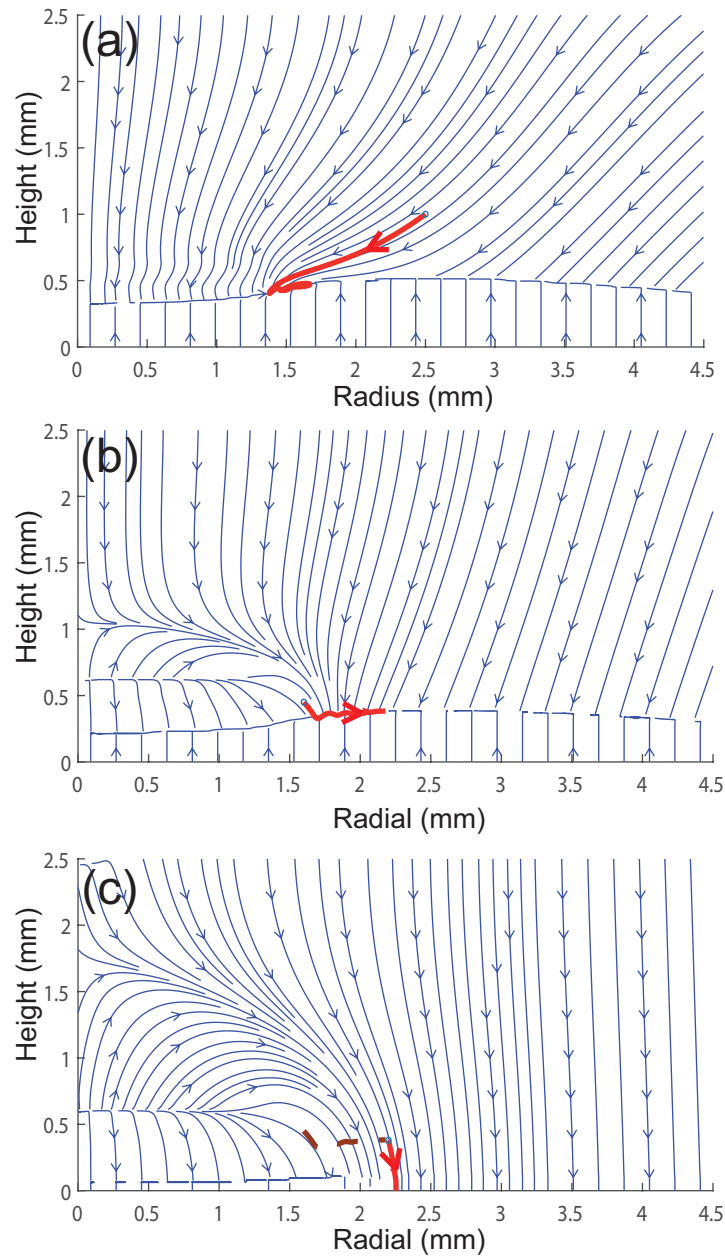


Figure 7.23: Simulated resultant force acting on the particle in a half cross section of chamber. RF voltage is 75 V in the case: (a) without modulation, (b) applying modulation with duty cycle 20% and (c) applying modulation with duty cycle 5%. The streams with arrow represent the direction of resultant force acting on particle. The red and brown line represent simulated trajectory of particle in this space.

varies from 1350 to 9700 e. Figure 7.20 (b) shows the result when ion density varies between  $0.5 \sim 4 \times 10^9 \text{ cm}^{-3}$  while  $T_e = 4 \text{ eV}$ . Particle charge varies from 8015 to 8040 e. Within the typical variation range of electron temperature and ion density for this experiment setup, electron temperature has more influence to the particle charge. The influence of the ion density to the particle charge could be neglected.

Particles are acted by gravitational, ion drag and electric forces. When the forces get balanced, particle levitates at the balanced position. In the case of multiple particles levitate in the plasma, interparticle force should be taken into account. Caused of the negative charge, particles repel each others. More the particles are charged, more the distance interparticle enlarge. In the bulk of the plasma, the electric field is created by ambipolar diffusion. The electric force by ambipolar electric field has a direction opposes to the ion drag force by the ambipolar diffusion flow. In the sheath, the electric field is created by electron depletion. The sheath structure can be calculated by Child-Langmuir law.[22, 24, 25]

Ion density distributions are simulated by the fluid model by taking into account the ambipolar diffusion, continuity equation and chamber dimension.[8, 9, 6] Ion flow and ambipolar electric field can be calculated from the ion density distribution.[22, 24] Figure 7.21 shows an example of the calculated ion density distribution and ion flow stream, represented by colour bar and arrows respectively. Half sectional view in right side of the chamber is represented. 0 position of radial is the centre of the chamber and Radial=45 mm is the wall.

Based on the simulated ion density distribution and sheath structure, forces act on particle are calculated in whole space.[6, 22, 24] Figures 7.22 and 7.23 show the simulated resultant force (gravitational, ion drag, and electric forces) with and without pulse-time modulation in the cases  $V_{rf}=50 \text{ V}$  and  $V_{rf}=75 \text{ V}$  respectively. Arrows represent force stream. Red and brown lines are simulated particle motion trajectory.

When  $V_{rf}=50 \text{ V}$  without modulation, as shown in Fig. 7.22 (a), ion drag force is everywhere smaller than electric force by the ambipolar electric field. Resultant force converge to the centre. Red line represents the simulated particle trajectory when a particle is injected into the plasma. Negatively charged particle is carried by electric force to the centre and then levitate in the bulk of plasma. In this case, particles are supported by the electric field of ambipolar diffusion in the bulk of plasma. In the case  $V_{rf}=75 \text{ V}$  without modulation, as shown in Fig. 7.23 (a), ion density is higher than that of  $V_{rf}=50 \text{ V}$ . Ion drag force in the centre area is higher than electric force. As simulation result shown in Fig. 7.23 (a) by the red line, injected particles have a balanced position of forces around Radial=1.5 cm. Particles levitate at the sheath boundary. The increase of ion density by increasing RF voltage leads the increase of the diffused ion flow. Ion drag force increase, so that particles are repelled outward.

When the pulse-time modulation is applied and the duty cycle decreases, electron temperature decreases. That lead the decrease of particle charge. The decrease of particle charge leads the decrease of interparticle distance. That results the convergence of particles by decreasing duty cycle as shown in Figs. 7.12 and 7.13.

The decrease of particle charge leads also the decrease of electric force acting on the particles. Comparing the ion drag and electric forces, the electric force decreases more than the ion drag force when the particle charge decreases. The force balance is broken. Particles are repelled by ion flow

to the new balanced position, as shown in the Fig. 7.22 (b) and 7.23 (b). The red and brown line represent the trajectories of particle when the pulse-time modulation is applied with duty cycle of 20%.

Once the electric force in the sheath can no longer support particle weight and the ion drag force toward the electrode, particle fall down. The ion density is not homogenous along the radial direction as shown in Fig. 7.21. The area above the powered electrode has high ion density and that decrease dramatically near the edge of the powered electrode and the grounded ring. This effect leads that the electric field of the sheath above the powered electrode is much stronger than that above the grounded ring. Decreasing modulation duty cycle, while the electric field above the grounded ring can not support particle, there is still strong enough electric field in the sheath above the powered electrode to prevent particles fall down onto the powered electrode. Simulation results are shown in the Figs. 7.22 (c) and 7.23 (c). Red lines are the simulated trajectories of particle when the modulation duty cycle is decreased 5%. The particle falls down to positions near 2.0 and 2.3 cm in radial direction from the centre of chamber. While the RF voltage is set at 75 V (Fig. 7.23 (c)), the particle falls down to a position further than that at 50 V (Fig. 7.22 (c)). The simulation results correspond to the experimental observation.

### 7.2.5 Conclusion

Motion of particles in plasma is observed by regulating RF voltage and applying pulse-time modulation. The increase of RF voltage repels particles outward from the centre of chamber. The pulse-time modulation with decrease of duty cycle lead particles converge to a point near the edge of the powered electrode. The converge point depends on the RF voltage. When the duty cycle of the modulation decreases low enough, particles start to fall down to the bottom. The falling down processes of particles are examined in two cases. To cut RF power leads particles fall down all together from where they levitated to a large area on the bottom side. While applying the pulse-time modulation and decreasing duty cycle, particles can fall down gradually to a limited area out side of the powered electrode. The area at where particles fall down can be controlled by the RF voltage. Higher the RF voltage, particles fall down to outer side. Forces acting on particles are calculated in the chamber and trajectory of a test particle trajectories are simulated by the calculation result of forces. The simulation results correspond to that of experiments.

## 7.3 Segmentation of particles in their size

Particles of two sizes in dusty plasmas are discussed in this section. As known, negatively charged dust particles in plasmas are acted by gravitational, ion drag, electrostatic and neutral drag forces.[6] The difference of force balance between different sized particles is assumed to cause the segmentation of particles in size. In this work, neutral gas flow and temperature gradient were not considered. We study about the effects of the bulk of plasmas on particles. In the bulk of plasmas, ambipolar diffusion and ionization are considered to be the dominate processes.[24, 11] Ion drag force is due to ambipolar diffusion flow. Electrostatic force is due to ambipolar electric field. Ambipolar diffusion and ionization processes lead a non homogeneous ion density in the bulk of plasmas. The spatial distribution of ion

density determines local ambipolar diffusion flow and electric field.

In experiments, we observe that increase of RF peak-to-peak voltage changes the direction of segmentation of the dust particles from vertical to horizontal. A horizontal distribution is suitable for particle classification in our cases. One dimensional distributions of ion density in vertical direction are measured by a double-probe method.[11, 15] In analyses, a fluid model[7, 11, 18, 19] is used to calculate the spatial distributions of ion density, and the spatial distributions are fitted to the measured parameters. Ion drag and electrostatic forces are calculated from the spatial distributions of ion density. Force-balanced positions for the dust particles different in sizes in each discharge condition are calculated. This explains the segmentation behaviours changed by RF voltage. In this work, small amount of the dust particles is contained in plasmas. Therefore, the effect of the dust particle on the plasmas and interaction between the dust particles are not considered.

### 7.3.1 Experimental

Experiments were performed in the PK-3 plus[11] reactor with an upper and a bottom electrode of 90 mm and 30 mm in diameter respectively. The argon gas was fed as the discharge gas. The gas pressure was set at 80 Pa. Gas flow was set at 0.4 SCCM (standard condition cubic centimetre per minute). Two dust particle dispensers were mounted on the top of the reactor, one contained MF (melamine-formaldehyde) particles of  $2.55 \mu\text{m}$  in diameter, and the other contained  $\text{SiO}_2$  particles of  $1.05 \mu\text{m}$  in diameter. The dust particles could be injected by driving a voltage from a pulse generator, and the amount of the dust particles could be regulated by pulse width. A small amount of two kinds of the particles was injected into the reactor chamber. The dust particles were illuminated by a laser of 532 nm in wavelength. The RF voltage (peak to peak) was changed from 50 to 150 V. The dust particles were observed by the CCD camera in the experiments.

### 7.3.2 Results

Figure 7.24 shows photographs of dust particles observed at RF voltages of 50, 100 and 150 V in Ar RF plasmas. Field of view of the photographs was right half of the chamber. Left edge of the photograph is the radial centre of the chamber.

At low RF voltage of 50 V, the dust particles levitated around the centre of the plasma and they were separated to two layers in vertical direction: the larger dust particles levitated in the lower layer, and the smaller ones levitated in the upper layer. When the RF voltage reached 100 V, the larger particles were repelled to outside while the smaller particles remained around the centre. Both particle clouds have extended horizontally. At 150 V, the larger particles moved outward further, while the smaller ones were repelled from the centre and remained inside of the larger particle cloud. The cloud of the dust particles clearly showed two segments of the smaller and larger ones as a horizontal size distribution.

Spatial distributions of ion density were measured by the double-probe method at RF voltage of 50, 100 and 150 V.[11, 15] In Fig. 7.25 measured values were plotted by markers as function of height from the bottom electrode. Lines are fitting curves as mentioned later. For all the three spatial distributions of ion density, the peak positions of ion density were not at the centre between two electrodes but at

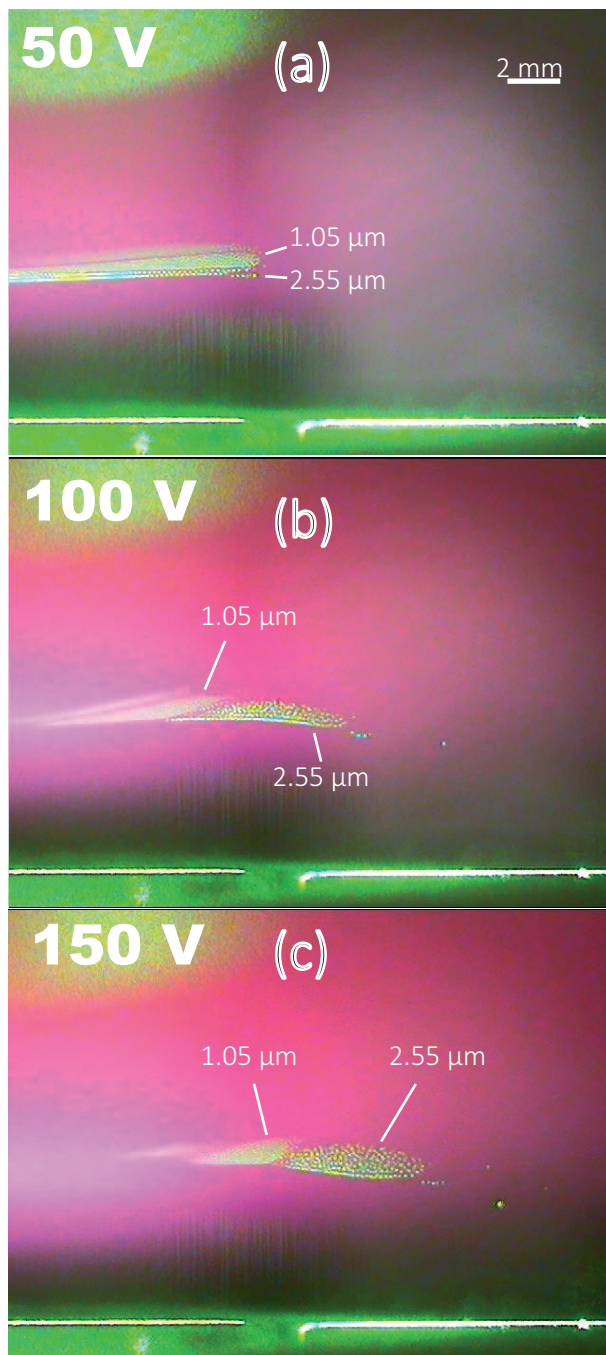


Figure 7.24: Segmentation of dust particles at RF voltages of 50, 100 and 150 V. Left side is the centre of chamber, and right side is the boundary.

around plasma-sheath boundary near the powered electrode. The ion density and its gradient were increased while the RF voltage increased from 50 to 150 V.

### 7.3.3 Discussion

The segmentation of dust particles in horizontal direction was observed and spatial distribution of ion density in vertical direction was measured. In order to analyze forces acting on the dust particles, a spatial distribution of ion density was calculated by the fluid model. Figure 7.26 shows the 2-dimensional spatial distribution of ion density at gas pressure of 80 Pa, and RF voltages of 50, 100 and 150 V. We can plot the ion density at Radial=0 as an 1-dimensional spatial distribution in vertical direction of the centre of the reactor. This curve can be fitted to the measured ion density on the Fig. 7.25. Markers are the measured ion densities and lines are the fitted value.

Once the spatial distribution of ion density is fitted, the ion flux can be calculated by  $\mathbf{\Gamma} = -D_a \nabla n$ . Ambipolar electric field can be calculated by  $\mathbf{E} = -\frac{k_B T_e}{e} \frac{1}{n} \nabla n$ .

Charge of the dust particles and floating potential are necessary to analyze the ion drag and electrostatic forces. At a steady state on the dust particles, the ion and electron currents represented by  $I_i$  and  $I_e$ , respectively, should be equal,  $I_e = I_i$ . [5] By taking the orbital-motion-limited (OML) theory, the electron and ion currents are expressed as

$$I_e = e\pi r_p^2 n_e \left[ \frac{8k_B T_e}{\pi m_e} \right]^{\frac{1}{2}} \exp\left[ \frac{eV_{pf}}{k_B T_e} \right], \quad (7.1)$$

$$I_i = e\pi r_p^2 n_i \left[ \frac{8k_B T_i}{\pi m_i} \right]^{\frac{1}{2}} \left[ 1 - \frac{eV_{pf}}{k_B T_i} \right]. \quad (7.2)$$

Here,  $r_p$ ,  $n_e$ ,  $n_i$ ,  $m_e$ , and  $m_i$  are radius of the dust particle, electron and ion densities, electron and ion masses, respectively. The  $V_{pf}$  is floating potential, and the  $T_i$  is the ion temperature with is considered to be the ambience temperature of 300 K. The charge of the dust particle is given by

$$Q_p = V_{pf} 4\pi\epsilon_0 r_p \left( 1 + \frac{r_p}{\lambda_D} \right). \quad (7.3)$$

Here  $\epsilon_0$  and  $\lambda_D$  are vacuum permittivity and Debye length, respectively.

The ion drag force is caused by momentum transfer from ions to the dust particles. [5] It consists of collection and orbit forces. The collection force is expressed by

$$\mathbf{F}_{id}^{col} = n_i \mathbf{v}_i \pi b_c^2 m_i v_s, \quad (7.4)$$

where  $\mathbf{v}_i$  is drift speed of ion. The  $n_i \mathbf{v}_i$  is the ion flux which is given by  $n_i \mathbf{v}_i = \mathbf{\Gamma}_i = -D_a \nabla n_i$ . The  $v_s = \left( \frac{8k_B T}{\pi m_i} + v_i^2 \right)^{\frac{1}{2}}$  is mean speed of the ion. [5]  $b_c$  is the collection radius given by the OML theory,

$$b_c^2 = r_p^2 \left( 1 - \frac{2eV_{pf}}{m_i v_s^2} \right). \quad (7.5)$$

The orbit force is

$$\mathbf{F}_{id}^{orb} = n_i \mathbf{v}_i \sigma^{orb} m_i v_s, \quad (7.6)$$

where  $\sigma^{orb}$  is the orbit cross-section defined by

$$\sigma^{orb} = 2\pi b_{\pi/2}^2 \ln\left( \frac{\lambda_D^2 + b_{\pi/2}^2}{b_c^2 + b_{\pi/2}^2} \right). \quad (7.7)$$

The  $b_{\pi/2}$  is an impact parameter for asymptotic orbit angle of  $\pi/2$ .

$$b_{\pi/2} = \frac{eQ_p}{4\pi\epsilon_0 m_i v_s^2}. \quad (7.8)$$

The electrostatic force,  $\mathbf{F}_E$  is expressed by the ambipolar electric field and the charge of dust particle,

$$\mathbf{F}_E = Q_p \mathbf{E}. \quad (7.9)$$

The resultant force of the ion drag and the electrostatic force is

$$\mathbf{F}_{\text{res}} = \mathbf{F}_{\text{id}}^{\text{col}} + \mathbf{F}_{\text{id}}^{\text{orb}} + \mathbf{F}_E. \quad (7.10)$$

Both of ion drag and electrostatic force depend on the gradient of ion density and dust particle size. Ion drag force  $\mathbf{F}_{\text{id}} \propto r_p^2 \nabla n$  and electrostatic force  $\mathbf{F}_E \propto r_p \nabla n/n$ . Ion drag force is more sensitive to the dust particle size. Increase of RF voltage causes increases of ion density and its gradient. It leads that the ion drag force is affected by RF voltage more than the electrostatic force. Those two aspects lead different equilibrium position for different dust particle size in a plasma and a possibility of the equilibrium position regulated by discharge condition.

Figure 7.29 shows ion drag and electrostatic forces in the radial (horizontal) direction. The positive sign of force indicates the force directing from the centre to outward and the negative sign indicates the opposite. At lower RF voltage of 50 V, inward electrostatic force is dominant for both two size dust particles of 1.05 and 2.25  $\mu\text{m}$ , and dust particles remain at the centre of the chamber. At RF voltage of 100 V, increase of ion density and leads to increase of ion drag and electrostatic forces, however we see a different aspect of the dependence on the dust particle size compared with 50 V. For smaller dust particle of 1.05  $\mu\text{m}$ , electrostatic force is still higher than ion drag force through whole radial. For larger dust particle of 2.25  $\mu\text{m}$ , near the ion centre of the chamber, the drag force is higher than the electrostatic one. There is an equilibrium point at Radial=16.5 mm for the larger dust particles. The larger dust particles are repelled at this position while the smaller dust particles remain in the centre of chamber. At RF voltage of 150 V, the smaller dust particles have a equilibrium position at Radial=15 mm, and the larger dust particles have a equilibrium position at Radial=18 mm. The evaluation of dust particle positions and segmentation behaviours agree with the experimental observations.

### 7.3.4 Conclusion

In the experiments, segmentations of dust particles in their sizes were observed at different RF voltage. Segmentation manner can be controlled by regulating discharge condition. In analysis, ambipolar diffusion in the bulk of plasmas was considered to be a main driving force for the segmentation. Spatial distributions of ion density were fitted by the numerical model. Ion flux and ambipolar electric field caused the ion drag and electrostatic forces. The equilibrium positions for different sized dust particles at different discharge voltage were calculated and they had good agreement with observation in the experiment. This gives a possibility for an application of classification of dust particle in their sizes. By controlling the levitating position of dust particles, separating one sized dust particles from other sized, and a spatial distribution of the dust particles can be obtained.

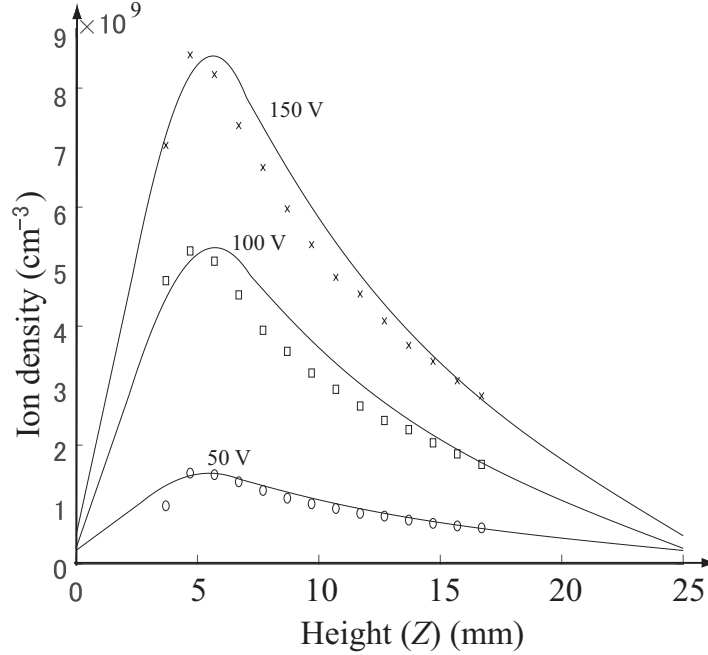


Figure 7.25: The 1-dimensional spatial distributions of ion density in vertical direction at the centre of chamber. Markers represent measured data by double-probe method and curves are fitted by the fluid model.

## 7.4 Classification of particles in their size

The segmentation of particles in their size in the bulk of dusty plasmas is discussed in the previous section. This section focus on the transport of two size particles through the plasma sheath. In order to investigate the sheath structure and its effects on the transport of dust particles, the ion flow is preferable to be negligible. To do so, configuration of the discharge chamber is modified, and the powered electrode is set at the upper side. According to the diagnostic and calculation in the previous section, the strong ionisation area appears near the upper side powered electrode. Near the bottom grounded electrode, where particles levitate, both ion drag and electric force in the bulk of plasma are much smaller compared to the electric force in the plasma sheath.

According to the OML theory[5] in the plasma, the charge depends on the radius of the dust particles  $r_p$ , the ratio of electron temperature to ion one  $T_e/T_i$ , and that of electron mass and ion one  $m_e/m_i$ . The negative charge enables the dust particle to levitate near the plasma-sheath boundary by forces such as gravitational, electrostatic and so on.[7, 20]

In this work, the main goal is to control the transport of dust particles in order to separate them depending on their sizes in RF capacitively-coupled plasmas. Pulse-time modulation is applied to the RF fundamental signal. Measurements with a double-probe method show that the pulse-time can significantly influence the electron temperature which is hard to be changed by regulation of the RF voltage. Variation of the electron temperature enables the dust particles with mono-dispersed size distribution to be transported through the sheath of plasmas. This effect is discussed in this section.

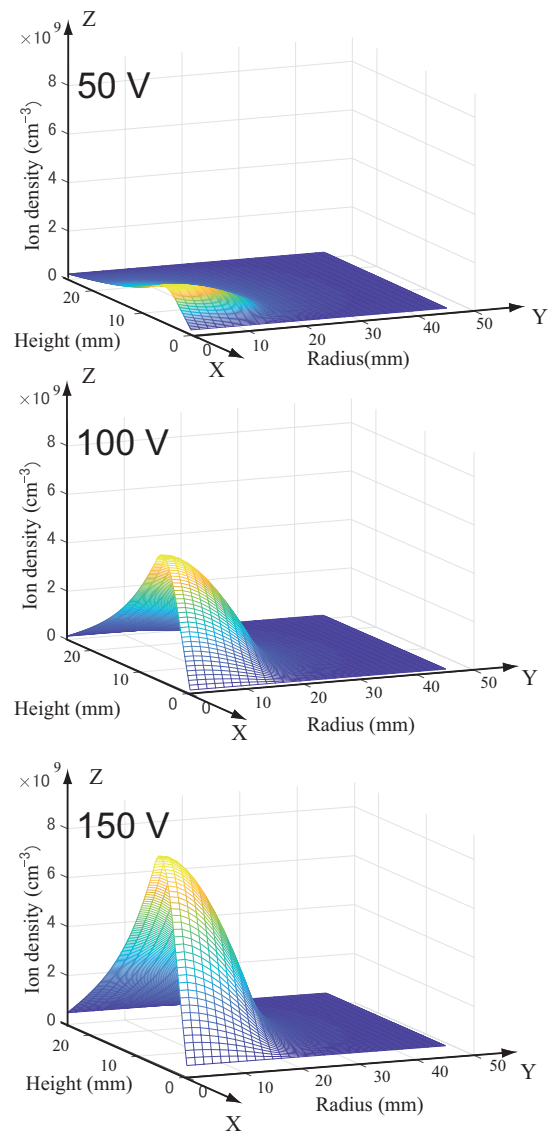


Figure 7.26: The 2-dimensional spatial distribution of ion density calculated by the fluid model, at RF voltages of 50, 100 and 150 V.

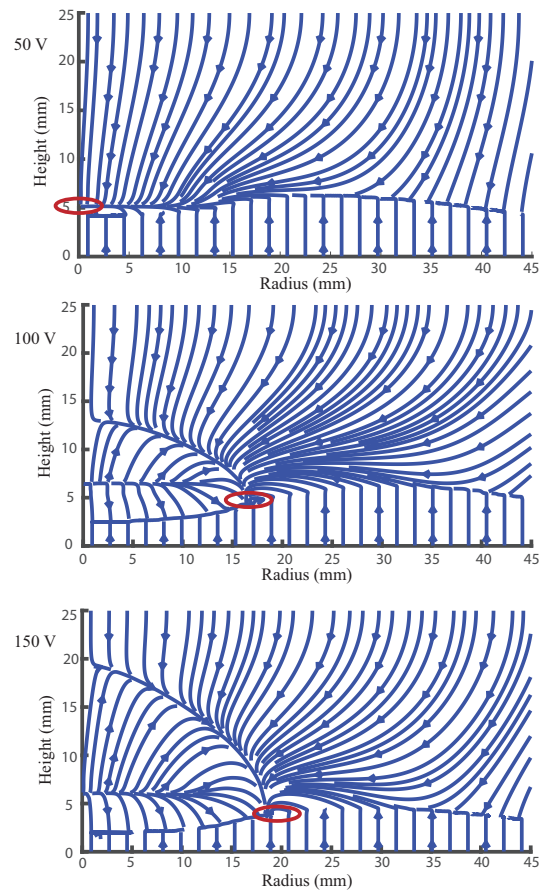


Figure 7.27: Resultant force stream on the particles of  $d = 2.25 \mu\text{m}$  for RF voltage 50, 100 and 150 V. Red cycle indicates the balanced position.

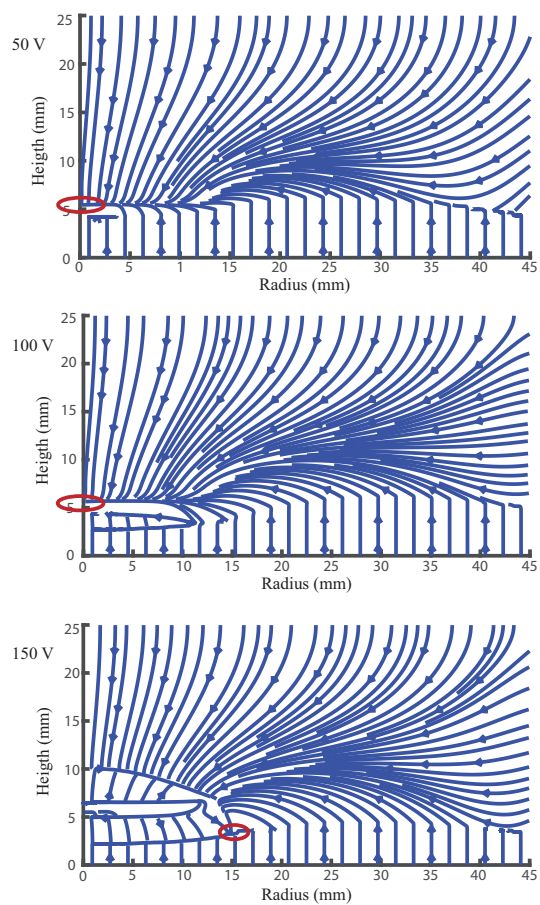


Figure 7.28: Resultant force stream on the particles of  $d = 1.05 \mu\text{m}$  for RF voltage 50, 100 and 150 V. Red cycle indicates the balanced position.

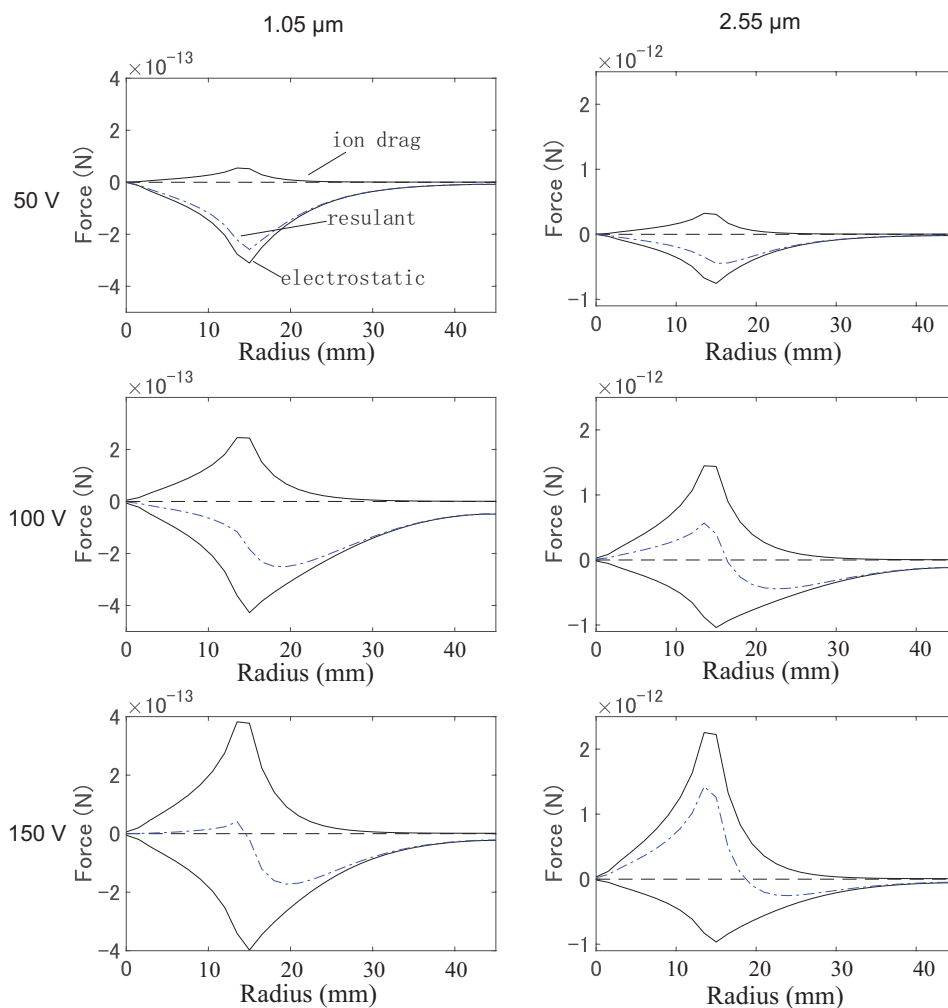


Figure 7.29: Ion drag, electrostatic and resultant forces at RF voltages of 50, 100 and 150 V for the dust particles of 1.05  $\mu\text{m}$  and 2.25  $\mu\text{m}$ . The positive sign of force represents the outward direction. Ion drag and electrostatic forces are represented by solid lines, positive one is the ion drag force and the negative one is the electrostatic force. Resultant force is represented by broken line. The point where the resultant force equals to 0 is the equilibrium position.

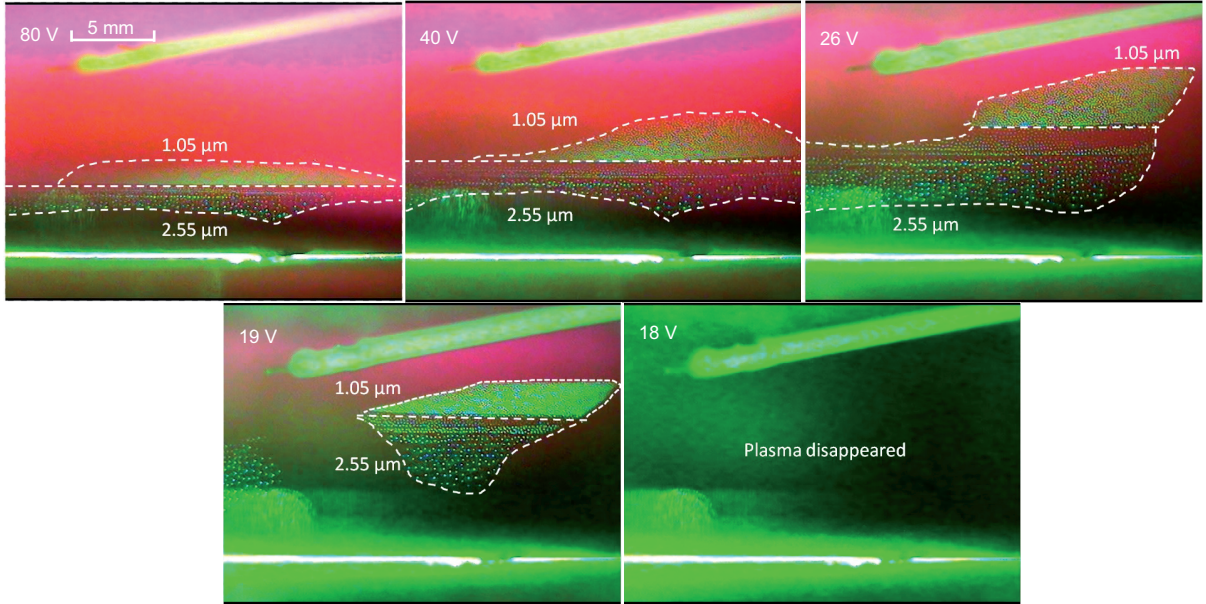


Figure 7.30: Particles in the plasma decreasing RF voltage from 80 V to 18 V.

#### 7.4.1 Experimental

The PK-3 plus chamber was used with the powered electrode set at the upper side. The bottom electrode was grounded and it consists of two parts: a disk set at the centre and a ring surrounding the disk. Both of them were grounded. Between the disk and the ring, a gap of 2 mm was formed. Argon gas was fed into the chamber for discharge. The pressure of the gas was set at 200 mtorr (26 Pa). The MF particles of 2.55  $\mu\text{m}$  in diameter, and  $\text{SiO}_2$  particles of 1.05  $\mu\text{m}$  in diameter, were injected by two dispensers mounted on the top of the chamber. In experiments, the RF voltage was varied from 80 V to 18 V, modulation frequency was set at 10 kHz, and modulation duty cycle was changed from 100% (100% duty means without modulation) to 20%.

#### 7.4.2 Results and Discussion

Three experiments to observe particle behaviours were performed (noted as Exp1, Exp2, Exp3). In each case, two sizes of particles (1.05  $\mu\text{m}$  and 2.55  $\mu\text{m}$  in diameter) were identically injected to the plasma. For the first experiment Exp1, the RF voltage was changed from 80 V to 18 V without

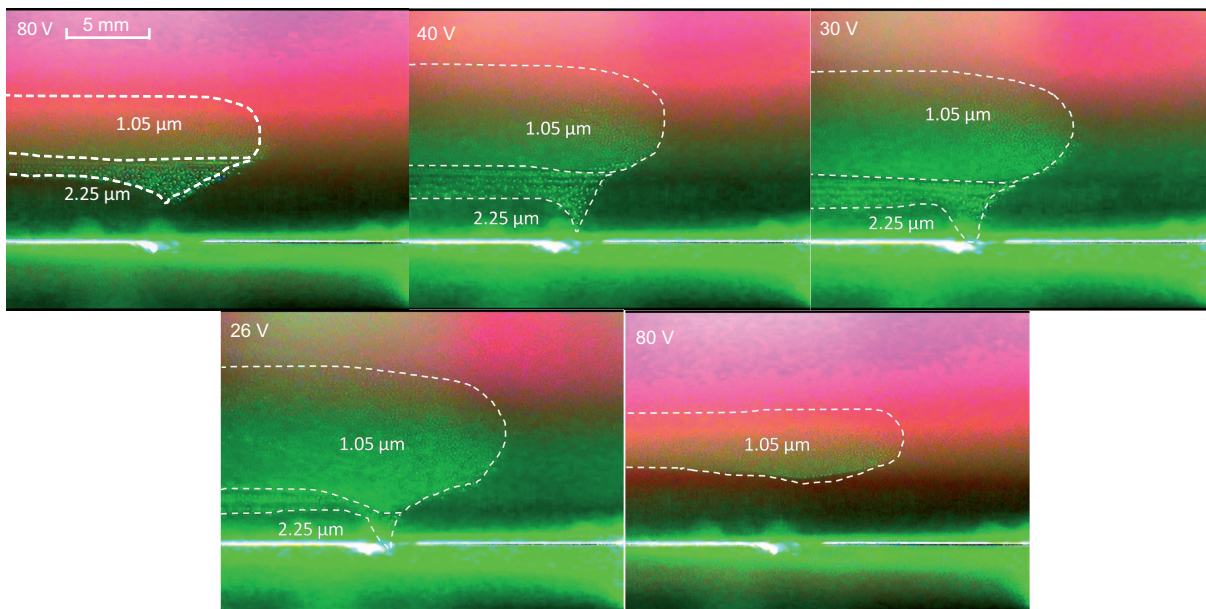


Figure 7.31: Particles in the plasma decreasing RF from 80 V to 26 V, and then returning to 80 V with a RF power modulation of 10 kHz in frequency and 30% of duty cycle.

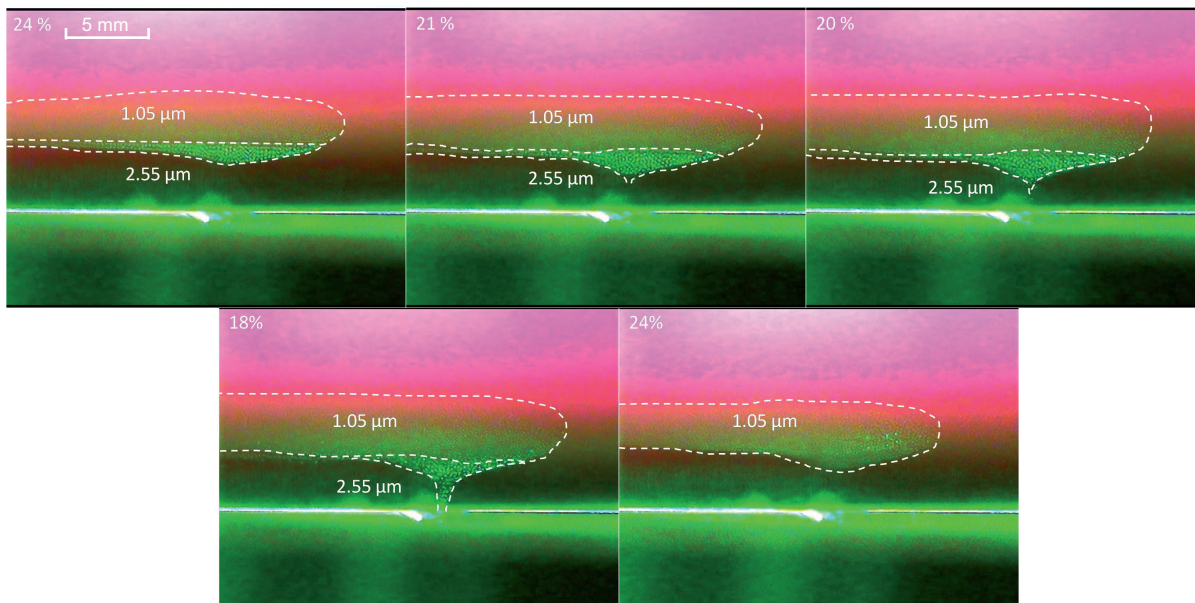


Figure 7.32: Particles in the plasma decreasing modulation duty cycle from 24% to 18%, and then returning to 24% with a RF power modulation of 10 kHz while RF voltage was set at 80 V.

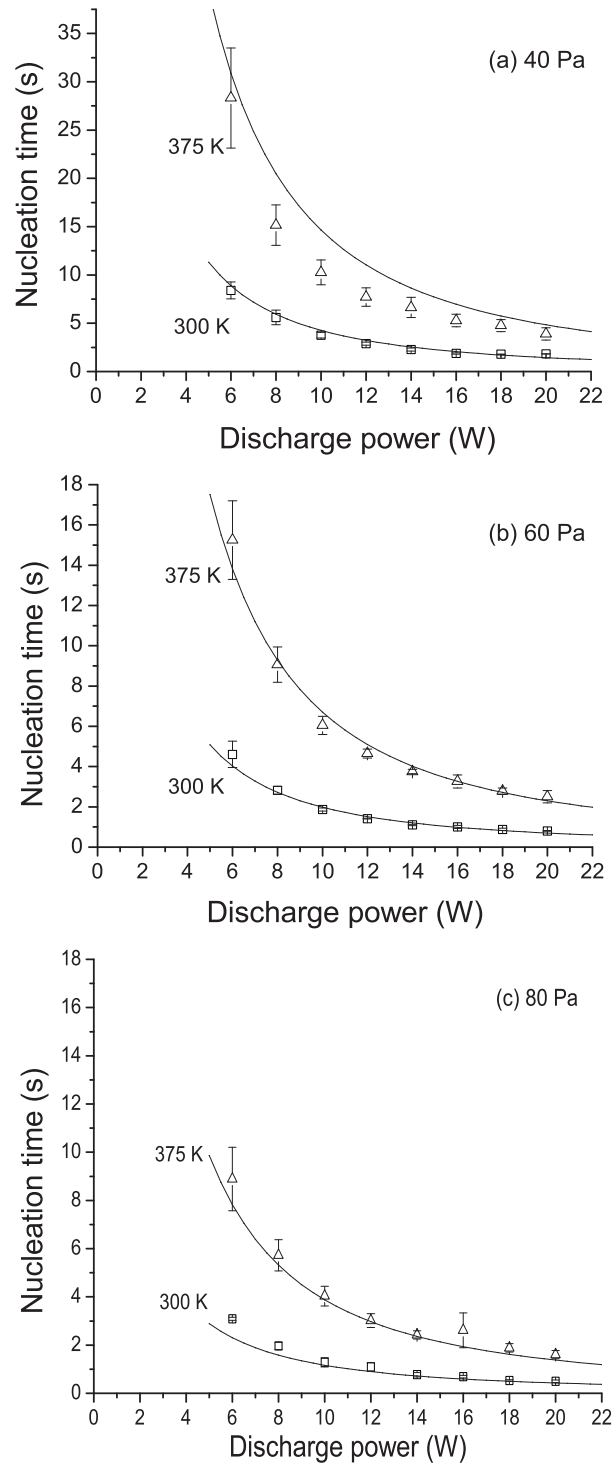


Figure 7.33: (a) Electron temperatures as functions of RF voltage with and without modulation. (b) Ion densities as functions of RF voltage with and without RF modulation. The frequency and duty cycle for modulation were 10 kHz and 30%, respectively.

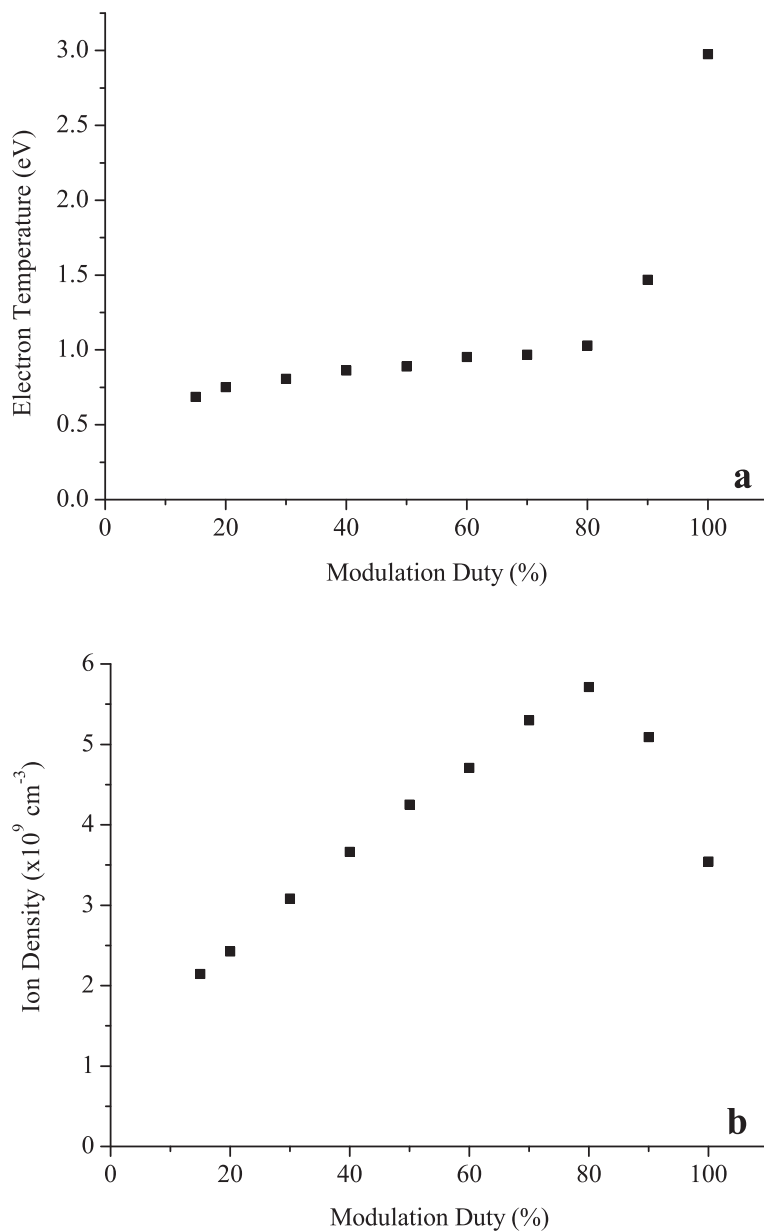


Figure 7.34: (a) Electron temperatures as functions of modulation duty cycle. (b) Ion densities of functions of modulation duty cycle. The frequency and RF voltage were 10 kHz and 100 V, respectively.

applying modulation signal. For the second experiment Exp2, the RF voltage was changed from 80 V to 26 V by applying a modulation signal of 10 kHz in frequency and 30% in duty cycle. For the third experiment Exp3, the RF voltage was set at 80 V, a modulation signal of 10 kHz in frequency was applied, and the modulation duty cycle was changed from 24% to 18%. Particles behaviours in the three experiments were shown in Fig. 7.30, Fig. 7.31 and Fig. 7.32, respectively. We can see that in each case two sizes of particles were initially levitated in the plasmas and they were separating in two layers: larger particles were levitating in lower layer and smaller particles were in upper layer.[21] In the case of Exp1, without modulation (Fig. 7.30), particles remained levitated in the plasma during decrease of RF voltage from 80 V to 18 V. The RF voltage at 19 V was too low, and both of two sizes of particles fell down at the same time. In the case of Exp2 (Fig. 7.31), levitating position of particles changed during decrease of RF voltage form 80 V to 40 V, and the larger-size particles started to fall down when the RF voltage decreased to 30 V. When the RF voltage decreased to 26 V, all the larger-size particles fell down and small-size particles only remained in the plasma. When the RF voltage returned to 80 V, there were only small-size particles levitating in the plasma. In the case of Exp3 (Fig. 7.32), the larger-size particles started to fall down when the modulation duty cycle decreased to 18 %. In a few 10 s , the larger-size particles were completely fallen, however the smaller particles still remained in the plasma. Then, the modulation duty cycle returned to 24 %, there were small-size particles only levitating in the plasma.

Electron temperature and ion density in the experiments were measured by the double-probe method[15] at the sheath edge. Figures 7.33 (a) and (b) show electron temperature and ion density as functions of RF power with and without modulation, respectively. The electron temperature was not influenced by the RF voltage, however it was strongly affected by the RF power modulation. It dropped from 4 eV (without modulation) to 1 eV (with modulation). The ion density increased with increase of the RF voltage. However, the ion density slightly decreased with adding the RF power modulation. In the Exp2, the electron temperature decreased with the modulation, resulting in falling down of larger particles. Figure 7.34 shows the electron temperature and the ion density as functions of modulation duty cycle while the RF voltage was set at 80 V.

The measurements of electron temperature and ion density were performed without the particles. It was found in a previous work[11] with the same chamber that the presence of the particles does not give much influence to the electron temperature and ion density at the sheath edge. In this work, those values were used as a boundary condition in calculations.

The particle behaviours in plasmas can be explained by an equilibrium between electrostatic force at the edge of the plasma sheath and gravity force on the particles.[7, 8, 9] Electrostatic force is depending on the charge number of the particles and the electric field of the sheath. The orbit-motion-limit(OML) model gives a solution of particle charge in plasmas.[9, 6] Sheath structure can be calculated by introducing Bohm criterion and Child-Langmuir law.[22, 23]

As discussed in Chapter 6, the potential, electric field and ion density in the plasma sheath can be expressed as

$$V(z) = -\sqrt{\frac{8J_1}{9\epsilon_0\mu_i}}(D-z)^{\frac{3}{2}}, \quad (7.11)$$

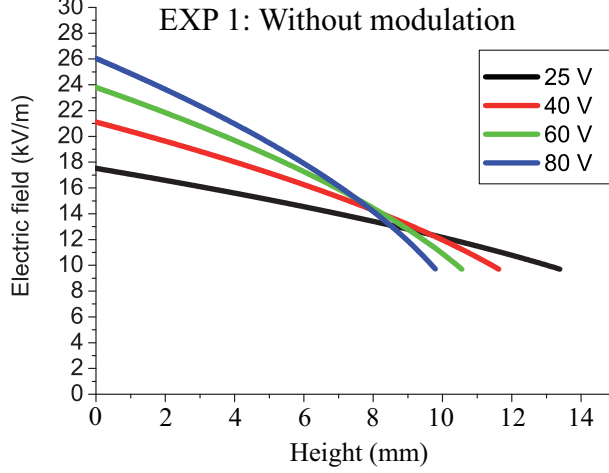


Figure 7.35: Electric field in function of height during the Exp1. Dependency of the electric field on the RF voltage is investigated without pulse-time modulation. The RF voltage is set at 25, 40, 60 80 V.

$$E(z) = -\frac{\partial V(z)}{\partial z} = \sqrt{\frac{2J_i}{\epsilon_0\mu_i}}(D-z)^{\frac{1}{2}} \quad (7.12)$$

and

$$n_i(z) = \frac{\epsilon_0}{e} \frac{\partial E(z)}{\partial z} = \frac{\epsilon_0}{2e} \sqrt{\frac{2J_i}{\epsilon_0\mu_i}}(D-z)^{-\frac{1}{2}}, \quad (7.13)$$

with

$$D = \left(\frac{ev_B^2}{2J_i\mu_i}\right)^{\frac{3}{2}} + \frac{1}{2} \ln\left(\frac{m_i}{2\pi m_e}\right) \left(\frac{8J_i}{9\epsilon_0\mu_i}\right)^{-\frac{1}{2}} \frac{k_B T_e}{e}^{\frac{2}{3}}. \quad (7.14)$$

The sheath length is  $S = D - \frac{ev_B^2}{2J_i\mu_i}$ .

Particle charge in sheath can be resolved by the equations discussed in Chapter 6, by taking the calculated sheath structure and measured electron temperature, ion density at the boundary of sheath edge. Equations of electron and ion flows are

$$\Gamma_e = \pi r_p^2 n_e \left[\frac{8k_B T_e}{\pi m_e}\right]^{\frac{1}{2}} \exp\left[\frac{e(V_f - V(z) + V(z) - V_p)}{k_B T_e}\right] \quad (7.15)$$

and

$$\Gamma_i = \pi r_p^2 n_i(z) u_i(z) \left[1 - \frac{e(V_f - V(z))}{\frac{1}{2} m_i u_i^2}\right], \quad (7.16)$$

with

$$Q = (V_f - V_p) 4\pi\epsilon_0 r_p. \quad (7.17)$$

The electric field and particle charge in the sheath are calculated for each condition of the 3 experiments. The results are shown in Figs. 7.35, 7.36, 7.37. The decrease RF voltage increases the sheath length and decreases the electric field in the sheath. Compare Fig. 7.35 and 7.36, the pulse-time modulation reduce both the sheath length and electric field in the sheath. Figure 7.37 shows the decrease of duty cycle decreases the electric field in the sheath.

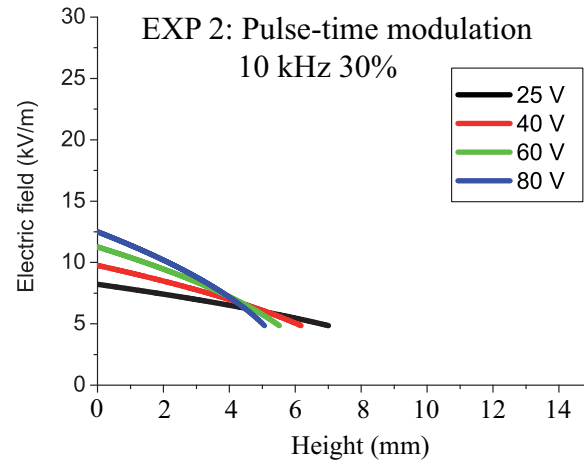


Figure 7.36: Electric field in function of height during the Exp2. Dependency of the electric field on the RF voltage is investigated by applying pulse-time modulation with frequency 10 kHz and duty cycle 30%. The RF voltage is set at 25, 40, 60 80 V.

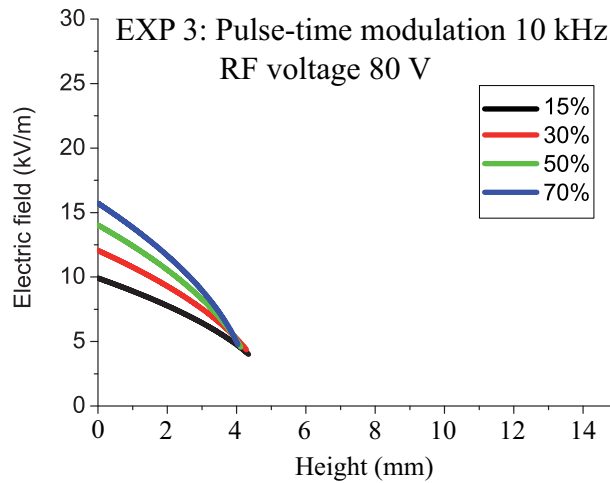


Figure 7.37: Electric field in function of height during the Exp3. Dependency of the electric field on the duty cycle of the pulse-time modulation is investigated. The RF voltage is set at 80 V, modulation frequency is set at 10 kHz, modulation duty cycle is set at 15%, 30%, 50%, 70%.

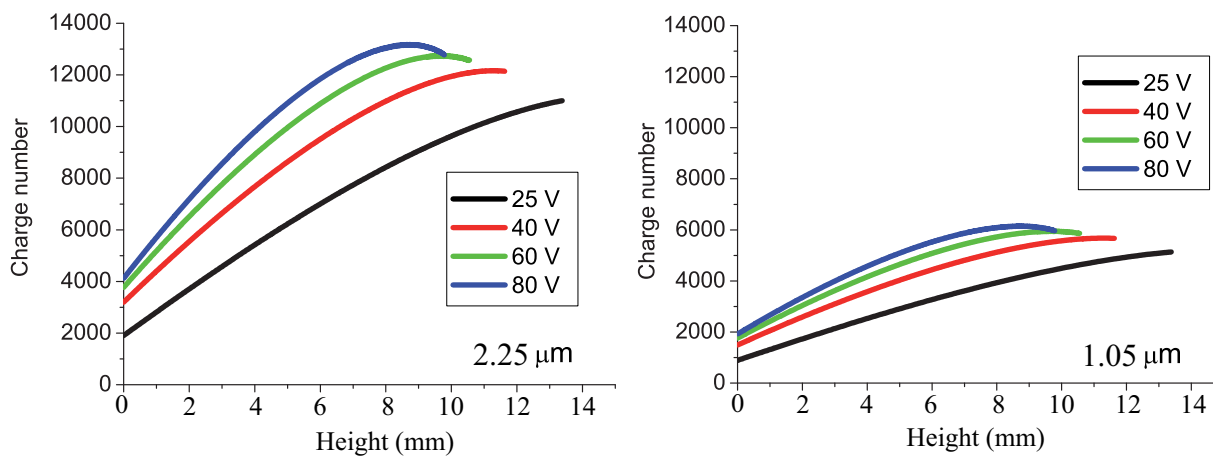


Figure 7.38: Charge number of two size particles in function of height during the Exp1. Dependency of the Charge number in the sheath on the RF voltage is investigated without pulse-time modulation. The RF voltage is set at 25, 40, 60 80 V.

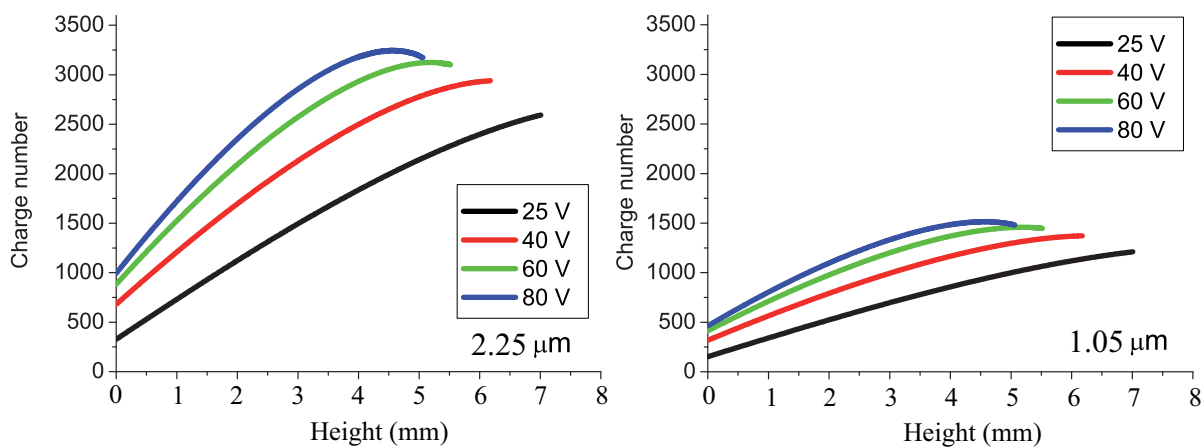


Figure 7.39: Charge number of two size particles in function of height during the Exp2. Dependency of the Charge number in the sheath on the RF voltage is investigated by applying pulse-time modulation with frequency 10 kHz and duty cycle 30%. The RF voltage is set at 25, 40, 60 80 V.

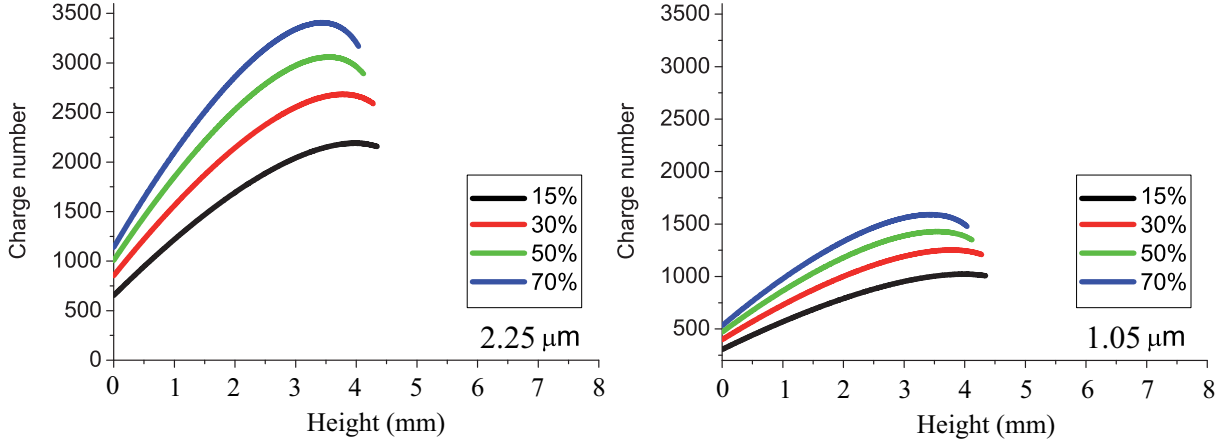


Figure 7.40: Charge number of two size particles in function of height during the Exp3. Dependency of the charge number in the sheath on the duty cycle of the pulse-time modulation is investigated. The RF voltage is set at 80 V, modulation frequency is set at 10 kHz, modulation duty cycle is set at 15%, 30%, 50%, 70%.

Figures 7.38, 7.39 and 7.40 show the results of particle charge in function of distance to the bottom electrode for the particles of two sizes, in each condition of the 3 experiments. Particles get less charge when they are closer to the grounded bottom electrode which is treated as the wall in the calculation. Both the decrease of RF voltage and duty cycle of the pulse-time modulation can lead the decrease of the charge of particles.

Electrical field increases and the particle charge decreases with getting closer to the lower grounded electrode, caused by electron depletion.[9] The electrostatic forces on the particles, calculated by  $F(z) = E(z)Q(z)$ , are shown as functions of height from the electrode in Fig. 7.41. There are maximum points of electrostatic forces in the middle of the sheath edge and the lower grounded electrode. Whether the particles can levitate or not depends on the balance of gravitational force and the maximum electrostatic force. While the maximum electrostatic force is larger than the gravitational force, the particles can levitate at a position higher than the maximum point of electrostatic force. In the calculation, when the ion density decreases, the sheath width increases however the electrostatic force decreases. When the electron temperature decreases, the sheath width decreases too and the electrostatic force decreases. The position of the particles can be changed by the plasma parameters.

The electrostatic force acting on the particles in the sheath were calculated by introducing the electron temperature and ion density measured by the double-probe[15]. The maximum electrostatic forces ( $F_e$ ) in the experiment conditions were extracted and plotted to compare with the gravitational forces ( $F_g$ ) on the particles. (Figs. 7.42 and 7.43)

In the Exp3, RF voltage was fixed at 80 V and modulated at 10 kHz, and the electrostatic forces ( $F_e$ ) decrease with decreasing the modulation duty cycle (Fig. 7.42). When the modulation duty cycle was decreased to 15%, the maximum electrostatic force for the larger particles became weaker than the gravitational force, while the electrostatic force acting on the smaller particles was still stronger

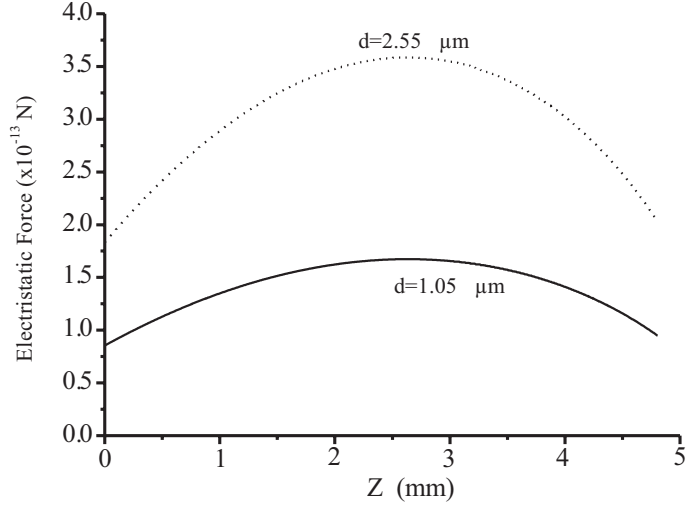


Figure 7.41: Electrostatic forces on particles of  $2.55 \mu\text{m}$  in diameter (dotted curve) and  $1.05 \mu\text{m}$  (solid curve) in the sheath, calculated from the plasma parameters of  $T_e=1.08 \text{ eV}$  and  $n_i=3 \times 10^9 \text{ cm}^{-3}$ .

than the gravitational force. Thus, at 15% of the modulation duty cycle, the larger particles fell down and the smaller particles remained trapped in the plasma.

In the Exp1 and Exp2, maximum electrostatic forces in the sheath were extracted as functions of RF voltage, with parameters of electron temperature corresponding to the modulation duty cycle (Fig. 7.43). Solid circles and rectangles, are for the Exp1, without modulation. Open marks are for the Exp2, applied modulation at 10 kHz, 30% of the duty cycle fixed. Decrease of RF voltage caused slight decrease of electrostatic force acting on the particles in the sheath. Without modulation, the decrease of the RF voltage was not enough to break the balance of the electrostatic and gravitational forces. That is why in Exp1, we could not drop the larger particles from the plasma without turning off the plasma by extremely reducing the RF voltage. For the Exp2, tendency of the electrostatic force as function of RF voltage was similar to that of the Exp1, however, the force was 10 times smaller than that of the Exp1 due to modulation. In this case, the maximum electrostatic force acting on the larger particles became weaker than the gravitational force by decreasing the RF voltage, and the larger particles fell down and the smaller particles only remained in the plasma.

### 7.4.3 Conclusion

RF power modulation and RF voltage regulation were applied to low temperature RF dusty plasmas containing two sizes of particles. The particles behaviours were observed by laser light scattering. By applying modulation and changing modulation duty cycle, particle transport was controlled: position of the particle descended slowly and the larger particles started to fall down for a given value of the duty cycle. Ion density and electron temperature in the experiments were measured by a double-probe method. Calculations of the plasma sheath were combined with the Child-Langmuir law and ambipolar diffusion. This combination gave reasonable spatial distribution of the ion density around

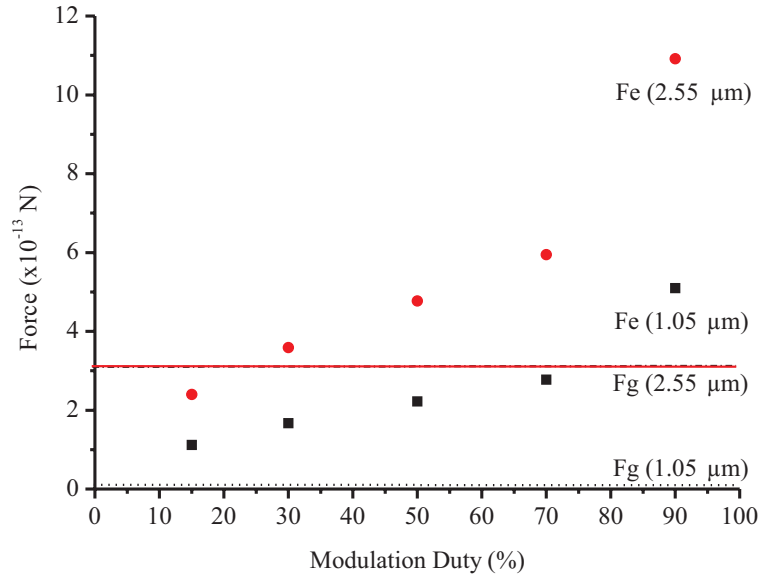


Figure 7.42: Electrostatic forces in the sheath for particles of 2.55  $\mu\text{m}$  in diameter (red circle) and 1.05  $\mu\text{m}$  (black rectangle) in changing modulation duty cycle from 90% to 15%. Two dotted straight lines show gravitational forces on particles of 2.55 and 1.05  $\mu\text{m}$  in diameter.

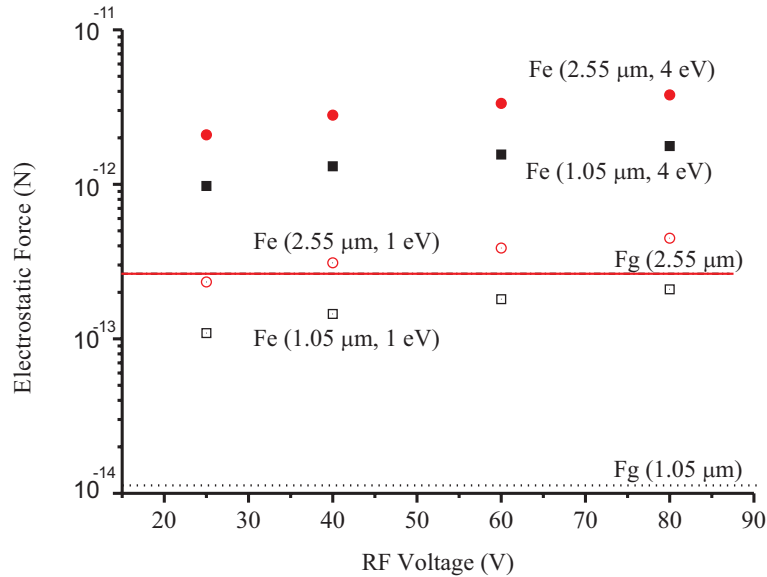


Figure 7.43: Electrostatic forces in the sheath for particles of 2.55  $\mu\text{m}$  in diameter (red circle) and 1.05  $\mu\text{m}$  (black rectangle) in changing RF voltage from 80 V to 25 V in the case with and without modulation. Solid marks show the case without modulation, where electron temperature remained around 4 eV in the experiments. Open marks show the case with modulation at 10 kHz in frequency 30% in duty cycle, where electron temperature remained around 1 eV. Two dotted lines show gravitational forces for the particles of 2.55 and 1.05  $\mu\text{m}$  in diameter.

the sheath edge, compared with the Child-Langmuir law only, which usually takes a boundary condition of  $E(S) = 0$  and causes the ion density to be infinity at the sheath edge. The orbital-motion-limited model was applied to calculate the mean charge of the particles in the sheath. Finally, the electrostatic forces acting on the particles were obtained in the calculations. As the result, decreasing of RF voltage and modulation duty cycle can decrease the electrostatic forces. Applying modulation and decreasing the modulation duty cycle, the electrostatic force could be significantly decreased. By operating the RF voltage and the modulation duty cycle, one can regulate the electrostatic force acting on the particles in the plasma sheath.

## 7.5 Conclusion

Transport behaviours of dust particles in complex plasmas are studied in this chapter. Dust particles are negatively charged in the plasmas and acted by gravitational, electric and ion drag forces. Dust particles levitate at the position where the forces get balance. The electric force confines the dust particles inside the plasmas, and the ion drag force repel them outward. The electric force is due to the charge of dust particles and the electric field. The ion drag force is due to the ion flux and the cross section of the dust particles. In the bulk of the plasmas, the electric field and the ion flux are created by ambipolar diffusion. In the plasma sheath, the electric field and ion flux are due to the electron depletion. The charge of dust particles increases with the increase of the electron temperature. The ion flux and electric field in the bulk of the plasmas increases with the increase of the gradient of the ion density. While the gradient remains the same, the electric field in the bulk of the plasmas increase with the decrease of the ion density.

The observations of this chapter make clear that in our experiment setup,

- 1) increasing RF voltage leads the dust particles transport outward,
- 2) applying the pulse-time modulation and decreasing the duty cycle leads the dust particles convert above the edge of the electrode,
- 3) decreasing the duty cycle infer then a critical value can drop gradually dust particles onto a specific area,
- 4) when there are dust particles of multiple sizes, the dust particles of larger size are more influenced by the ion drag force, and the particles can be separated in segments by their size due to the difference of the balanced position of forces,
- 5) when there are dust particles of multiple sizes, decreasing the duty cycle can drop gradually the dust particles by the larger size.

The diagnostics of plasma parameters make clear that,

- a) increasing RF voltage leads the increase of ion density and its gradient,
- b) the regulation of RF voltage dose not influence to the electron temperature,
- c) pulse-time modulation leads the decrease of the electron temperature.

For the general conclusion, we have,

- $\alpha$ ) the gradient of ion density creating ion flux repel dust particles,
- $\beta$ ) higher the electron temperature, higher the competence to confine the dust particles,
- $\gamma$ ) the inhomogeneity of the ion density is the cause of the segmentation of the dust particles in their size.

Though the results and the conclusions, the control of the transport of the dust particles in the RF plasmas is realised.

## 7.6 French summery

Les principaux résultats de nos recherches sur le comportement et le transport des particules dans le plasma sont présentés dans ce chapitre. Les particules avec des tailles bien connues sont utilisées. Un diagnostic de la décharge RF est premièrement effectué pour voir comment les paramètres plasma (température électronique et densité ionique principalement) réagissent en fonction des modifications des conditions de la décharge. Ensuite, l'influence de la présence des particules sur les paramètres plasma est examinée. Les mesures par la double sonde de Langmuir dans les cas avec et sans la présence des particules montrent que la petite quantité de particules, que nous mettons en œuvre dans nos expériences, n'induit pas une influence importante sur le plasma outre la perturbation locale. Les particules avec une distribution de taille mono-dispersée sont observées dans le plasma en faisant varier la tension et la modulation de la puissance RF. Les positions de lévitation, de transport et de dépiégeage des particules sont observés. La dépendance des comportements en fonction des tailles de particules est ensuite étudiée en injectant des particules de deux tailles différentes dans le plasma. La segmentation des particules et les différentes conditions de dépiégeage fonction de la taille sont observés. Cela ouvre une possibilité de classifier les particules par leur taille. Ce mécanisme est expliqué par les forces agissant sur les particules. Les particules chargées négativement dans le plasma sont à la fois poussées par le flux des ions et la force gravitationnelle et confinées par le champ électrique dans la gaine. Les flux des ions dans le corps plasma sont dus à la diffusion ambipolaire qui dépend du gradient de la densité plasma locale. L'augmentation de tension de la décharge augmente à la fois la densité et son gradient spatial, la force de poussée des ions est ainsi renforcée et les particules sont repoussées vers l'extérieur. La diminution de la température électronique réduit à la fois le champ électrique et la charge des particules, et par conséquent, la force de confinement des particules diminue. En jouant sur les deux paramètres, les forces sur les particules peuvent être contrôlées et par conséquent leur transport. Ayant différents points d'équilibre, les particules de tailles différentes peuvent être séparées les unes des autres.



# Bibliography

- [1] G. S. Selwyn, J. E. Heidenreich, and K. L. Haller, *Appl. Phys. Lett.* **57**, 1876 (1990).
- [2] S. J. Choi and M. J. Kushner, *J. Appl. Phys.* **74**, 853 (1993).
- [3] M. Lennox and S. Coulombe, *J. Nanopart. Res.* **14**, 1245 (2012).
- [4] R. L. Merlino, *Plasma Physics Applied* (Research Signpost, Kerala, India, 2006) p. 73.
- [5] J. Goree, *Plasma Sources Sci. Technol.* **3**, 400, (1994).
- [6] M. S. Barnes, J. H. Keller, J. C. Forster, J. A. O'Neill, and D. K. Coultas, *Phys. Rev. Lett.* **68**, 313 (1992).
- [7] A. Douglass, V. Land, K. Qiao, L. Matthews, and T. Hyde, *Phys. Plasmas* **19**, 013707 (2012).
- [8] V. Land, L. S. Matthews, and T. W. Hyde, *Phys. Rev. E* **81** 056402 (2010).
- [9] A. Douglass, V. Land, L. Matthews, and T. Hyde, *Phys. of Plasmas* **18**, 083706 (2011).
- [10] A. V. Ivlev, M. Kretschmer, M. Zuzic, G. E. Morfill, H. Rothermel, H. M. Thomas, V. E. Fortov, V. I. Molotkov, A. P. Nefedov, A. M. Lipaev, O. F. Petrov, Yu. M. Baturin, A. I. Ivanov, and J. Goree, *Phys. Rev. Lett.* **90**, 5 (2003).
- [11] K. Takahashi, J. Lin, M. Hénault, and L. Boufendi, *IEEE Trans. Plasma Sci.* **46**, 704 (2018).
- [12] A. G. Khrapak, V. I. Molotkov, A. M. Lipaev, D. I. Zhukhovitskii, V. N. Naumkin, V. E. Fortov, O. F. Petrov, H. M. Thomas, S. A. Khrapak, P. Huber, A. Ivlev, and G. Morfill, *Contrib. Plasma Phys.* **56**, 253 (2016).
- [13] M. Hénault, Ph. D. thesis, University of Orleans, Orleans, 2015.
- [14] M. Boudhib, Ph. D. thesis, University of Orleans, Orleans (2017).
- [15] E. O. Johson, and L. Malter, *Phys. Rev.* **80**, 1 (1950).
- [16] D. B. Allan, T. Caswell, N. C. Keim, and C. M. Van der Wel, Zenodo, trackpy: Trackpy v0.4.1 (Version v0.4.1), (2018).
- [17] H. Huang, M. Schwabe, and C. Du, *J. Imaging* **5**, 36, (2019).

- [18] T. Gyergyek, and J. Kovačič, *Phys. Plasmas* **22**, 093511 (2015).
- [19] D. P. Lymberopoulos, and D. J. Economou, *J. Res. Natl. Inst. Stand. Technol.* **100**, 473 (1995).
- [20] J. E. Daugherty, R. K. Porteous, and D. B. Graves, *J. Appl. Phys.* **73**, 1617 (1993).
- [21] D. G. Batryshev, T. S. Ramazanov, M. K. Dosbolayev, and M. T. Gabdulin, *J. Nano-Electron. Phys.* **6**, 3, 03032 (2014).
- [22] P. Chabert and N. Braithwaite, *Physics of Radio-Frequency Plasmas* (Cambridge Univ. Press, Cambridge, 2011).
- [23] T. Panagopoulos, and D. J. Economou, *J. Appl. Phys.* **85**, 7 (1999)
- [24] M. A. Liberman, and A. J. Lichtenberg, *Principles of plasma discharges and materials processing*, (A Wiley-Interscience Publication, New York, 1994).
- [25] A. Bouchoule, *Dusty plasmas Physics, Chemistry and Thechnological Impacts in Plasma Processing*, (Wiley-Interscience Publication, Orléans, 1999).

# Chapter 8

## Perspective

### 8.1 Introduction to LIBS

Laser induced breakdown spectroscopy (LIBS) is a material diagnostic method, it consists of following four parts:

- Ablation of material by laser heating.
- Generation of plasma based on the released material element particles.
- Acquisition of spectrum emitted by generated plasma.
- Analyze of obtained spectrum.

#### 8.1.1 Ablation of material by laser heating

Ablation of material is to release some material molecules or atoms from material surface by laser heating, as the first step of the LIBS. The material surface can be locally heated under the laser light illumination to a very high temperature. When element particles obtain enough energy, they can exit from the material surface. To quantify this effect, a notion of power density is employed (with unite often in  $\text{GW}/\text{cm}^2$ ):

$$I = \frac{E}{\tau A}, \quad (8.1)$$

where  $E$ ,  $\tau$  and  $A$  are energy, duration of laser pulse and surface of illuminated spot by laser, respectively.

When the power density exceeds a threshold, the ablation of material occurs. The threshold depends on both laser and material parameter: wave length of laser light, laser light absorption capacity and thermal diffusion coefficient of the material.[1, 2, 3]

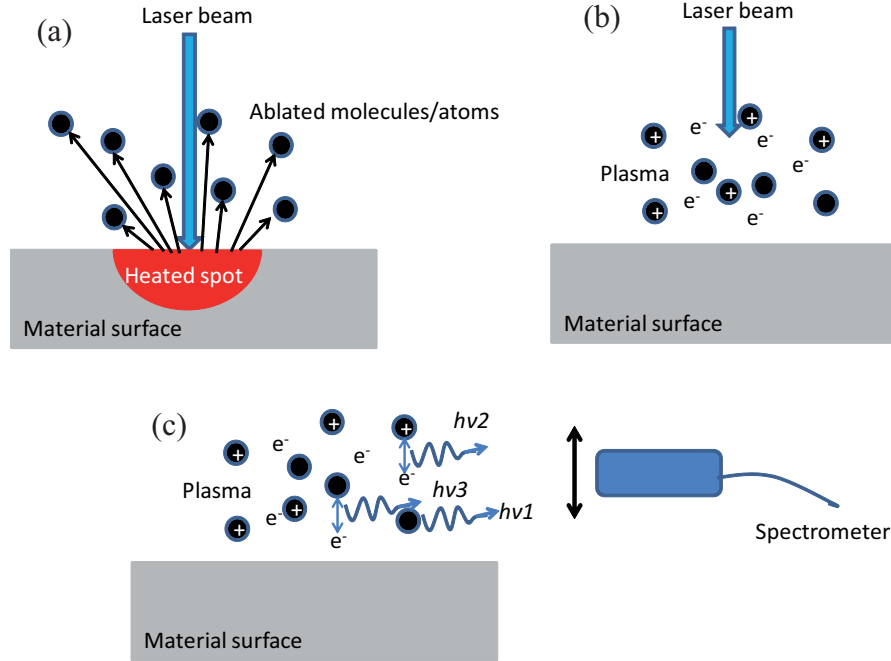


Figure 8.1: .

### 8.1.2 Generation of plasma based on the released material element particles

Plasma can be then generated by interaction between laser light and ablated material element particles. Being heated to very high temperature, the ablated molecules/atoms have high kinetic energy to provoke collision, multi-photonic and thermal ionization. Those ionizations create first free electrons. Once the free electrons are created, they can absorb the photons to obtain enough high energy to enhance the ionization as well as the electron density. This is an inverse Bremsstrahlung absorption. The absorption coefficient is proportional to square of the electron density:

$$\alpha_B \propto [1 - \exp(-\frac{hc}{\lambda k_B T})] \lambda^3 n_e^2, \quad (8.2)$$

where  $h$ ,  $c$ ,  $\lambda$ ,  $T$ ,  $n_e$  are Planck constant, light speed, wave length of laser light, temperature and electron density, respectively.

The increase of electron density enhances the absorption coefficient, and the increase of the absorption coefficient enhances the electron density. Consequently, an avalanche forms, and plasma ignites.[1, 2, 3] The plasma is called Laser Induced Plasma (LIP).

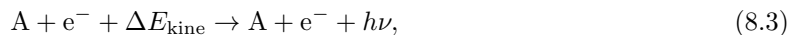
After the generation, the plasma then expands its volume, and is confined by ambient gas. The confinement depends on gas pressure, gas nature and ablated material nature. Some plasma parameters such as plasma volume, plasma density are influenced by the confinement. At higher pressure, plasma is confined in a small volume, plasma density is higher, but plasma has shorter life duration. At lower pressure, plasma is less confined and can expand to bigger volume. In this case, plasma density is lower so do the emission luminosity. For a determinate material and gas nature, there exists an

optimal pressure of ambient gas for maximal emission luminosity. That is measured experimentally and generally in the range of 10 to 100 mbar.[2] The volume of plasma depends on the pressure of ambient gas, and it is about the order of mm at high pressure ( $\sim$  bar), of cm at low pressure ( $<$ mbar).[2]

### 8.1.3 Light emission by LIP

In the generated plasma, light emission comes from 3 main sources: Bremsstrahlung radiation, recombination radiation and spontaneous transition. Bremsstrahlung radiation and recombination radiation contribute continuous spectrum and spontaneous transition contributes discrete lines.[1, 2, 4]

Bremsstrahlung radiation designates the radiation when electron is slowed down by a neutral atom or an ion. The kinetic energy of electron converted to light emission.



where A is a elemental particle, atom or ion.

When an electron and an atom have a recombination collision, an energy conversion occurs from kinetic energy of electron to light emission.



Spontaneous transition of element particles is due to excitation/de-excitation process. The transition from permitted upper energy level to inferior energy level gives discrete spectrum lines and which contains material element information, such as chemical composition, and plasma information, such as electron temperature and electron density.



Immediately after the laser pulse induction, Bremsstrahlung radiation and recombination collision dominate light emission process. It is due to high plasma density and high ionization degree that a reduction of ionization energy occurs. Since only electrons whose energy below the effective ionization energy can exit in the bounds of an element particle, otherwise, electrons having higher energy will be ionized. The reduced ionization energy limits permitted levels, consequently, the excitation and de-excitation of bound electrons between excited levels are strongly limited by small number of accessible levels. In this earlier period, continuum spectrum can cover discrete lines.[4] Over the expansion and relaxation, the Bremsstrahlung radiation and recombination collision reduce and spontaneous transition takes place. In point of view plasma spectrometry, there exists an optimal delay from the laser induction to obtain a maximum ration of discrete line intensity on continuum spectrum intensity depending on material simple, ambient gas nature and pressure.

## 8.2 Experiment

### 8.2.1 Particles

Carbon particles are used as targets. Their size is varied between 0.5 to 1  $\mu\text{m}$ . Carbon particles scatter less light emission, so they are difficult to be seen by visible laser beam.

Table 8.1: Characteristic parameters of Nd:YAG Q-Switch laser.

Nd:YAG Q-Switch laser	
Wavelength	1064 nm
Maximum energy	400 mJ
Average power (Max.)	4 W
Pulse duration	5 ns
Pulse frequency	20 Hz

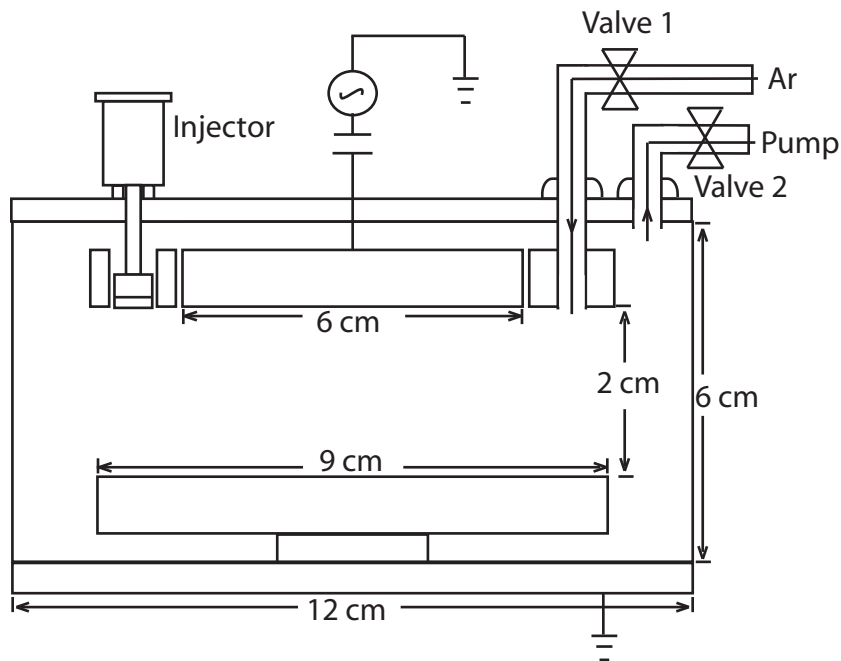


Figure 8.2: Crosse sectional view of the reactor chamber with a dispenser of the dust particles.

### 8.2.2 Laser

Nd:YAG Q-Switch (Quantel, Brillant model) laser was used as induction laser. It can produce a high power pulse of 1064 nm. Characteristic parameters are shown in table 8.1.

There are two modes to trigger laser beam: auto continue mode and manual mode. At auto continue mode, the laser launch pulse with frequency of 20 Hz, but it is not suitable for the analysis of plasma suspending nanoparticle LIBS. A remote controller permits to launch single pulse and permits to reduce laser energy. Since the wavelength 1064 nm is in the range of infrared, a visible flash light is associated to indicate the direction. The laser generator requires an initialization time about 30 minute before the first shoot after started-up.

### 8.2.3 Reactor

A PK-3 modified chamber was used as plasma reactor. (Fig. 8.4) The chamber dimension is length=12 cm, width=12 cm and height=6 cm. It contains two cylindrical capacitive coupled electrodes which are set at the top and bottom side of chamber. The top side electrode is connected to a RF generator via a matching box. The bottom side electrode is contacted with chamber walls and connected to mass. There is a hole in the center of the bottom electrode. The hole is served to create a potential well and trap particles. An entrance and an exit of gas are situated at the edge of the top side wall. The gas entrance is connected to an Ar gas line, and a graduate valve is used to control gas flow. The gas exit is connected to a primary pump with a valve. A baratron gauge is used to monitor gas pressure in the chamber. A particle injector is situated on the top side wall opposite side from the gas entrance and exit. Whole reactor is supported by a platform which can regulate reactor height. The 4 side faces walls are transparent glass.

### 8.2.4 Spectrometer

An Echelle spectrometer is used for the spectroscopic analysis. The spectrometer (Andor technology, model Mechelle 5000) can obtain a specter with a large range, from 200 nm to 1 000 nm. A CCD detector is connected just behind the spectrometer. There are two ways to launch an acquisition: intern trigger and extern trigger. With intern trigger mode, the beginning timing is controlled from computer interface, and with extern trigger, the beginning timing is synchronized to an input pulse signal.

There are three modes of acquisitions:

- Real time acquisition.
- Single acquisition.
- Accumulation acquisition.

With real time acquisition mode, the spectrometer redoes automatically a new acquisition immediately after the previous one being done. This mode is used for the monitoring of light emission. With Single acquisition mode, the spectrometer dose only one acquisition at a desired timing. This mode allows analyze the spectrum of specified timing. With accumulation acquisition mode, the spectrometer launches specified number of acquisition and superposes them to one spectrum. This mode allows increasing signal count number and neutralizing noise. It requires a good repeatability for each acquisition.

There three parameters to regulate for acquisitions

- Gain: Multiply factor. Range 0~255. It multiplies all signals as well as noise.
- Delay: Delay between trigger signal and acquisition timing. It has a time unity.
- TTL : Acquisition duration. CCD detector integrates intensity during this period. It has a time unity.

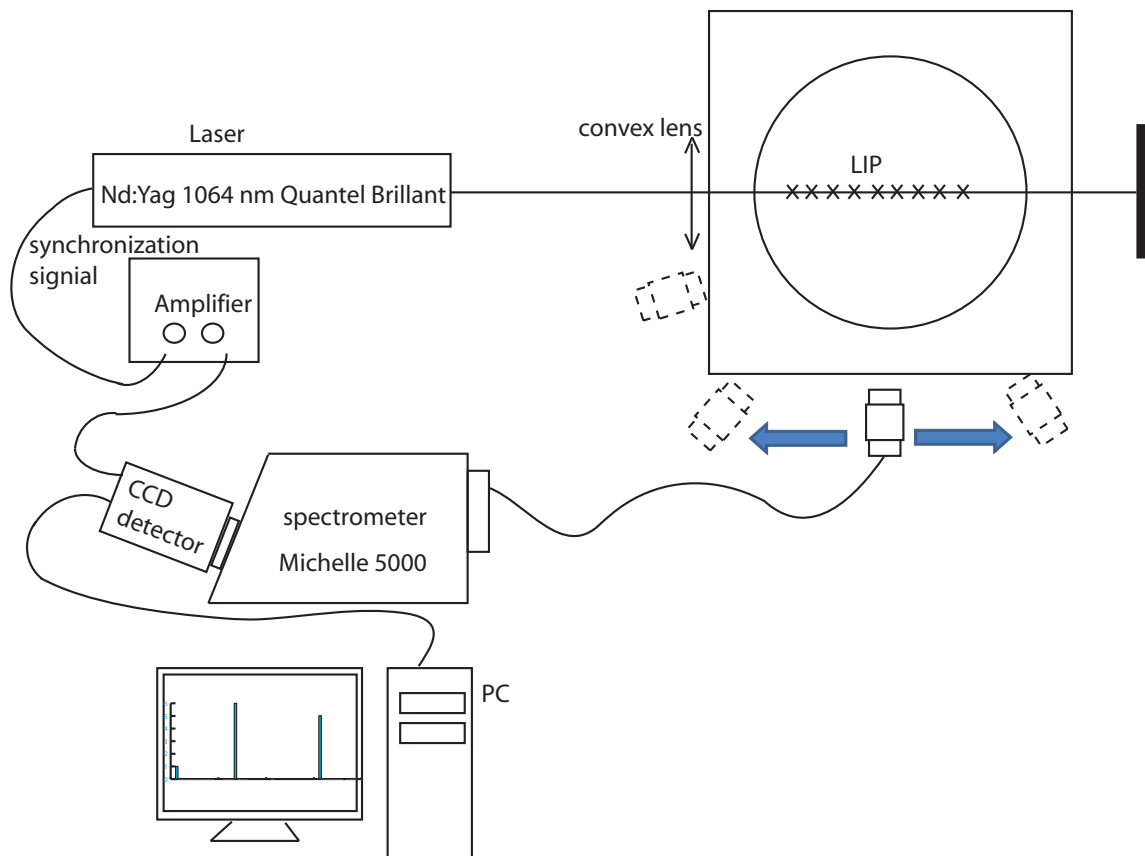


Figure 8.3: Top view of the schematic of the experiment setup.

### 8.2.5 Schematic

Nd:YAG laser is positioned in front of plasma reactor. A convergence lens is set between the laser and plasma reactor. Focal distance of the convergence lens is 7 cm. In order to set the focal point to the center of reactor and to avoid the converged laser pulse damage the glass wall, the convergence lens is very close to the glass wall. The Laser is connected with the spectrometer via a signal amplifier. For each laser pulse, a synchronization signal is sent from the laser to spectrometer. Light emission is collected by spectrometer via a light fiber with a collection convergence lens. The light fiber can be positioned around the reactor.

## 8.3 Result

We injected the carbon particles into the reactor chamber then triggered the laser. The gas pressure, RF power and gas flow were regulated in order to better confine the particles. Since the small carbon particles are hardly to be seen by visible laser light, the transport behaviours of dust particles discussed in previous chapters should be taken into account to control their levitating positions.

Figure 8.5 shows the first LIP observed. The blue light indicated is the LIP of the carbon particles.

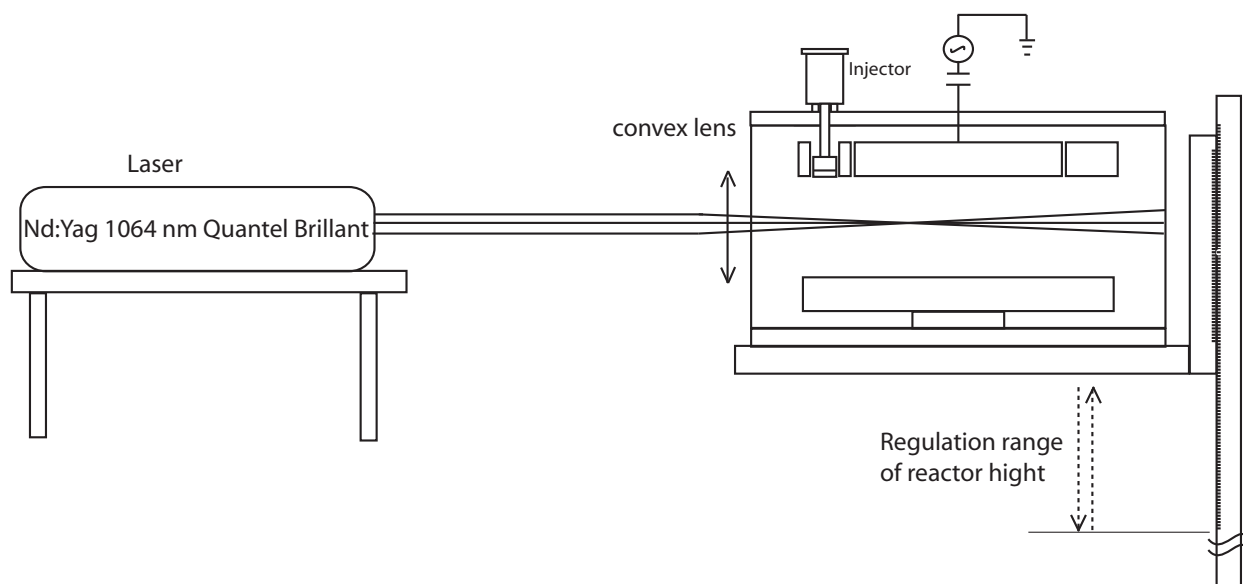


Figure 8.4: Sid view of the schematic of the experiment setup. The height position of the reactor can be regulated.

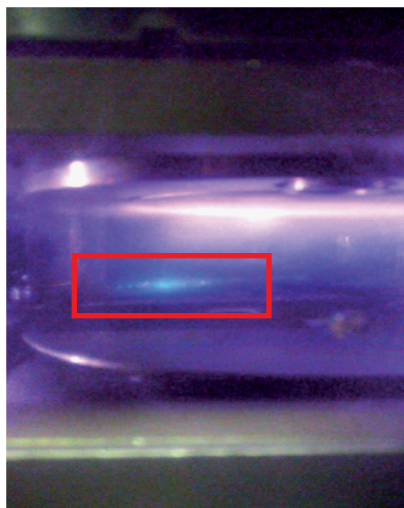


Figure 8.5: The LIP obtained immediately after the injection of the carbon particles.

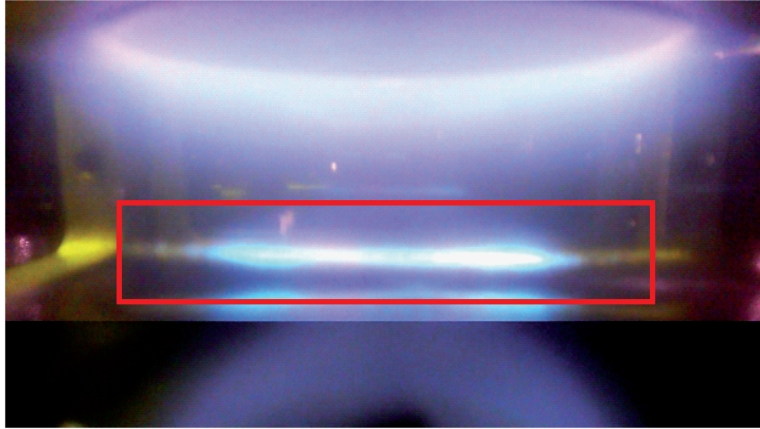


Figure 8.6: The improved LIP. Particles remain stable in the bottom side of reactor chamber, and the LIP can be obtained constantly.

RF power at 6 W, and gas pressure at 1 mbar (100 Pa). In this case, the LIP can only be observed immediately after the injection of the particles. It means that the particles are not stable in the plasma. The situation is improved by increasing the RF power and reducing the gas flow. To increase the RF power to 8 W can enhance the electric field of the sheath to confine the carbon particles, but when the RF power is too high as 10 W, the carbon particles are repelled and dispersed. This reactor chamber has both the entry and exit of gas, and that creates a gas flow in it. The gas flow perturbs the carbon particles and causes the instability. Figure 8.6 shows the improved LIP of carbon particles. In the improved case, the carbon particles can remain stable in the plasmas and the LIP is obtained constantly.

## 8.4 Conclusion

The LIP, which is the first step of the LIBS, of the carbon particles is obtained and improved in the plasmas. That is an application of the studies of the transport behaviours of the dust particle in dusty plasmas. The confinement and transport control of dust particles in plasmas give the possibility to perform the LIBS to the small sized aerosol materials by using dusty plasmas. That has many advantages to perform the LIBS in dusty plasmas than in air, as like the stability of the levitating positions of the dust particles, which are the target materials, and the confinement by the plasmas results in a dense LIP. Due to some technical problems of the experimental setup, and the project period insists that the detection and the analysis of the spectrum of the LIP should be the perspective of the future works.

## 8.5 French summary

Dans ce chapitre, la perspective d'appliquer les résultats de l'étude des comportements et de transport des particules dans le plasma à leur caractérisation par la méthode de LIBS (Laser Induced Breakdown

Spectroscopy ) est décrite. La LIBS est une méthode d'analyse, par spectroscopie d'émission, de la composition chimique des matériaux. Le laser évapore la surface de celui-ci et en génère un plasma appelé LIP (Laser Induced Plasma). L'émission du LIP, contenant les informations sur le matériel, est ensuite détectée et analysée par le spectromètre. L'application de la LIBS sur les petites particules, comme les aérosol, cependant, peut rencontrer des difficultés par sa dimension toute petite et son expansion en l'air. L'avantage de l'appliquer dans le plasma poudreux est de pouvoir confiner et contrôler les petites particules pour qu'elles restent stables et en nuage dense. Les dispositifs mis en œuvre et la méthode sont présentés. Le LIP est obtenu et amélioré dans l'expérience en contrôlant le transport des particules dans le plasma.



# Bibliography

- [1] M. Boudhib, Ph. D. thesis, University of Orleans, Orleans (2017).
- [2] D. L'hermite, J.-B. Sirven-LIBS: spectrometrie d'émission optique de plasma induit par laser, Techniques de l'ingénieur (2017).
- [3] B. Sallé, Ph. D. thesis, University of Orleans, Orleans (1998).
- [4] A. De Giacomo, R. Gaudiuso, M. Dell'Aglio, A. Santagata, spectrochimica acta part B, **65**, 385,(2010)
- [5] D. W. Hahn and N. Omenetto, Appl. Spectrosc. **64**, 335 (2010).
- [6] D. W. Hahn and N. Omenetto, Appl. Spectrosc. **66**, 347 (2012).



## Chapter 9

# Conclusion

Two parts of the studies of the dusty plasmas were performed in this thesis. The formation of dust particles and the transport behaviour of dust particles.

In the part of the formation of dust particles, A mixture gas of  $C_2H_2/Ar$  was used to ignite the plasmas, and carbon dust particles were generated in the plasmas. It is known that the formation process of dust particles in plasmas can be determined by 3 steps: nucleation, agglomeration and surface grow. This part of thesis focused on the nucleation step. A method of determination of the nucleation process by monitoring the self-bias voltage was described. In the experiments, the nucleation time in function of RF power of plasmas, gas pressure and gas temperature was investigated. The results showed that the nucleation process occurs faster in higher power, higher pressure and lower temperature. The dependency of the nucleation time on the temperature was explained by the vibration-transition energy relaxation mechanism, and that on the RF power and pressure was explained by the ratio of the charge and diffusion time of the small dust particles.

In the part of the transport behaviours of dust particles, industrially fabricated particles with determined size were used. The particles were injected into Ar plasmas, and were observed by laser scattering with a CCD camera. Characterisations of Ar plasmas for the specific experiment setup were performed firstly in order to be able to discuss the interaction of plasmas to the dust particles. The diagnostics of plasma were performed by a double langmuir probe. Pulse-time modulation to the Ar RF plasmas was studied to be a factor to influence and to control the transport of dust particles. Particles of mono-dispersed size were firstly studied in the plasmas. The levitating positions and falling down processes were studied in function of the RF power and pulse-time modulation. Secondly, two sizes particles were injected into the plasma at same time. The different transport behaviours, as like the segmentation of levitation and different timing of falling down basis on their size, were observed. Particles of mixture sizes were successfully separated one size particles from other sizes. The mechanisms of transport behaviours of the dust particles were investigated by the combination of the diagnostic of plasma parameters (electron temperature and ion density in principle) by the double langmuir probe and calculation of the forces acting on the dust particles. Calculation methods adjusted to the specific experiment setup were established. The calculation results fitted to that of the experiments. That means the mechanisms were correctly explained and the calculation methods

could be used to find discharge conditions for the control of the transport of the dust particles in the plasmas.

In total, the behaviours and control methods of dust particles in the plasmas, including that of the generation by the reactive gases, transport in the bulk of plasma, and falling down from the plasmas, were studied. It gives the perspectives to manipulate small sized aerosol material as dust particle in the plasmas. Dusty plasma could be used for the fabrication of small particles, work as a sieve to classify dust particles by their sizes, or be used to confine aerosol materials as dust particle.